Modeling and Simulation
of Thermo-Electrochemistry of Thermal Runaway
in Lithium-Ion Batteries

Von der Fakultät Energie-, Verfahrens- und Biotechnik der Universität Stuttgart zur Erlangung der Würde eines Doktor-Ingenieurs (Dr.-Ing.) genehmigte Abhandlung

Vorgelegt von

Nanako Tanaka
aus Fukuoka, Japan

Hauptberichter:	Prof. Dr. Wolfgang G. Bessler
Mitberichter:	Prof. Dr. K. Andreas Friedrich
Mitberichter:	Prof. Dr. Jürgen Garche

Tag der mündlichen Prüfung: 05.05.2015

Institut für Thermodynamik und Wärmetechnik
der Universität Stuttgart

2014

Abstract

With the rapid development of high-power lithium-ion batteries, there are growing demands for improving the safety of lithium-ion cells. Exothermic electrochemical reactions in the cells are responsible for thermal risks. The goal of this thesis is to provide a detailed analysis of exothermic degradation mechanisms (i.e., runaway chemistries) inside of a lithium-ion cell through the development of runaway chemistry numerical models coupled with an electrochemical battery model. These models are based on a thermo-electrochemical multi-scale approach and were implemented in an in-house simulation environment. In this work, degradation mechanisms for both the anode and the cathode were developed. Moreover, lithium-ion batteries with two types of cathodes (lithium iron phosphate and a blend of lithium nickel cobalt aluminum oxide and lithium manganese oxide) were also investigated. The runaway chemistry models established in this work include solid elecrolyte interface (SEI) formation and decomposition, oxygen evolution from cathode and solvent oxidation, and lithium hydration associated with reactions between gaseous products of SEI decomposition. These chemistries were modeled as global reactions with an Arrhenius-type temperature dependence. In order to validate and obtain the kinetic parameters of these global reactions, simulations of differential scanning calorimetry were conducted for each electrode. The thermal calculation framework also allows further establishment of sub-reactions in a cell. Furthermore, simulations of an entire cell were conducted utilizing the established runaway chemistries of the electrodes. We also investigated how degradation processes influence cell conditions under thermal and electrical abuse. The analysis of these abuse simulations enables to predict possible triggers of thermal runaway, in addition to providing model validity under abuse conditions.

Zusammenfassung

Aufgrund der rasant steigenden Energie- und Leistungsdichte moderner Lithium-Ionen-Batterien wächst auch der Anspruch an die Sicherheit der Zellen. Dabei stellen exotherme elektrochemische Reaktionen das größte Risiko für die Zellen dar, da sie ein sogenanntes thermisches Durchgehen oder „thermal runaway"auslösen können. Das Ziel dieser Arbeit ist es, durch die Entwicklung numerischer Modelle exothermer Degradationsmechanismen und deren Kopplung an ein elektrochemisches Batteriemodell eine detaillierte Untersuchung des thermischen Durchgehens von Li-Ionen-Batterien durchzuführen. Die Modelle basieren auf einem thermo-elektrochemischen Multiskalenmodell und wurden als Erweiterung einer bestehenden Simulationsumgebung implementiert. Degradationsmechanismen wurden dazu sowohl an der Graphit-Anode als auch an zwei verschiedenen Kathoden untersucht, nämlich Lithium-Eisenphosphat sowie einer Mischung aus Lithium-Nickel-Kobalt-Aluminiumoxid und Lithium-Mangandioxid. Die Modelle der chemischen Reaktionen, die zu einem thermischen Durchgehen führen, berücksichtigen die Bildung bzw. Auflösung einer SEI (solid electrolyte interface) und die Sauerstoffentwicklung durch Oxidation der Kathode bzw. des Elektrolyten ebenso wie Reaktionen zwischen gasförmigen Produkten der SEI-Zersetzung. Die chemischen Mechanismen wurden dazu als globale Reaktionen implementiert und sie werden jeweils durch einen Arrhenius-Ansatz beschrieben. Um die kinetischen Parameter zu bestimmen und zu validieren, wurden für jede Elektrode dynamische Differenzkalorimetrieverläufe simuliert. Die globalen Reaktionsmechanismen können durch Hinzufügen von Nebenreaktionen oder durch eine detailliertere Beschreibung der Teilreaktion ergänzt bzw. verfeinert werden. Anschließend wurden unter Verwendung der entwickelten „thermal runaway"-Mechanismen Simulationen der gesamten Batterie durchgeführt. Dadurch konnte der Effekt der Degradationsprozesse auf das Verhalten der Zelle bei thermischer oder elektrischer Überlastung untersucht werden. Zunächst wurde dazu die Gültigkeit des Modells für diese Betriebsbedingungen belegt. Durch die weitere Analyse dieser Simulationen können schließlich kritische Betriebsbedingungen vorhergesagt werden, bei denen ein erhöhtes Risiko des thermischen Durchgehens besteht.

Contents

Acronyms

Term	Description
1D	One-Dimensional
ASCII	American Standard Code for Information Interchange
C-rate	Normalized battery current
CID	Current Interupt Device
DAE	Differential-Algebraic Equations
DEC	Diethyl Carbonate
DENIS	Detailed Electrochemistry and Numerical Impedance Simulation
DFT	Density Functional Theory
DLR	Deutsches Zentrum für Luft- und Rahmfahrt, German Aerospace Center
DMC	Dimethyl Carbonate
DSC	Differential Scanning Calorimetry
EC	Ethylene Carbonate, $C_3H_4O_3$
EMC	Ethyl Methyl Carbonate
FTA	Fault Tree Analysis
LCO	Lithium Cobalt Oxide, $LiCoO_2$
LFP	Lithium Iron Phosphate, $LiFePO_4$
LIB	Lithium-ion Battery
LIMEX	Extrapolation integrator for Linearly IMplicit ODEs
LMO	Lithium Manganese Oxide, $LiMn_2O_4$
MCMB	MesoCarbon MicroBead
NASA	National Aeronautics and Space Administration
NCA	Lithium Nickel Cobalt Aluminum Oxide, $LiNi_{0.8}Co_{0.15}Al_{0.05}O_2$
NIST	National Institute of Standards and Technology
NMC	Nickel Manganese Cobalt Oxide
OCV	Open-Circuit Voltage
ODE	Ordinary Differential Equations
P2D	Pseudo-two-Dimensional
PC	Propylene Carbonate, $C_4H_6O_3$
PE	Polyethylene

Term	Description
PEMFC	Polymer Electrolyte Membrane Fuel Cell
PPE	Polypropylene
PTC	Positive Temperature Coefficient
SEI	Solid Electrolyte Interface
SEM	Scanning Electron Microscopy
SOC	State of Charge
SOFC	Solid Oxide Fuel Cell
SPM	Single-Particle Model
TEM	Transmission Electron Microscopy
ZSW	Center for Solar Energy and Hydrogen Research Baden-Württemberg

List of Symbols

Term	Unit	Description
A	m^2	Specific area
a_{decomp}	$-$	Constant in active surface model of SEI decomposition
$A_{\mathrm{dl}}^{\mathrm{V}}$	m^2/m^3	Electric capacity area per volume due to double-layer
a_{growth}	$-$	Film growth rate constant
A_{surf}	m^2/m^3	Volumetric active surface area
$A_{\mathrm{surf,init}}$	m^2/m^3	Initial volumetric active surface area
$A_{\mathrm{surf,SEIdecomp}}$	m^2/m^3	Volumetric active surface area of SEI decomposition
$A_{\mathrm{surf,SEIform}}$	m^2/m^3	Volumetric active surface area of SEI formation
c^*	kg/m^3	Concentration of bulk
$c_i^{a_i}$	kg/m^3	Concentration species i with reaction order a
c_{Li}	kg/m^3	Concentration of lithium ions
$c_{\mathrm{Li,el}}^a$	kg/m^3	Concentration of lithium in electrolyte with reaction order of a
c_{LMO}	kg/m^3	Concentration of lithium ions in LMO
c_{NCA}	kg/m^3	Concentration of lithium ions in NCA
C_p	J/K	Heat capacity at constant pressure
$c_{\mathrm{p}}^{\mathrm{eff}}$	J/kg/K	Effective heat capacity
D_i	m/s^2	Diffusion coefficient of species i
D_i^{migr}	m/s^2	Diffusion coefficient of species i due to migration
E	V	Cell potential
ΔE	V	Potential change
e	$-$	Anode/Cathode
E'	V	Formal potential of an electrode versus reference
E''	V	Potential of an electrode versus reference
E_{act}	J/mol	Activation energy
$\Delta E^{\ddagger}$	J/mol	Standard internal energy of activation
E_{eq}	V	Cell potential at equilibrium
F	C/mol	Faraday constant, 9.64863×10^4 C/mol
f	$-$	Frequency factor, unit depends on order
f_{d}	1/s	Rate constant of SEI decomposition

Term	Unit	Description
ΔG	J/mol	Gibbs free energy
$\Delta G^{\ddagger}$	J/mol	Standard free energy of activation
$\Delta G_{\mathrm{a}}^{\ddagger}$	J/mol	Anodic free energy of activation
$\Delta G_{\mathrm{c}}^{\ddagger}$	J/mol	Cathodic free energy of activation
ΔH	J/mol	Enthalpy of reaction
$\Delta H^{\ddagger}$	J/mol	Standard enthalpy of activation
$\Delta H_{\mathrm{in/ex}}$	J/mol	Reaction enthalpy of intercalation/extraction processes
ΔH_n	J/mol	Reaction enthalpy of runaway reaction n
i_0	A/m^3	Exchange current density
$i_{\mathrm{dl}}^{\mathrm{V}}$	A/m^3	Volumetric current density due to double-layer
$i_{\mathrm{F}}^{\mathrm{V}}$	A/m^3	Volumetric faradaic current density
i_{a}	A	Anodic current
i_{c}	A	Cathodic current
k'	1/s	Standard rate constant
$k_{n,\mathrm{char}}$	1/s	Rate constant for charge-transfer runaway reaction n
$k_{n,\mathrm{non\text{-}char}}$	1/s	Rate constant for non-charge-transfer runaway reaction n
k_{b}	1/s	Rate constants of backward process
k_{decomp}	1/s	Rate constant of SEI decomposition
k_{f}	1/s	Rate constants of forward process
k_{form}	1/s	Rate constant of SEI formation reaction
L_{elde}	m	Length of electrode
M_i	g/mol	Molar mass of species i
O	–	Oxidized form of the standard system, O $+ ze \leftrightarrow$ R
P	Pa	Pressure
P_{ex}	J/s	Additional power required in DSC
$\dot{q}_{\mathrm{chem}}^{\mathrm{V}}$	W/m^3	Electrochemical heat source
$\dot{q}_{j}^{\mathrm{V}}$	W/m^3	Heat source per volume by j
$\dot{q}_{\mathrm{pol}}^{\mathrm{V}}$	W/m^3	Polarization heat source
$\dot{q}_{\mathrm{rev}}^{\mathrm{V}}$	W/m^3	Reversible heat source
$\dot{q}_{\mathrm{run,char}}^{\mathrm{V}}$	W/m^3	Runaway chemistry heat source for charge transfer reaction
$\dot{q}_{\mathrm{run,non\text{-}char}}^{\mathrm{V}}$	W/m^3	Runaway chemistry heat source for non-charge transfer reaction
$\dot{q}$	W/m^2	Heat flux
q_{ex}	J	Additional energy required in DSC
q_p	J	Heat transferred at constant pressure
R	J/mol/K	Gas constant, 8.3144621 J/mol/K
r_n	mol/s/m^3	Reaction rate of runaway reaction n
R	–	Reduced form of the standard system, O $+ ze \leftrightarrow$ R

Term	Unit	Description
r_v	m^2/m^3/s	Volumetric rate constant
ΔS	J/mol/K	Entropy of reaction
ΔS_blend	J/mol/K	Entropy of lithium intercalation for blend material
$\Delta S^\ddagger$	J/mol/K	Standard entropy of activation
$\dot{s}_i^V$	mol/m^3/s	Volumetric source term of species i
ΔS_LMO	J/mol/K	Entropy of lithium intercalation for LMO material
ΔS_NCA	J/mol/K	Entropy of lithium intercalation for NCA material
T	K	Temperature
t	s	Time
T_amb	K	Ambient temperature
T_surf	K	Cell surface temperature
V	m^3	Volume
v_b	kg/m^3/s	Rate of backward process
v_f	kg/m^3/s	Rate of forward process
v_net	kg/m^3/s	Rate of net process
W	J/m^3	Work
w_LMO	−	Weight ratio of LMO to total mass of blend
w_NCA	−	Weight ratio of NCA to total mass of blend
x'_m	−	Grid number m in reduced coordinate, x'
$X_\mathrm{Li,bulk}^b$	kg/m^3	Concentration of lithium in bulk with reaction order of b
X_LMO	−	Mole fraction of lithium ions of LMO
X_NCA	−	Mole fraction of lithium ions of NCA
x_n	−	Grid number n in original coordinate, x
z	−	Number of transferred charges
α_a	−	Anodic symmetry factor
α_c	−	Cathodic symmetry factor
α_conv	W/m^2/K	Convective heat transfer coefficient
β	K	Linear coefficient
$\Delta\phi_\mathrm{eq}$	V	Equilibrium potential difference
ϵ	−	Porosity
ϵ_surf	−	Emissivity
ϵ_SEI	−	Volume fraction of SEI
η_act	V	Activation overpotential
η_conc	V	Concentration overpotential
λ^eff	W/m/K	Effective heat conductivity
ϕ_an	V	Potential of anode
ϕ_ca	V	Potential of cathode

Term	Unit	Description
ϕ_{elde}	V	Potential of electrode
ϕ_{elyt}	V	Potential of electrolyte
ρ_{eff}	kg/m^3	Effective density
ρ_i	kg/m^3	Density of species i
σ	S/m^2	Conductivity
σ_i	S/m^2	Conductivity of species i
σ_{s}	W/m^2/K^4	Stefan-Boltzmann constant, 5.670373×10^{-8} W/m^2/K^4

1 Introduction

The science, research, and technology of energy transition and energy storage devices has become imperative. Global warming caused by greenhouse gases poses a risk of dramatic climate change including more frequent occurrences of extreme weather events such as heat waves, droughts and heavy rain falls, ocean acidification, and species extinctions due to shifting temperature regimes [1]. One international initiative against global warming is the United Nations Framework Convention on Climate Change (UNFCCC) [2]. The UNFCCC was initiated on 21 March 1994 with 154 nations to aim for the "stabilization of greenhouse gas concentrations in the atmosphere at a level that would prevent dangerous anthropogenic interference with the climate system". On 11 December 1997, the UNFCCC achieved a milestone, the adoption of Kyoto protocol [3]. The Kyoto Protocol sets binding obligations on industrialized nations to reduce emissions of six main greenhouse gases: carbon dioxide (CO_2), methane (CH_4), nitrous oxide (N_2O), hydrofluorocarbons (HFCs), perfluorocarbons (PFCs), and sulfur hexafluoride (SF_6). Similar concepts have also been widely accepted by most developed countries that have not ratified the Kyoto protocol. Moving towards their own goal, each country announces its key policy against greenhouse gases.

In order to reduce greenhouse gas emissions, many countries have begun to pursue alternatives to fossil fuels, i.e., renewable energy. One of the most ambitious and successful examples of such efforts can be seen in the renewable energy sector in Germany [4]. The share of electricity produced by renewable energy in Germany was more than 20% of its total energy consumption in the first half of 2012. In addition to this achievement, the Germany policy, Energiewende (an energy revolution), currently aims to cut greenhouse gas emissions by 40% from 1990 levels by 2020. To achieve this goal, Germany engages in wind energy, biomass, photovoltaics, hydropower, and solar thermal energy initiatives simultaneously [5].

In addition to seeking renewable energies, smart grids can be used to optimize electricity infrastructure and reduce greenhouse gas emissions [6]. A smart grid computerizes the electric utility grid by integrating information technology and electricity infrastructure. This enhanced grid actively senses and responds to changes in power demand and supply

and as a result, reduces the amount of electricity consumed [7]. Smart grids also effectively deal with natural energy resources which are variable by nature and add complexity to normal grid operation. New smart grid features include the ability for grid operators to quickly reduce power demand when renewable energy sources such as wind or solar power decrease, and allow additional energy storage capabilities to absorb excess power when it is not needed. Energy storage will help to smooth out variability in natural resources and make them easier to use [8].

Moreover, greenhouse gas reduction also influences automobile industries. Electric vehicles are considered to be part of the smart grid and part of future electric infrastructure. The development of cars with electric motors combined with, or in place of conventional combustion engines has accelerated since the 1990s. Although the mass production of electric vehicles has been rising only recently, the first attempt dates back to the beginning of the 20th century. The first concept of an electric vehicle was presented by Austrian-German engineer Dr. Ferdinand Porsche in 1900 [9]. Dr. Porsche's hybrid vehicle, named the Lohner-Porsche Mixte Hybrid, was powered by batteries and a gasoline-engine generator [10]. At that time, hybrid vehicles were pursued because the performance of the combustion engine was not sufficient. As gasoline engine technology achieved a remarkable breakthrough, interest in the hybrid vehicle faded away. However, with recent concern over worldwide environmental issue, the hybrid vehicle has been brought back into the spotlight. The first hybrid electric vehicles to gain popularity in the US, UK and Japan was the Toyota Prius. Toyota motors has achieved more than 3 million sales of the Prius in past 16 years since its first release in 1997 [11]. The key behind Prius' success was its efficient nickel-metal hydride (Ni-MH) battery and Miller cycle gasoline engine. The Ni-MH battery was chosen due to its safety and long lasting lifespan. The present model, Prius T3, achieves a fuel efficiency of 3.9 l/100 km [12].

Recent automobile batteries have been gradually replaced with lithium-ion batteries because of their high energy density. The Nissan Leaf is one of the more widely known commercialized electric vehicles (EV) that contain lithium-ion batteries. The 2013 model has a range of 200 km. 192 laminate type lithium-ion batteries are connected in series and parallel to deliver more than 90 kW of power. The latest European and Japanese version of the Toyota Prius uses a space-saving lithium-ion battery that enables three rows of seats and can accommodate seven passengers [12]. Another widely known electric vehicle is Tesla Motors's fully electric sports car. Tesla's first production, the Tesla Roadster, was the first commercial automobile with lithium-ion batteries when it was released in 2008. The Roadster battery pack is made up of 6831 "18650 form-factor" cells and achieved 0 - 60 miles/h acceleration in 3.7 seconds.

However, as more energy is stored, more concerns about safety arise. The lithium-ion

battery made long range driving possible, but at the same time, the risk of thermal runaway became higher. Safety is also a concern outside of the automobile industry, as lithium ion cells are used in various portable devices such as cell phones and laptops. One of the most dangerous and extreme issues with this type of battery is the possibility of thermal runaway [13]. Multiple research experiments have been conducted to tackle the problem of the thermal runaway. Such studies can generally be divided into two groups; the observation of full cells and the observation of individual components. Researchers have investigated individual phenomena on each component at elevated temperatures which are assumed to induce the runaway of a full cell. However, a comprehensive system which can predict and mitigate thermal runaway of lithium-ion cell has not been invented yet.

Therefore, our project, "Thermal runaway of lithium batteries", was initiated to develop a combined methodology of multi-scale deterministic simulation, stochastic simulation, and experimental analyses to understand, predict and control thermal runaway in lithium batteries. Project partners include University of Stuttgart, Center for Solar Energy and Hydrogen Research Baden-Württemberg (ZSW), Offenburg University of Applied Sciences and Deutsches Zentrum für Luft- und Rahmfahrt, German Aerospace Center (DLR). Part of this project aims to bridge the connection between full cell observation and the studies of individual phenomena to give a more rigorous connection and clear insight between utilizing a multi-scale deterministic model. Numerical simulation is available tool to contribute to further understanding this complex event. Detailed chain reaction model enables researchers to identify the cause of severe events. Furthermore, this model can be a part of a mitigation system of battery runaway which can predict an extreme event in advance using the current conditions.

In this thesis, the general concepts of lithium-ion battery components and battery runaway are discussed first, and simulation methodology and results are covered in the subsequent chapters.

Chapter 2 provides a general background of rechargeable lithium-ion batteries and an overview of battery components, battery numerical simulation, and studies of battery thermal runaway. The battery components overview includes general explanations about anode materials, cathode materials, electrolyte, solid electrolyte interface (SEI), separator, and current collectors. The numerical simulation overview shows common methods of current battery simulation including thermal simulation. These contents mainly focus on materials and methods related to this work.

Chapter 3 reviews fundamental methodology of modeling and simulations utilized in this work, including electrochemical kinetic theory, transport theory, parametrization ap-

proaches, simulation software information, and simulation methods for Differential Scanning Calorimetry (DSC). The section on electrochemistry provides theory behind electrode reactions, as well as thermodynamic properties of anodes and cathodes utilized in simulations. The transport theory section consists of topics related to mass and charge transport for electrolyte, and information about heat transport through a cell in a radial direction from the cell center to its surface. Parametrization of the battery model is one of the more challenging topics in numerical simulations of a cell. The parameters used in this work are summarized in Section 3.5. Simulation software and simulation methods used to reproduce the DSC experiment are explained subsequently.

Simulation models and results are shown in Chapter 4 and Chapter 5. In Chapter 4, simulations for individual battery runaway chemistries are discussed. The battery chemistry includes SEI decomposition, SEI formation, oxygen release from cathode active material, solvent oxidation, ethylene oxidation, and lithium hydration. Chapter 5 shows simulations of the entire cell model that consists of both the runaway chemistries shown in Chapter 4 and electrochemistry of battery operation explained in Chapter 3. Battery simulations under nominal operating conditions and abuse conditions are also discussed.

Finally, in Chapter 6, this study is summarized and a future outlook is provided.

2 Background: Lithium-ion batteries

2.1 Overview of rechargeable lithium-ion batteries

Lithium-ion batteries are one of the most popular batteries in today's market. The global lithium-ion market is expected to grow to $33.11 billion in 2019 [14]. This technology has rapidly become a standard power source in a broad range of markets such as cell phones, laptop computers, military electronics, aircraft, and electric or hybrid electric vehicles. To meet market demands, several designs have been developed, including spiral wound cylindrical, wound prismatic, and flat plate prismatic cells in small (0.1 Ah) to large (160 Ah) sizes [15].

Major advantages of lithium-ion batteries relative to other types of batteries include [15]:

- High-rate and high-power discharge capability

- High specific energy, specific power and energy density

- Wide temperature range of stable operation

- Small capacity retention

- Long cycle life

- No memory effect

On the other hand, the major disadvantages are [15]:

- Degradation at high temperature

- Venting (gas release) and possible thermal runaway (Section 2.2)

- Need for protective circuitry

Although it is proven that lithium-ion batteries are safe enough to be commercialized, the disadvantages show that lithium-ion batteries still have safety issues. In fact, accidents due to battery malfunctions have been reported and improvement is inevitable [16]. This work focuses on one of the disadvantages, thermal runaway, which can cause hazardous damage to a cell as well as its environment.

Table 2.1: General characteristics of lithium-ion cells. Based on ref. [15]

Characteristic	Performance range
Operational cell voltage	2.5 to 4.2 V
Specific capacity	100 to 250 Wh/kg
Energy density	245 to 430 Wh/l
Power density	2000 to 3000 W/l
Specific power	700 to 1300 W/kg
Continuous rate capability	Typical:1C, High rate:5C
Operable temperature range	-40°C to 65°C

Table 2.1 shows the general performance characteristics of lithium-ion batteries. One outstanding characteristic of lithium-ion batteries is their high energy density, which is approximately three times higher than that of NiCd or NiMH batteries.

The target cell of this work is a 26650 type wound cylindrical cell (diameter: 26 mm, height: 65 mm). The structure of this cylindrical cell is shown in Figure 2.1. This figure illustrates a wound sheet of anode and cathode combined with current collectors and placed in a cylindrical steel can. The steel can also play the role of a negative terminal being connected with a negative current collector. On the otherhand, the top cap of the cell acts as a positive terminal. The cell top is sealed with a gasket to prevent gas or electrolyte from leaking out. To effectively control overcurrent hazards, several types of cylindrical lithium-ion cells include safety features such as a vent or a Positive Temperature Coefficient (PTC) device.

Lithium-ion batteries are comprised of cells which have lithium intercalation compounds as positive and negative materials (Figure 2.2). The typical active materials of a negative electrode (anode) are natural graphite or hard carbons. The typical active materials of a positive electrode (cathode) are metal oxides with: (1) a layered structure (e.g., Lithium Cobalt Oxide, $LiCoO_2$ (LCO)), (2) a spinel structure (e.g., Lithium Manganese Oxide, $LiMn_2O_4$ (LMO)) and (3) an olivine structure (e.g., Lithium Iron Phosphate, $LiFePO_4$ (LFP)). Blended cathode materials are also widely commercialized. The blend is a mix of several metal oxides and it can compensate for the disadvantages of individual materials. The target cells in this work have cathode materials of LFP and a blend of LMO and Lithium Nickel Cobalt Aluminum Oxide, $LiNi_{0.8}Co_{0.15}Al_{0.05}O_2$ (NCA). On the anode side, MesoCarbon MicroBead (MCMB) is assumed for the target cell. Details about anode and cathode materials will be discussed in Section 2.3 and 2.4, respectively.

When a battery is charged, the positive electrode is oxidized and the negative electrode is reduced and vice versa for discharge (Equation 2.1). During the charge/discharge process, lithium ions are intercalated/extracted from interstitial space between atomic
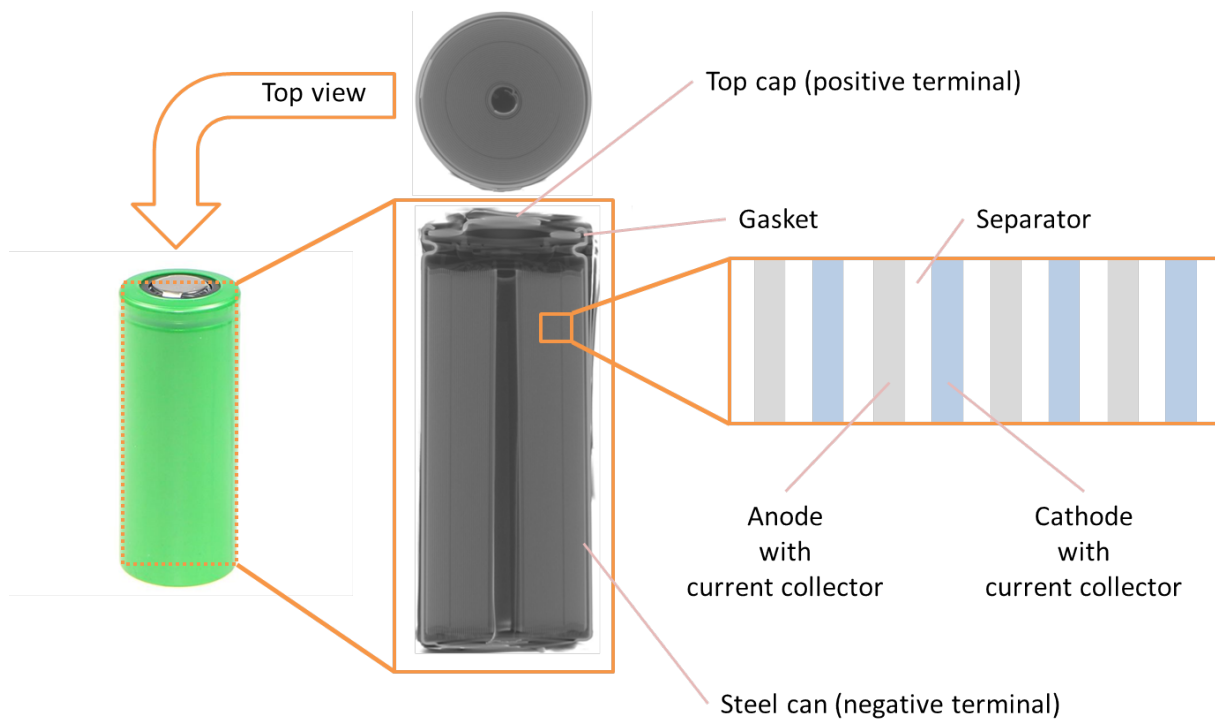
Figure 2.1: Structure of the lithium-ion cell used in this work. CT image: courtesy of Offenburg University of Applied Sciences.
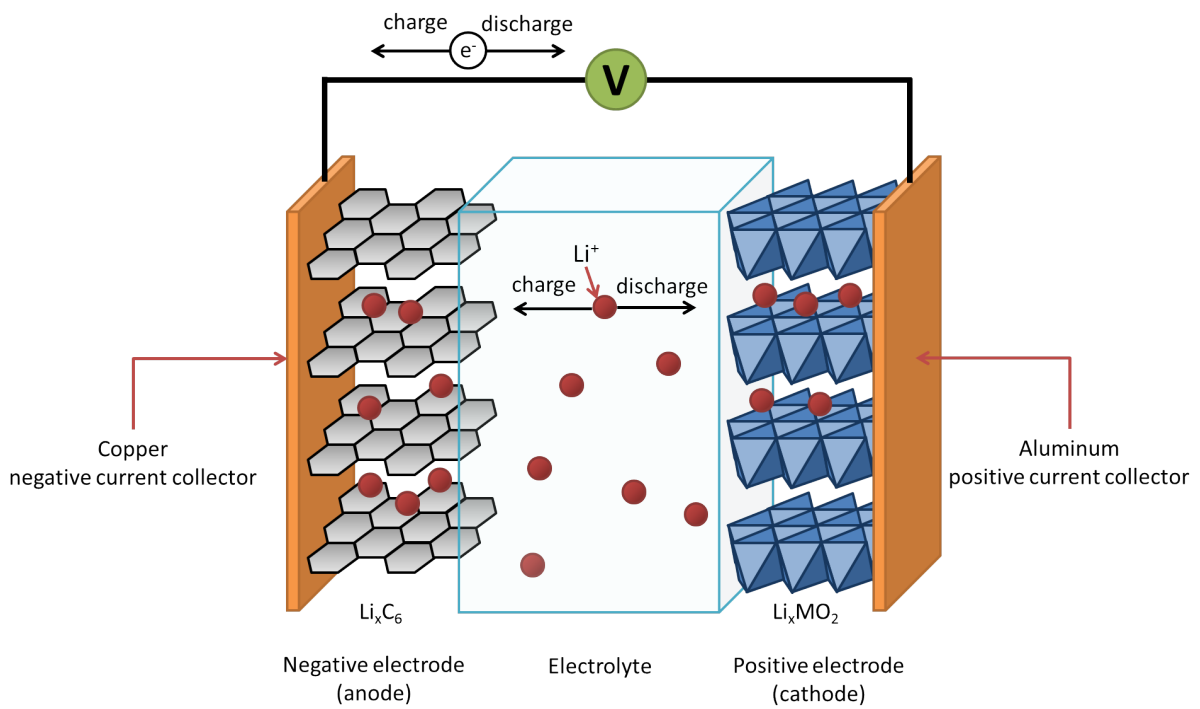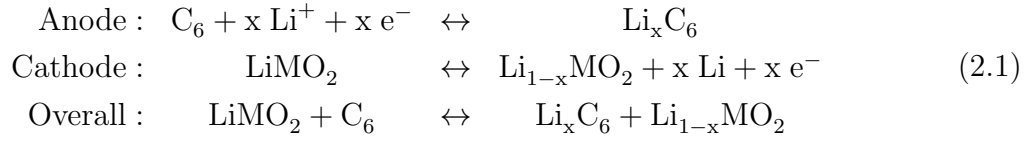

Figure 2.2: Schematic of a lithium-ion cell, based on ref. [15].

layers within the active materials. The active materials act reversibly as hosts and lithium ions are guests to form a sandwich structure [15].

$$
\begin{aligned}
\text{Anode}: && C_6 + x\,Li^+ + x\,e^- &\leftrightarrow& Li_xC_6 \\
\text{Cathode}: && LiMO_2 &\leftrightarrow& Li_{1-x}MO_2 + x\,Li + x\,e^- \\
\text{Overall}: && LiMO_2 + C_6 &\leftrightarrow& Li_xC_6 + Li_{1-x}MO_2
\end{aligned}
\tag{2.1}
$$

where $x = 0 \cdots 1$.

When a cell is cycled, lithium ions shuttle between the positive and negative electrodes by potential and concentration gradient [15]. Under cycling, lithium ions move through liquid electrolyte which soak porous electrodes and a separator (Section 2.5). The separator electronically and physically separates positive and negative electrodes to avoid short circuits by direct contact of electrodes (Figure 2.1). It is a permeable membrane that allows transport of lithium ions (Section 2.7). Both electrodes have current collectors, that are typically comprised of a copper sheet on anode and an aluminum sheet on cathode (Section 2.7). The current collectors are used to pass electrons from active material to the external circuit. Upon discharging the battery, the anode current collector receives an electron and sends it to the cathode via external circuit. In turn, charging sends electrons from the cathode current collector to an anode via the external circuit.

In addition to the main components of batteries described above, if we look closer look at the anode surface, we will see that Solid Electrolyte Interface (SEI) plays an important role as a passivation layer (Section 2.6). In this study, SEI is featured because of its exothermic characteristics during formation and decomposition at elevated temperatures.

In this work, numerical simulation is used to describe several exothermic phenomena in lithium ion batteries. The model consists of two parts: (1) conventional battery model for nominal operation condition, and (2) exothermic chemistry for elevated temperatures. A general overview of the conventional numerical model and a simulation for batteries is described in Section 2.8. The details of the exothermic chemistry considered in this study are summarized in Chapter 4. In order to validate the thermal model, simulation results are compared with experimental results from both literature and project partners.

2.2 Thermal runaway of lithium-ion batteries

2.2.1 Overview

Failures of lithium ion batteries are present in both energetic and non-energetic modes [17]. Both modes have failures for numerous reasons, including poor cell design (electrical or mechanical), cell manufacturing flaws, external abuse of cells (thermal, mechanical, or electrical), and inadequately designed and manufactured battery packs, protection electronics, chargers, and systems [17]. A typical non-energetic failure includes loss of capacity, internal impedance increase, activation of a permanent disabling mechanism such as a Current Interupt Device (CID), separator shutdown, electrolyte leakage, and cell swelling [17]. Some of the non-failure modes are associated with cell-aging mechanisms from irreversible reactions consuming lithium ions [17].

(a) Outside of a cell.
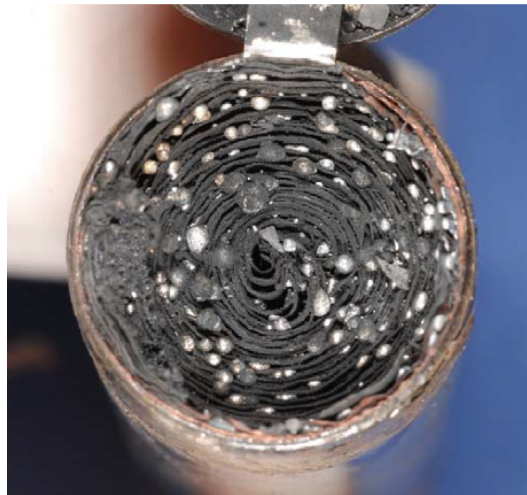
(b) Inside of a cell. Resolidified beads of melted aluminum can be observed.

Figure 2.3: An 18650 cell undergone thermal runaway from ref. [17].

In general, thermal runaway is defined as an energetic failure; rapid self-heating of a cell derived from any or a combination of exothermic chemical reactions in a cell [17]. The likelihood of initiating cell thermal runway is analogous to the likelihood of initiating many exothermic reactions, including SEI related reactions or the combustion of an electrolyte.

The self-heating of an anode with an electrolyte starts at a temperature in a range around 100 °C (Section 2.6.2). If a cell is brought to the initiating temperature of an exothermic reaction, it will eventually induce exothermic chain reactions and lead to the point where thermal runaway initiates [17]. Once a cell reaches a thermal runaway state, the internal temperature can exceed 600 °C for fully charged cells depending on the type of components [17]. Aluminum alloys have melting points as low as 548 °C, thus, damage to the internal current collector can occur as shown in Figure 2.3b.

In following subsections, we will review three failure modes: mechanical abuse, thermal abuse and electrical abuse.

2.2.2 Mechanical Abuse

The mechanical abuse of cells can cause an internal short circuit, which may initiate thermal runaway through localized cell heating which propagates through the entire cell [17]. This type of abuse can result in immediate failure, or can create a flaw in the cell that causes an internal cell fault after the cell has undergone numerous cycles [17].
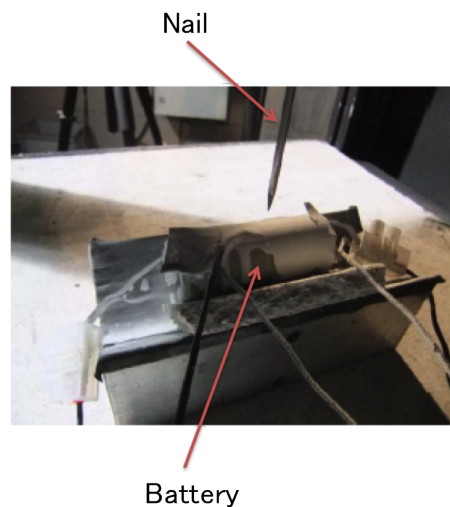

Figure 2.4: Experiment of nail penetration perpendicular to electrode surface of a cylindrical cell. Courtesy of ZSW.

Mikolajczak reported that when mechanical damage occurs at the edges of an electrode, it is significantly more likely to induce thermal runaway than cause damage perpendicular to electrode surfaces [17]. When crush damage is perpendicular to electrode surfaces, it may deform the electrodes and separator layers, but little to no internal short-circuiting occurs unless the separator is penetrated [17]. If the cell case is penetrated perpendicular to electrode surface during a nail test (Figure 2.4), it is likely that a low impedance internal

short circuit will occur between current collectors bridged by the penetrating nail, and cell heating may be too low to initiate thermal runaway [17].

However, if crushing or penetration occurs perpendicular to electrode edges, deformation is likely to result in a high impedance short circuit between electrode layers, and therefore initiating thermal runaway [17]. Maleki et al. studied the effect of nail penetration and crush locations that induce immediate thermal runaway [17; 18]. They found that pinch damage at the edge of electrodes was more likely to induce immediate thermal runaway than damage on the flat face of a prismatic cell [17]. If mechanical damage does not cause thermal runaway immediately or within hours of occurrence, it can still cause runaway when the cell continues to be cycled [17]. The point of mechanical damage can lead to electrode or separator degradation over cell cycles, and ultimately, severe lithium plating can occur, or a significant hole in the cell separator can develop [17]. These failure modes are most likely to occur during cell charging [17].

2.2.3 Thermal abuse

The most direct way to exceed thermal stability limits is to subject a cell to external heating [17]. External heating is generally examined during an oven test that applies heat to the cell exterior using a heater in an oven [19]. This type of test can provide both constant and ramp environment temperatures. While conducting oven tests with a commercial lithium ion battery, Mikolajczak et al. reported very few energetic failures were attributed to the long-term storage of the cells just above the self-heating point, 70 to 90 °C, even though self-sustaining thermal runaway can result from adiabatic environments or extended heat exposure times [17]. As for thermal abuse cell modeling, there are few modeling works relative to experimental works. So far, all models have decoupled the electrochemical model and only focus on thermal simulations even though these thermal models are also available in 3D. For example, Kim et al. presented both lumped and three-dimensional thermal models that include various side reactions inside a cell under high external oven temperature [20]. Each side reaction had an assigned activation energy which is proportional to the exponential of temperature, and had a factor limiting the extent of the reaction such as concentration of lithium ions. They showed that the surfaced area-to-volume ratio was a critical parameter for determining the onset of thermal runaway in an oven test.

DSC is also a common experiment used to investigate the thermal properties of each component within a cell at elevated temperatures. In comparison, accelerating rate calorimetry (ARC) is used to investigate the effects of thermal abuse on an entire cell similar to the oven test [13; 21; 22; 23; 24; 25]. Although both DSC and ARC are conducted in

adiabatic conditions and measure the temperature of a sample, the difference and advantage of a DSC experiment is that it can identify the exact heat release from a sample as compared to a temperature with reference. A detailed explanation of the theory behind this experiment will be reviewed in section 3.6.3.

Thermal runaway is not only induced by a mild temperature change in a cell during an oven or DSC/ARC test. It is also known that acute exposure of a cell to high temperature can also induce thermal runaway [17]. This relates to the propagation of runaways among cells within battery packs when combustion or other rapid increases of temperature were initiated by one of the cells.

In this study, several thermal abuse modes are modeled and simulated when coupled with an electrochemical model of a single battery. Detailed methods and results of this simulation are reviewed in Sections 3.6.3 and 5.2.

2.2.4 Electrical abuse

There are several ways in which electrically abused lithium ion cells can lead to cell thermal runaway reactions such as overcharge, over-discharge, and external short circuits.

Overcharge is associated with significant degradation of both the anode and the cathode. Once overcharged, it has been reported that plated lithium forms dendrites that can grow over time and cause internal short-circuiting on the anode side [17]. On the cathode side, overcharging can cause excess removal of lithium from the active material, such that their crystalline structure becomes unstable and leads to exothermic reactions. Over-discharge slightly differs from overcharge. Although simply over-discharging a cell to 0 V does not induce a thermal runaway reaction, it can cause internal damage to electrodes and current collectors such as dissolution of copper [17]. Over-discharging can also lead to lithium plating when the cell is recharged and the plating can ultimately cause thermal runaway through an internal short circuit due to further dendrite growth.

On the other hand, the mechanism of thermal runaway from an external short circuit is different from that of an over-charge/discharge associated with lithium plating or an internal short circuit. Upon an external short circuit, high rate discharging causes significant resistive heating within a cell at points of high impedance [17]. The internal heat could easily lead the cell to exceed thermal runway limits, converting all of its electrical energy to thermal energy. As cell size and capacity increases, the likelihood of internal impedance heating leading to thermal runaway also increases [17]. Larger cells transfer internal heat to their exterior and also have higher capacities. Therefore, they convert more electrical energy to internal heat [17].

Many experimental studies have been done for electrical abuse, however, similar to thermal abuse, at this time there are no simulations for a thermal model coupled with electrochemical model of a cell [17; 21; 26].

In this study, we investigate the external short circuit of a cell that represents the fastest and most energetic electrical abuse by the coupled thermal/electrochemical model. The heavy cycling of a cell in various C rates are examined. The methods and results of electrical abuse are shown in Section 5.3.

2.3 Anode materials and properties

2.3.1 Overview

Between the 1970s and the early 1980s, during a time of intensive secondary battery development, lithium-based batteries used lithium metal as an anode. One advantage of using lithium metal is its high specific capacity and excellent storage of lithium ions. However, safety issues caused industries to avoid lithium metal and, in turn, they have focused on lithium intercalation compounds. Carbon became a common intercalation anode material because of its light weight and electrochemical potential close to that of lithium metal [27]. When carbon reacts with electrolytes consisting of Propylene Carbonate, $C_4H_6O_3$ (PC) and it releases gas. However, this side effect can be suppressed by adding other solvents such as Ethylene Carbonate, $C_3H_4O_3$ (EC) [27]. Another disadvantage of using carbon materials is its irreversible capacity loss at the first charge cycle due to an irreversible reaction with the electrolyte. This reaction produces SEI, which passivates the carbon surface so that it is less likely to react with the electrolyte after the second cycle.

The structure of a carbon material greatly influences the performance of lithium intercalation capacity and potential. The schematics of carbon layer and graphite are shown in Figure 2.5. The basic structure of a carbon layer is comprised of a sheet structure with carbon atoms arranged in a hexagonal array (Figure 2.5a). Carbon layers are then stacked to form graphite, as shown in Figure 2.5b. The carbon layers form ABAB stacking which results in 2H graphite. The stacking disorder is not only a horizontal displacement of a carbon sheet but also includes situations where graphitic planes are parallel but shifted or rotated (turbostratic disorder) or those in which the planes are not parallel (unorganized carbon).

When lithium is intercalated in graphite, the disordered ABAB stacking transforms into the ordered AAAA structure. During the transformation, distinctive plateaus and steps are observed in thermodynamic potentials of the material. This plateau is related to
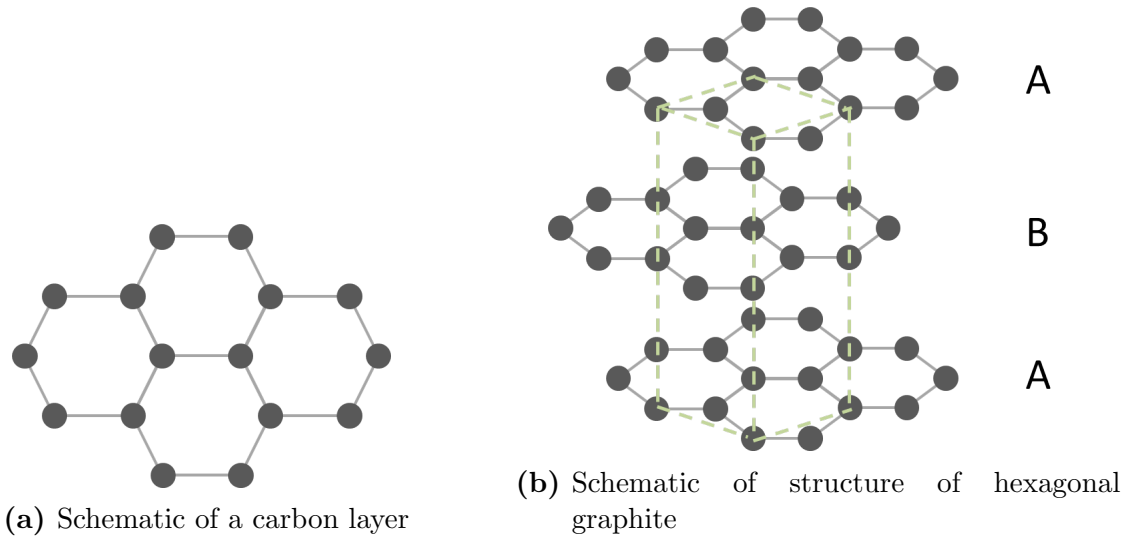
(a) Schematic of a carbon layer

(b) Schematic of structure of hexagonal graphite

Figure 2.5: Schematic of hexagonal structure of a carbon layer and graphite. Based on ref. [15]

lithium intercalation in distinct stages of graphite. Graphite used in a conventional lithium-ion cell shows less distinct stages, and petroleum coke and disordered materials have continuously smooth voltage profiles.

Carbon can be divided into three types: (1) soft carbon, (2) hard carbon, and (3) coke type materials [15]. This classification is based on the temperature of graphitization that removes turbostratic disorder and relieves strain on the material. Soft carbon is the material graphitized at temperature between 2000 °C and 3000 °C. Hard carbon is the material that cannot be graphitized even at a temperature higher than 3000 °C and typically it is prepared from phenolic resin. On the other hand, a coke type material is prepared at lower than 1000 °C.

The first commercial lithium-ion batteries created by the Sony Corporation utilized petroleum coke. Coke material has a capacity of 180 mAh/g and is stable with PC-based electrolytes. After the mid-1990s, most lithium-ion cells consisted of anodes with graphitic spheres, and, more specifically, a MCMB carbon. MCMB offers high specific capacity such as 300 mAh/g and low surface area which leads to low irreversible capacity and good safety properties. A detailed comparison of different anode properties are included in Subsection 2.3.2.

2.3.2 Different kinds of carbon and their properties

An ideal anode is composed of a material that has a high specific capacity without an irreversible capacity. Table 2.2 shows the properties of various carbons. The first commercialized anode, a petroleum coke, offers a reasonable specific capacity, but suffers from a high irreversible capacity. Graphite is low cost and has a good specific capacity ($\sim$ 350 mAh/g) but, similar to petroleum coke, it also shows a high irreversible capacity. MCMB carbons offer good values for both specific capacity and irreversible capacity, even though its energy density is not necessarily high ($\sim$ 30 mWh/cm^3). This is because low irreversible capacity is possibly correlated with a low surface area, which can result in intermediate energy density. For the same reason, spherical materials are preferred due to their low surface area. Hard carbon can offer a higher capacity than the theoretical specific capacity of carbon (LiC$_6$), 372 mAh/g, however, it is not commonly used in lithium-ion cells because of its very high irreversible capacity [15].

In our simulations, we assume that the anodes have MCMB carbon treated in 2800°C as shown by Reynier et al. [28]. Figure 2.6a shows Open-Circuit Voltage (OCV) against lithium metal of natural graphite and MCMB carbons treated under 750, 1000 and 2800 °C. As the figure shows, the MCMB 2800 °C offers a similar performance to natural graphite compared to the materials treated in lower temperatures. This representation shows that the MCMB 2800 °C has an ordered graphitoid structure compared to others which have rather disordered structures. Reynier et al. reported that the enthalpy of lithium intercalation, ΔH, is significantly more negative (i.e. intercalation is more exothermic) in a disordered material than an ordered material (Figure 2.6c). The ordered material has more dependence on lithium concentration in profiles of both ΔH and the entropy of lithium intercalation, ΔS, and shows a sharp drop in their profiles due to stage transitions (Figure 2.6b and 2.6c). The profile of ΔH shows that disordered carbons reaching -100 kJ/mol, is approximately -40 kJ/mol lower than that of ordered materials. This indicates that the material is thermally unstable, yet it provides more sites for low energy lithium.

**Table 2.2:** Properties of carbons for anode. Based on ref. [15]

Carbon	Type	Specific capacity (mAh/g)	Irreversible capacity (mAh/g)
KS6	Synthetic graphite	316	60
MCMB 25-28	Graphite sphere	305	19
MCMB 10-28	Graphite sphere	290	30
XP30	Petroleum Coke	220	55
Grasker	Carbon fiber	363	35
Sugar carbon	Hard carbon	575	215
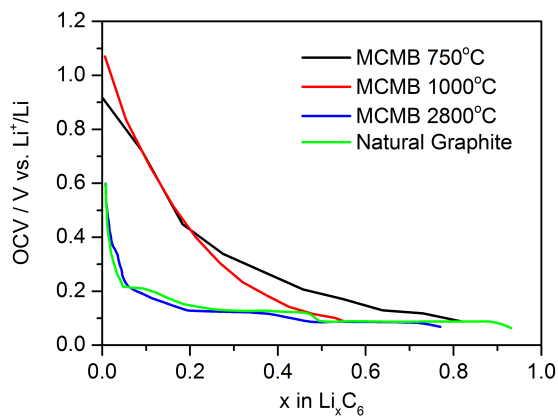
(a) Open-circuit voltage
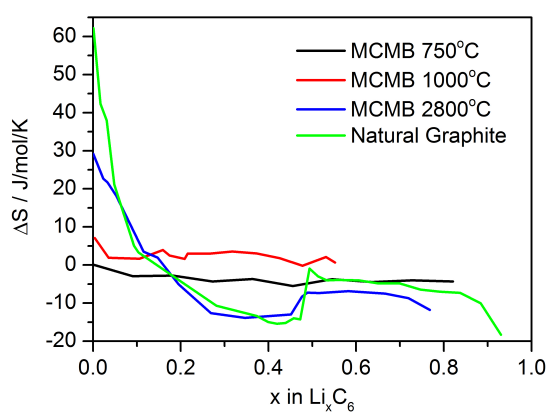
(b) Entropies of lithium intercalation.
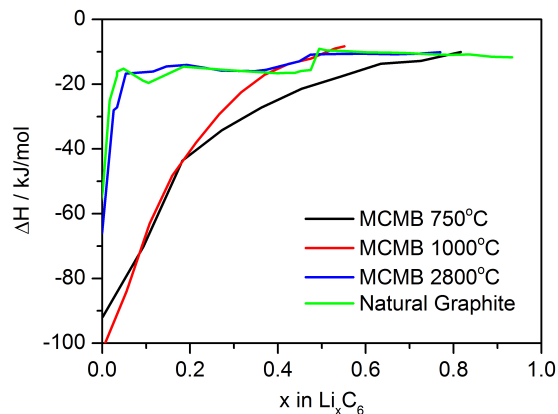
(c) Enthalpies of lithium intercalation.

Figure 2.6: Open-circuit voltage and entropy/enthalpy of lithium intercalation for natural graphite and MCMB carbons treated at 750, 1000 and 2800°C as a function of lithium concentration. Based on ref. [28]

2.4 Cathode materials and properties

2.4.1 Overview

Lithium-ion cells utilize a lithiated metal oxide as a cathode. A cathode's active material needs to satisfy the following basic requirements [15]:

- High free energy of reaction with lithium

- Large lithium-ion storage capacity

- Reversibility with lithium intercalation/extraction without structural change

- High lithium diffusivity

- High electronic conductivity

- No reactivity with electrolyte

- Low cost

In order to obtain high voltage and high energy density, the lithium exchange reaction must occur at a high potential against lithium. In addition, the material needs to have a large lithium-ion storage capacity to maintain a large specific capacity. Moreover, the less structural change accompanied with the lithium intercalation/extraction results in long cell life, high coulombic efficiency, and high energy efficiency. Furthermore, both lithium diffusivity and conductivity must be high to achieve an electron/ion exchange at a high rate through the active material. The cathode material also needs to be stable in a cell to prevent having an inessential reaction with the electrolyte. Finally, the material has to be at a decent price for commercialization.

There are many types of cathode active materials currently available in global markets. As briefly mentioned in Section 2.1, the three most common structures of these materials are: (1) a layered structure (e.g., LCO): (2) a spinel structure (e.g., LMO): and (3) an olivine structure (e.g., LFP). Table 2.3 and 2.4 summarize their advantages, disadvantages, and general properties. LCO was the cathode material first used in commercial lithium ion cells produced by Sony in 1991 and are still commonly available in today's battery market. LCO has a layered structure and offers high voltage; however it is also high in cost because cobalt is expensive. Nickel layered structure materials, $LiNiO_2$ or NCA, have a high specific capacity ($\sim$ 200 mAh/g) as well as high specific energy ($\sim$ 760 Wh/kg). On the other hand, spinel-type materials that contain manganese are low in cost, less toxic, and have the highest potential. Olivine-type materials are the newest materials in the market and include the LFP cathode, which was commercialized in 2005 by A123 Systems, LLC.

The LFP cathode has the is the lowest amount of exothermic decomposition although the potential of the cell is relatively low.

Table 2.3: Properties of cathode materials. Based on ref. [15] and [29]

Material	Structure	Specific capacity (mAh/g)	Potential vs. Li (V)
$LiCoO_2$	Layered	155	3.9
$LiNiO_2$	Layered	200	3.6
$LiNi_{0.8}Co_{0.15}Al_{0.05}O_2$	Layered	200	3.8
$LiMn_2O_4$	Spinel	120	4.0
$LiFePO_4$	Olivine	170	3.45

Table 2.4: Advantages and disadvantages of cathode materials. Based on ref. [29]

Material	Advantages	Disadvantages
$LiNi_{0.8}Co_{0.15}Al_{0.05}O_2$	Performance is well established High capacity High voltage Excellent high-rate performance Moderate safety (oxygen release)	High cost of Ni and Co Potential resource limitations
$LiMn_2O_4$	Low cost High operating voltage No resource limitation Moderate safety (oxygen release) Excellent high-rate performance	Mn solubility issue Low capacity
$LiFePO_4$	Moderately low cost No resource limitations Excellent safety (no oxygen release)	Low operating voltage Low capacity

In this study, olivine-type materials (LFP) and blended materials (LMO and NCA) are examined. Details of related materials are also explained in the following sections.

2.4.2 Olivine-type $LiFePO_4$ cathode material

The olivine-type cathode material is relatively new. The group of Goodenough first reported using a phospho-olivine material for a cathode in 1997 [30]. The phospho-olivine material has an orthorhombic structure (space group Pnma). Figure 2.7 shows the structure of $LiFePO_4$, which is one of the most commonly used phospho-olivine cathode materials and is also known as triphylite. In $LiFePO_4$, Li^+ and Fe^{2+} occupies octahedral

sites and P is in tetrahedral sites [29]. Lithium ions diffuse along the b-axis where LiO_6 octahedra share edges along tunnels through the b-axis. One of unique characteristic of this type of material is that its potential is independent of lithium concentration (x in Li_xFePO_4). This can be seen in the flat voltage profile shown in Figure 2.8a. As for the entropy and enthalpy of lithium intercalation (Figure 2.8b and 2.8c), Dodd reported that both the entropy and enthalpy have three characteristic regions [31]. The first region is near $x = 0$ where lithium is first intercalated to the cathode material. In this region, the entropy and enthalpy increase very slightly. The second region is in $0.05 < x < 0.85$. The entropy gradually decreases down to -14 J/mol·K and the enthalpy keeps a constant value at approximately -331 kJ/mol. The third region is in $x > 0.85$ where both the entropy and enthalpy show substantial changes that result in a sharp drop of OCV. Andersson et al. confirmed that the plateau in OCV indicates a two-phase reaction, triphylite and $FePO_4$ (heterosite), by X-ray diffraction and Mössbauer spectroscopy (Equation 2.2) [32].
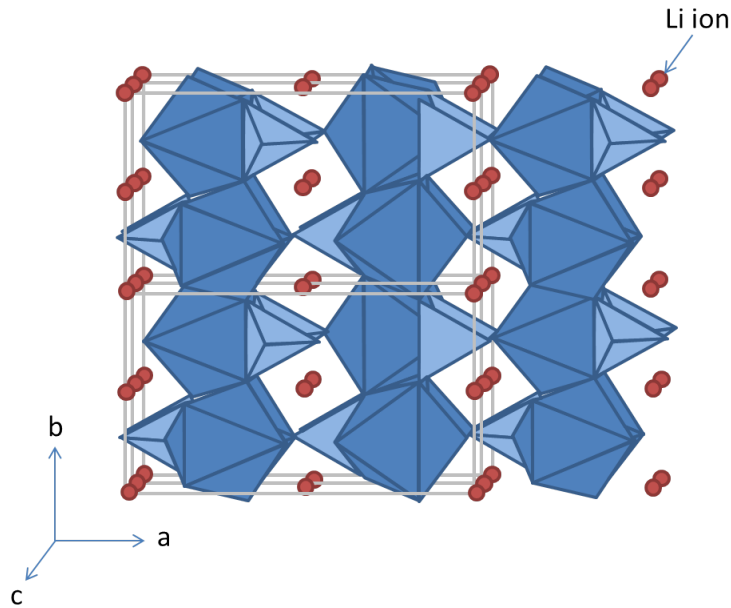
$$LiFePO_4 \leftrightarrow FePO_4 + Li^+ + e^- \tag{2.2}$$

Figure 2.7: Schematic of olivine type $LiFePO_4$ structure. Based on ref. [33]

Still, the detailed mechanism behind a lithium intercalation/extraction reaction in an olivine material is not completely understood. The shrinking core model is a commonly used method for understanding this mechanism [34]. During discharge, lithium is first inserted into $FePO_4$ forming a homogeneous solid-solution of $Li_\alpha FePO_4$, where α is close to zero. Then, once it is further along in the discharge process, a lithium-rich ($Li_{1-\beta}FePO_4$)

(a) Open-circuit voltage

(b) Entropies of lithium intercalation.

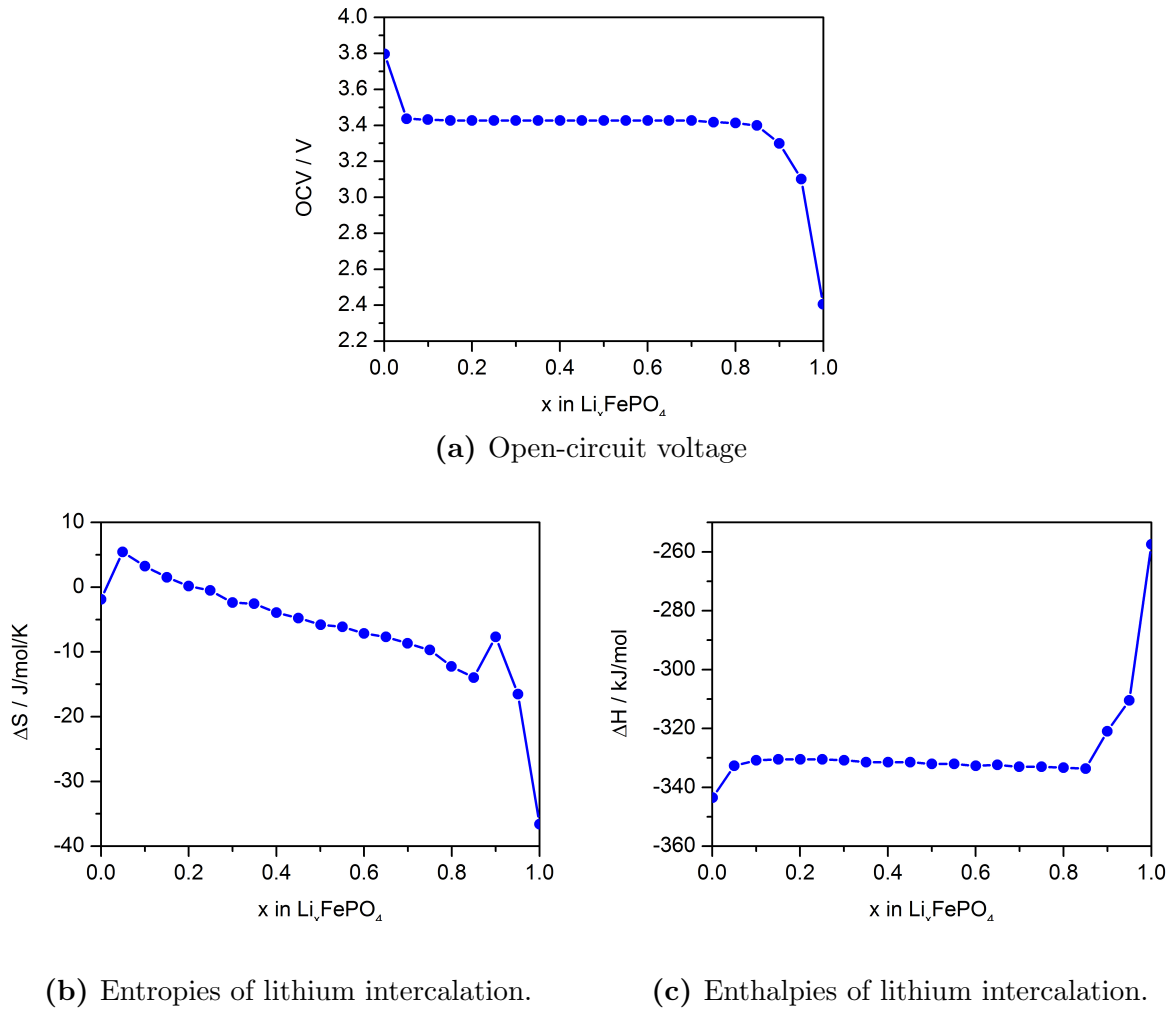**(c)** Enthalpies of lithium intercalation.

Figure 2.8: Open-circuit voltage and entropy/enthalpy of lithium intercalation for $LiFePO_4$ as a function of lithium concentration. Based on ref.[31].

shell appears on the surface and covers a $Li_\alpha FePO_4$ core. As the reaction continues, the shell grows toward the core and the core shrinks until it is completely converted to $Li_{1-\beta}FePO_4$. $LiFePO_4$ is produced by further lithiation at the very end of the discharge process. In case of the charge process, the entire procedure is reversed [29]. However, this is a controversial model due to anisotropy of lithium diffusion in $LiFePO_4$. The study with Transmission Electron Microscopy (TEM) shows that the domains of $LiFePO_4$ and $FePO_4$ align along the ac-plane in a partially delithiated sample [35]. This means that the phase transformation moves in the direction of the a-axis, and not to the center of the core. Another study by Laffont et al. shows that $LiFePO_4$ exists only at the edges of $FePO_4$ [36]. In addition, no disordered regions (i.e., solid-solution phase, $Li_\alpha FePO_4$) at the phase boundaries were found. So far, it is said that the shrinking core model may be applicable on a large scale with secondary particles even though it is clear that the model cannot apply to primary particles [29].

The thermal stability of the $LiFePO_4/FePO_4$ system is a particularly attractive feature [29]. At elevated temperatures, $FePO_4$ transforms to a thermodynamically favored trigonal form (α-quartz structure). Its progress proceeds without the evolution of oxygen, although the reaction is irreversible and leads to capacity loss [37]. Oxygen release is not favorable because of a possible reaction with electrolyte that can release high amount of heat. This is a unique feature of olivine material, making it more attractive than other metal oxides, which release oxygen at high temperatures or a high state of charge condition.

On the other hand, $LiFePO_4$ material has a lower energy density due to a small density (3.6 g/cm^2) compared to layered oxides or spinels (approximately 5 g/cm^2). The potential against lithium is also lower than that of oxides and spinels.

### 2.4.3 Spinel-type $LiMn_2O_4$ cathode material

In a lithiated state, a Li-Mn-O system forms a stable spinel structure. The stoichiometric spinel, $LiMn_2O_4$, can be easily synthesized in air by lithium and precursors with manganese [29]. Figure 2.9 shows a schematic of this structure (cubic space group of Fd3m). Lithium ions are located at tetrahedral 8a sites and manganese is located in octahedral 16d sites in a ccp array of oxygen anions (Figure 2.9b). Lithium is diffused through vacant tetrahedral and octahedral sites in the three-dimensional structure.

Theoretically speaking, $Li_xMn_2O_4$ can cycle over a stoichiometry range of $0 \geq x \geq 2$, giving total specific capacity of 285 mAh/g [29]. However, a large anisotropic volume change with the formation of $Li_2Mn_2O_4$ leads to irreversible particle disintegration and loss of connection within the composite electrode. This process happens below 3 V against Li/Li^+ and even a few times of cycling in this region can largely damage the material and result in capacity fade or structural strain/failure. In contrast, above 4 V, volume change is small enough to keep reasonable reversibility even though the range of lithium stoichiometry is limited to $0 \geq x \geq 1$. For this reason, most studies focus on a plateau around 4 V, as shown in Figure 2.10a. The theoretical specific capacity of this range is 148 mAh/g, however, in practice, it is approximately 120 mAh/g (Table 2.3). This is because it is impossible to extract all lithium ions from the active material [29].

Manganese-based materials have been used in industrial and commercial applications because of their low cost and good electrochemical properties. However, they have one drawback, their capacity fades even at a 4 V plateau due to multiple processes such as: (1) irreversible side reactions with the electrolytes due to the high potential [40; 41], (2) evolution of oxygen, (3) dissolution of manganese [15], (4) production of tetragonal
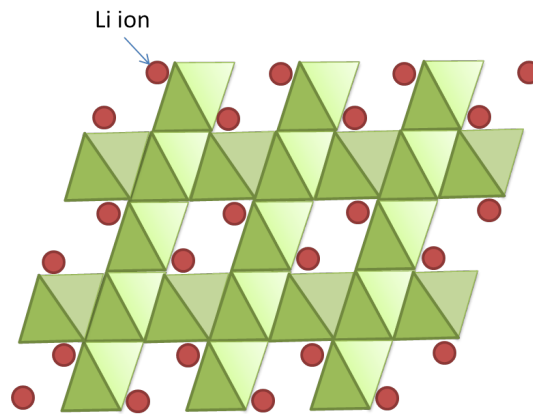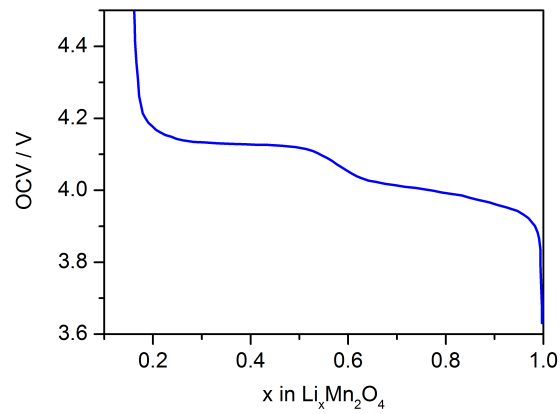
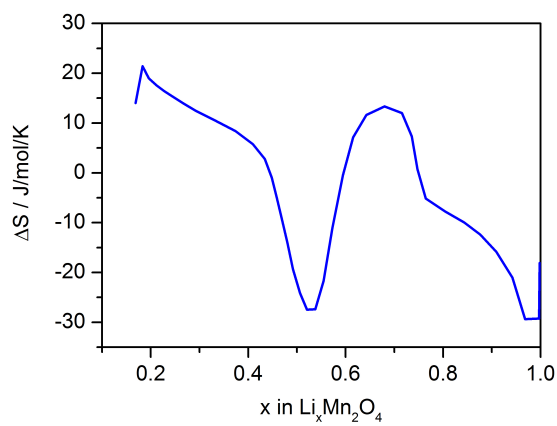**(a)** Schematic of spinel-type $LiMn_2O_4$ structure. Based on ref. [38].
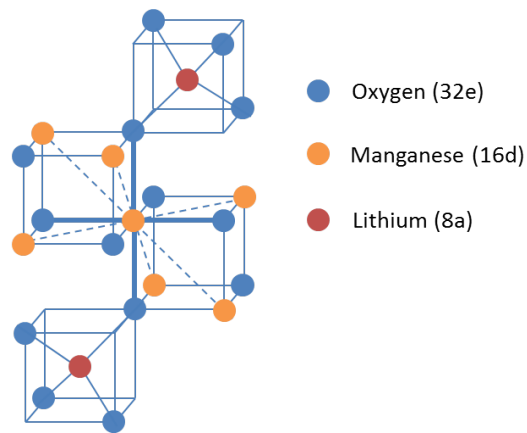
(b) Schematic of unit cell of $LiMn_2O_4$.
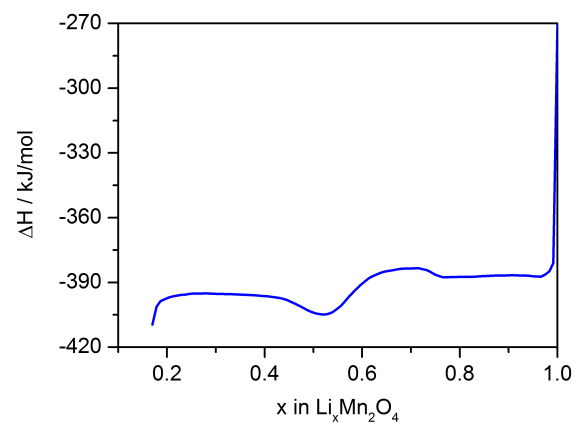
Figure 2.9: Schematics of $LiMn_2O_4$ structure. Based on ref. [38].

(a) Open-circuit voltage

**(b)** Entropies of lithium intercalation.

(c) Enthalpies of lithium intercalation.

Figure 2.10: Open-circuit voltage and entropy/enthalpy of lithium intercalation for $LiMn_2O_4$ as a function of lithium concentration. Based on ref.[39].

$Li_2Mn_2O_4$ on particle surfaces with high discharge rates [29], and (5) Jahn-Teller distortion in discharged cells [15]. Capacity fade in spinel cells is remarkable when cells are stored in either a charged or discharged state. Without additional treatments, spinel cells will lose over 20% of the capacity within three weeks at 50 °C. One of the most common treatments against capacity fade is an inorganic coating of Li_2CO_3 or $LiCoO_2$. At 50 °C, a coated spinel reduces capacity loss to $1 \sim 3$ % per week.

Alternatively, capacity loss from cycling is controlled by lithium substitution and additive substances which increase the oxidation state of manganese, $Li_{1+x}Mn_{2-x}O_4$. These control methods decrease the lattice parameter, a, which closely relates to the amount of capacity loss during cycling [29]. Almost all commercial manganese oxide spinels consist of lithium-substituted material because the cycling behavior of $Li_{1+x}Mn_{2-x}O_4$ is much better than that of $LiMn_2O_4$. In practice, capacity loss during cycling is still exhibited particularly at high temperatures over 55°C even with a lithium-substituted manganese oxide material. This is a major drawback for automobile applications. The dissolution of manganese is the cause of capacity loss and is associated with Mn^{3+} disproportionation in the presence of acidic $LiPF_6$ components/organic carbonate electrolyte solutions (Equation 2.3) [29].

$$2\,Mn^{3+}(solid) \rightarrow Mn^{4+}(solid) + Mn^{2+}(solution) \tag{2.3}$$
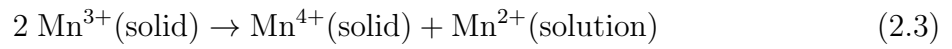
This significant problem is not limited to the cathode side. The dissolved Mn^{2+} can diffuse to the anode side being reduced. This may increase the charge-transfer resistance and disrupt the critical SEI layer [42]. However, it is also known that the dissolution of manganese is suppressed when a manganese oxide spinel is mixed with layered materials such as Nickel Manganese Cobalt Oxide (NMC) or NCA [43]. The details of blended cathodes will be described in Section 2.4.5.

2.4.4 Layered $LiNi_{0.8}Co_{0.15}Al_{0.05}O_2$ cathode material

$LiNi_{0.8}Co_{0.15}Al_{0.15}O_2$, NCA, is the most commonly used cathode material related to layered $LiNiO_2$. This is because the presence of aluminum and cobalt greatly improve the cathode's thermal stability and electrochemical properties, even though it is still inherently less safe than olivine-type materials such as LFP. However, NCA offers high specific capacity and good power capability, making it very suitable for automobile applications (Table 2.3).

Figure 2.11 shows a schematic of layered transition metal oxides. Lithium ions are located in the $3a$ site and other ions form a hexagonal symmetric structure known as a space group

R-3m. This type of arrangement is also known as O3 in layer notation, and indicates that there are three layers per unit cell and the lithium ions are octahedrally coordinated [29].
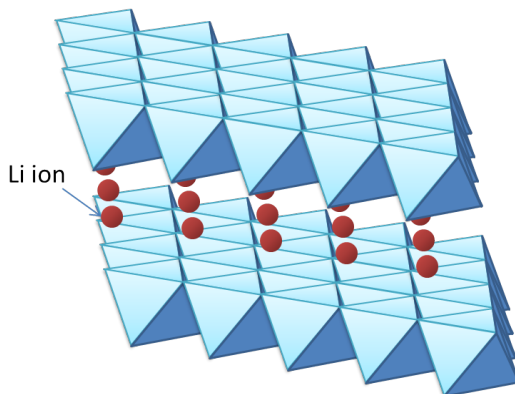

Figure 2.11: Schematic of layered type structure.

The open-circuit voltage (OCV) of an NCA material is shown in Figure 2.12a. Experimental results by Yang et al. show that the OCV of NCA has a unique slope throughout its lithium intercalation range without having a plateau different from LFP or LMO [44]. Entropy of lithium intercalation varies between -8 and 2 J/mol·K and exhibits 1/4 less variation than those of LFP or LMO, yet, the variation of enthalpy is within the same range (Figure 2.12b and 2.12c). The relatively flat ΔS profile is considered to be the first order transition suppressed by the substitution of cobalt and aluminum [44]. In fact, the variation of entropy with lithium intercalation relates to the rate of lattice disorders. The flat ΔS profile compared to that of LMO or LFP indicates that the structure change is relatively small although it still exist in NCA. XRD studies reported that contraction is observed on the a-axis and the c-axis expands along the charge process for $Li_xNi_{0.8}Co_{0.2}O_2$, which is the same structural material as NCA. The dimension changes are almost linear to the change in stoichiometry of lithium ions, x [44].

The drawbacks of NCA cathode materials are significant capacity fade and impedance rise during cycling [45]. Studies with accelerated cycling tests at high temperatures show that NCA cathode materials suffer drastic power fading when electrochemically in active NiO type phase rock-salt structures (Fm$\bar{3}$m) form at the surface. These studies also reported that overcharged (i.e., highly delithiated) Ni-rich NCA materials form a complex structure with both a layered R$\bar{3}$m core and a rock-salt structure at the surface [46]. The layered R$\bar{3}$m structure of NCA is thermally unstable particularly in the charged state. The unstable layered structure results in phase transition to the rock-salt structure (Fm$\bar{3}m$) via a disordered spinel structure (Fd$\bar{3}$m) releasing heat. It is known that the phase transition is associated with oxygen evolution which can react with electrolyte to accelerate thermal runaway [47]. However, similar to spinel-type $LiMn_2O_4$ materials, it is also known that NCA mixed with spinel can suppress heat generation [48].
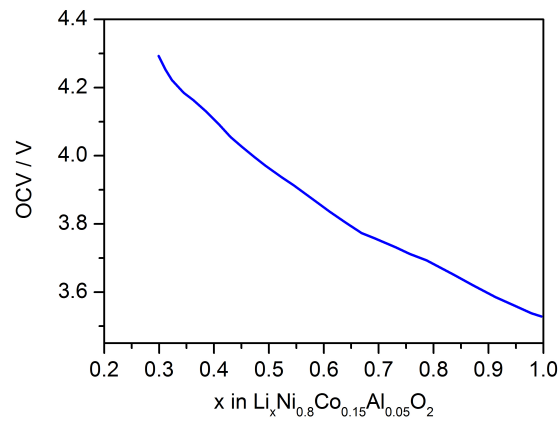
(a) Open-circuit voltage
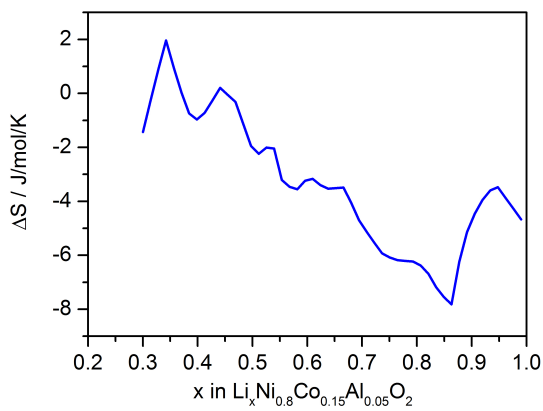
(b) Entropies of lithium intercalation.
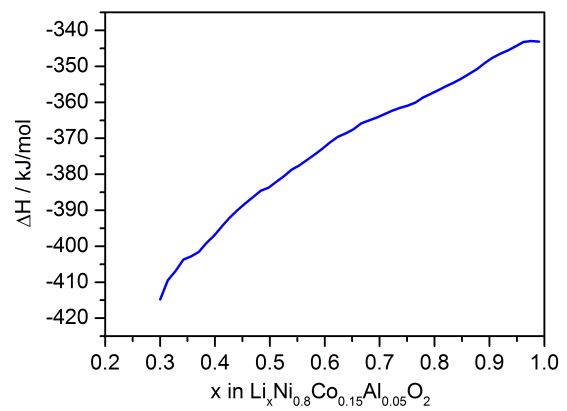
(c) Enthalpies of lithium intercalation.

Figure 2.12: Open-circuit voltage and entropy/enthalpy of lithium intercalation for $LiNi_{0.8}Co_{0.15}Al_{0.15}O_2$ as a function of lithium concentration. Based on ref. [44].

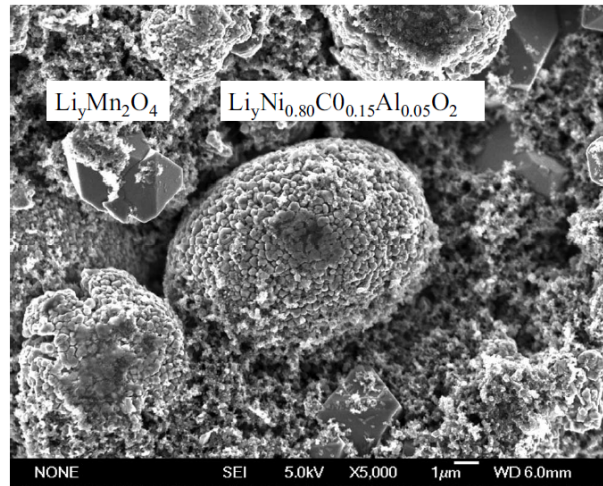### 2.4.5 Blended LiMn$_2$O$_4$ and LiNi$_{0.8}$Co$_{0.15}$Al$_{0.05}$O$_2$

Blended cathode active material is comprised of a physical mixture of several distinct lithium intercalation compounds [43]. The purpose of blending is to achieve a balanced performance compared to individual materials. In a blend of LMO and NCA, NCA offers a higher capacity and longer life, although the thermal stability of NCA is worse than that of LMO [49], [50]. On the other hand, LMO offers higher operating voltage, better rate capability, and cheaper cost. A blend of these two materials draws attention because when combined together the two materials can compensate for their drawbacks. Compared to pure NCA, NCA/LMO blend is better in cost, energy, power, and safety. The only exception is that a NCA/LMO blend has a shorter storage life, which can easily outweigh its other merits in certain applications [43].
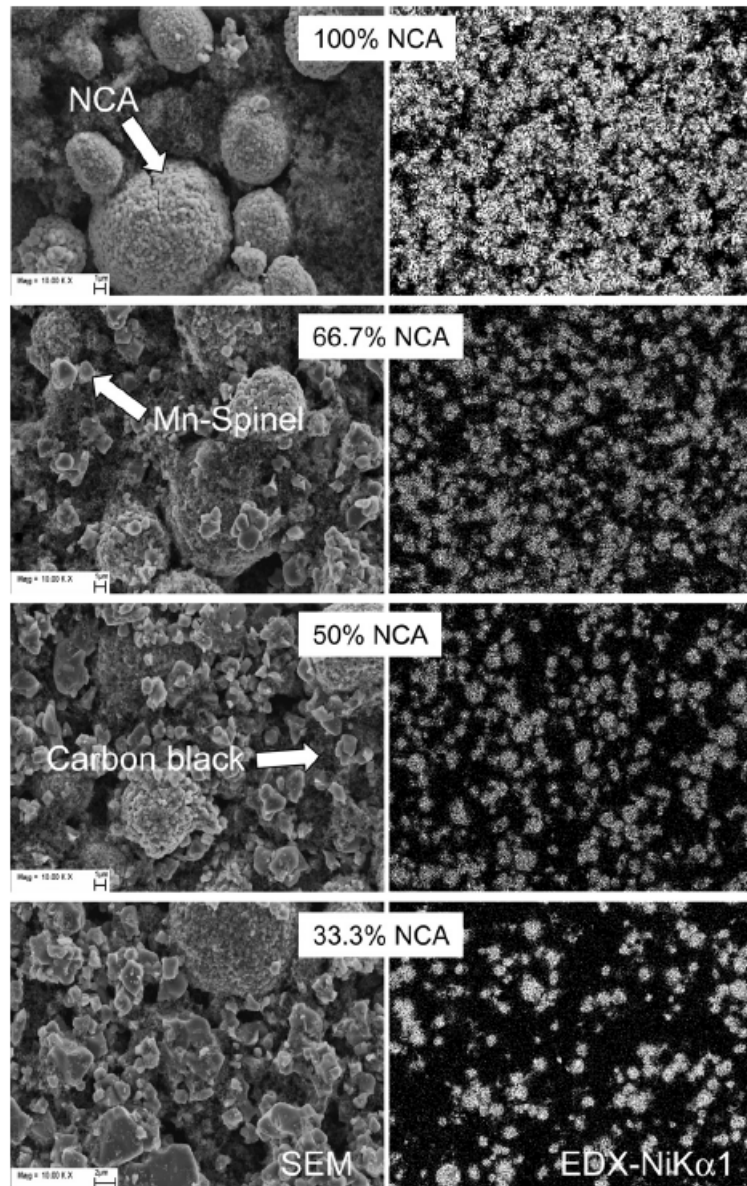
As shown in the scanning electron micrograph by Albertus et al. (Figure 2.13a), it is also possible to see visual distinctions between the two materials in a blended cathode. LMO has crystal angular shape, and in contrast, NCA has round ball-like shape. It is obvious when different blend rate materials are compared to each other (Figure 2.13b). Tran et al. showed comparison of four different types of the blends (NCA ratio of 100%, 66.7%, 50% and 33.3%) as well as nickel distributions by energy dispersive X-ray spectroscopy mapping (EDX).

As for the performance of a blended cathode, Albertus et al. studied the LMO/NCA blend (1:1 wt%) and compared voltage profiles of pure materials at various Normalized battery currents (C-rates) utilizing theoretical simulations [51]. They reported that the blended cathode shows a higher average voltage at a high C-rate (5C) than pure NCA. Similarly, another study shows that a blended cathode with 33.3% of NCA offers the best discharge behavior at 5C relative to other mixture ratio (Figure 2.14a) [48]. SOC behavior in each compound (LMO:NCA 1:1 wt%) indicates that both materials behave as if they were pure materials; and that the charge in LMO and NCA phases are independent of each other (Figure 2.14b). Moreover, Figure 2.14b shows that compared to LMO, NCA contributes more to cell capacity when total SOC is lower than 40%. On the other hand, LMO acts as the primary contributor to the cell capacity when the total SOC is larger than 40%. Figure 2.15 shows rate performance of a blended material (LMO:NCA 1:1 wt%). A kink in cell potentails in a range of C/25 ∼ 5 C at 0.6 normalized capacity can be considered as the boundary when NCA dominant phase shifts to LMO phase [48]. Furthermore, Tran et al. also reported that the blended material offers improved thermal stability relative to NCA [48].

In this study, this kind of LMO/NCA blend material is inclded in the battery and runaway simulation. A detailed method of modeling will be discussed in Section 3.5.4.

(a) Scanning electron micrograph from ref. [51].

(b) Scanning electron micrograph in different blend ratio from ref. [48].

Figure 2.13: Scanning electron micrograph of blend cathode active material, $LiMn_2O_4$ and $LiNi_{0.8}Co_{0.15}Al_{0.15}O_2$

(a) Rate performance of blend electrodes (NCA/LMO) in different C rate in range from C/5 to 5C.

(b) SOC of each compound as a function of overall SOC of blend material (LMO:NCA 1:1 wt%).
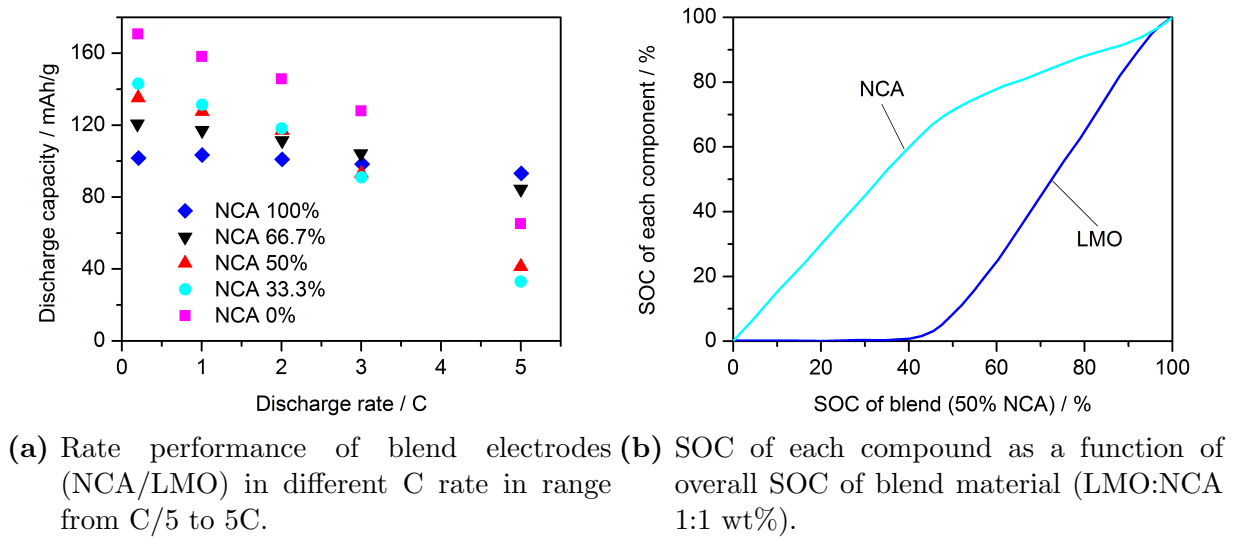
Figure 2.14: Rate performance and state of charge (SOC) from ref. [48].
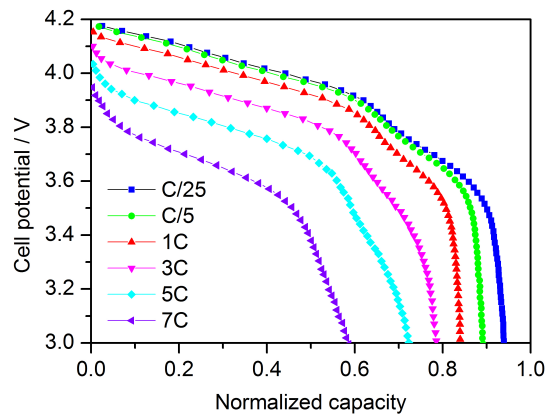
Figure 2.15: Experimental rate performance of blend material (LMO:NCA 1:1 wt%) from ref. [51].

2.5 Electrolyte

2.5.1 Overview

There are four types of electrolytes utilized in lithium-ion cells: gel, polymer, solid and liquid [15]. A gel electrolyte is an ionically conductive material in which salt or solvents are mixed or dissolved in a high molecular weight polymer. One advantage of a gel electrolyte is to be able to prevent battery leakage by using a polymer which can absorb a liquid electrolyte. On the other hand, polymer electrolyte is a liquid- and solvent-free high molecular weight polymer with dissolved salt which provides ionic conductivity [15]. In terms of safety, polymer electrolytes are less volatile due to their non-flammable solvents.

Solid electrolyte is made up of a solid state material that is ionically conductive. Recently, researchers have intensively studied an all-solid battery consisting of solid electrolyte [52; 53; 54; 55]. The solid electrolyte has excellent safety properties without having a volatile component, and exhibits extremely high lithium ionic conductivity at room temperature [54]. However, due to practical concerns with conductivity, durability and issues with the interface between electrolyte and electrodes, most of commercialized lithium ion cell contains liquid electrolyte.

2.5.2 Liquid electrolyte

Liquid electrolytes are almost completely absorbed in porous electrode and separator materials. There are two types of liquid electrolytes, aqueous and non-aqueous. Due to the use of lithium, a non-aqueous electrolyte is utilized in lithium ion batteries to avoid hazardous chemical reactions. These types of electrolytes are usually solutions of one or more lithium salt in mixtures of two or more organic solvents [56]. The rationale behind a mixed solvent is to meet the diverse requirements of a battery that are rarely satisfied with individual compounds. Oftentimes, solvents with very different chemical properties are mixed and utilized simultaneously [56]. In contrast, a mixture of salts is rarely used because performance improvements have not been demonstrated and the types of anion are limited. These limitations come from the small ionic radius of a lithium ion which cases most lithium salts to not meet the minimum solubility requirements in low dielectric media [56]. Most salts that meet minimal solubility standards are anions composed of a simple anion core and stabilized by a Lewis acid agent [56]. Lithium hexafluorophosphate, $LiPF_6$, is the most commonly used salt that offers high ionic conductivity ($< 10^{-3}$ S/cm), high lithium ion transference (~ 0.35), and reasonable safety properties [15]. F^- in $LiPF_6$ is complexed by the Lewis acid PF_5. We assume that the target cells of this work also utilize $LiPF_6$.

An ideal liquid electrolyte solvent must meet the following minimum criteria [56]:

- High solubility for salts to have sufficient concentration (high dielectric constant)

- Low viscosity (fluid) to manage ion transport

- Inert to all cell components including charged surfaces of electrodes

- A liquid state that stays within an operative temperature range

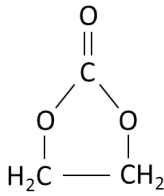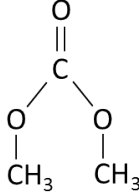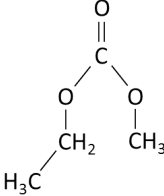- Safe (high flash point), nontoxic and reasonably priced

For lithium ion batteries, limitations for solvents depend on the nature of reducing anodes and oxidizing cathodes [56]. Any solvent with active protons is set aside in spite of their excellent power because a reduction of protons generally occurs in a potential range of 2.0 - 4.0 V versus lithium, and that is within same range as the operating voltage of lithium ion cells. Therefore, the solvent must be aprotic. At the same time, the electrolyte solvents must be able to keep sufficient amounts of lithium salt. Thus, only those with polar groups such as carbonyl (C=O), nitrile (C≡N), sulfonyl (S=O), and ether-linkage (-O-) can be qualified [56].

Over the years, many types of polar solvents have been investigated. At this time the most commonly used solvents these days are organic esters and ethers [56]. While the industry first focused on PC, current formulations consist of EC mixed with acyclic alkyl carbonates such as Dimethyl Carbonate (DMC), Ethyl Methyl Carbonate (EMC) and Diethyl Carbonate (DEC). The shift from PC happened because PC causes degradation in graphite electrodes co-intercalating with lithium and lead to exfoliation (i.e. poor cycling efficiency) [15]. EC was first suggested as an electrolyte co-solvent by Elliot in 1964 due to its high dielectric constant and low viscosity [57]. However, the battery community was not interested in this solvent because of its high melting point ($\sim$ 36 °C). This problem was not solved until 1970 when Scrosati et al. found that the melting point can be suppressed in the presence of a solute [56; 58]. EC established its position as the battery electrolyte when Dahn and co-workers reported fundamental differences between PC and EC in lithium ion intercalation/deintercalation with graphitic anodes [56]. EC was found to form a passivation film, SEI, on a graphitic anode. This film prevented sustained electrolyte decomposition on the anode although this kind of surface protection was not realized with PC. In past decades, the SEI layer captured the attention of researchers, however, it is still not well understood. Details on this research topic will be reviewed in Section 2.6.

Many studies were employed to find the co-solvent of an EC based electrolyte that satisfies oxidative stability up to $\sim$5 V against lithium for lithium ion cells with graphitic anodes and metal oxide cathodes [56; 59; 60; 61]. The first successful mixture shown in a published article that meet this standard was a mixed electrolyte of a linear carbonate (DMC) cosolvated with EC [56; 62; 63]. As shown in Table 2.5, DMC is a material with relatively low boiling points, low viscosity, and a low dielectric constant. DMC was found to suppress the melting temperature of EC in addition to providing low viscosity (higher ion conductivity). Furthermore, the best feature of a mixed EC:DMC electrolyte is its wide electrochemical stability window which is stable on a spinel cathode surface up to 5.0 V [56]. Interestingly, it is still unclear why this improvement can be achieved considering the failure of anodic stability with ether-based electrolytes, EC:PC.

Other formulations based on a mixture of EC with a linear carbonate, such as EC:EMC and EC:DEC [64; 65], have also been investigated, however, no significant differences relative to the DMC mixture were observed in regards to electrochemical characteristics [56]. Currently, most of commercialized lithium ion cells consist of EC based mixtures with these linear carbonates.

Table 2.5: Characteristics of organic solvents based on ref. [15]. T_m: melting point, T_b: boiling point, M.Wt.: Molecular weight.

Characteristics	EC	DMC	EMC
Structure			
T_m (°C)	39	4	-55
T_b (°C)	248	90	109
Density (g/ml)	1.41	1.07	1
M.Wt.	88.1	90.1	104.1

In this study, we utilize electrolytes containing EC:DMC and EC:EMC.

2.6 Solid Electrolyte Interface (SEI)

2.6.1 SEI formation

SEI is the passivation film which spatially separates solvents from the electrode while maintaining ionic conductivity so lithium ions can have a path towards the electrode. SEI covers carbon particles and contains inorganic components such as LiF on the cross section of the electrode and edges of graphite particles [66]. On the other hand, SEI on graphene sheets contain soft organic compounds (Figure 2.16).

The SEI layer is primarily observed on the anode side because there is no practical solvent that is thermodynamically stable with lithium or graphitic anode, Li_xC_6, near 0 V against lithium [15]. The thickness of a SEI may vary from tens to hundreds of Å [66; 67; 68]. The process of SEI formation is irreversible, exothermic and, at the same time, a loss of capacity is observed due to lithium consumption primarily on the cell's first cycle [15; 69]. The amount of irreversible capacity loss depends on both the formulation of the electrolyte and the types of electrodes [70]. The reaction occurs at the surface of
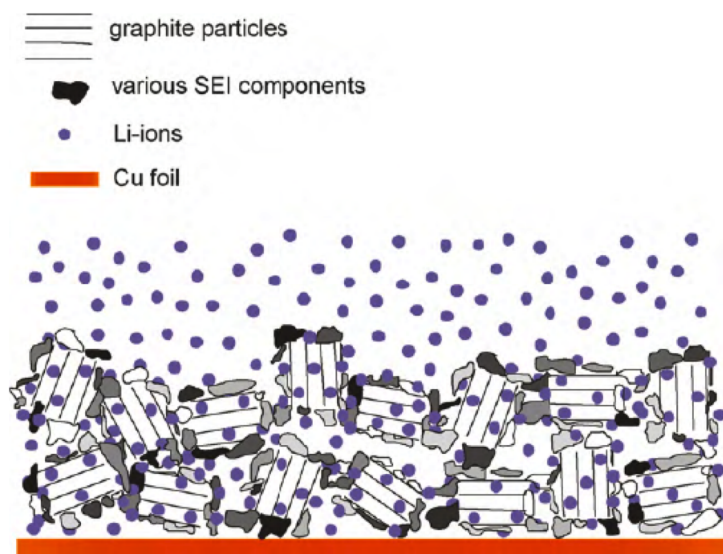
Figure 2.16: Schematic of a lithiated graphite composite electrode covered by inhomogeneous SEI from ref. [66]. Darker shades SEI: inorganic, lighter shades SEI: organic.

an active material, therefore, electrodes with low specific surface areas typically offer lower irreversible capacity. Cells with EC-based electrolytes offer low capacity fade, low irreversible capacity, and high capacity as described in previous Section 2.5. Aurbach et al. attributed these characteristics the the EC-based SEI film that is formed with a minimum amount of lithium [65]. The proposed chemical composition of the SEI by EC consists primarily of lithium ethylene carbonate, $(CH_2OCO_2Li)_2$ (Figure 2.17), with related reaction products such as Li_2CO_3 or $LiOCH_3$ [15; 65; 71].
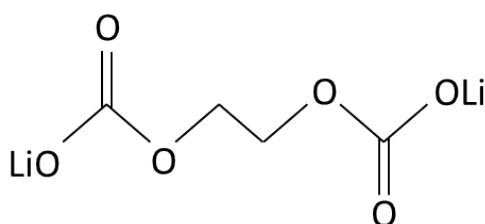
Figure 2.17: Main chemical composition of SEI (lithium alkyl carbonate) based on EC electrolyte.

Although solvents mixed with EC, esters or alkyl carbonates, such as DMC or EMC, can also form a stable passivation layer, it is known that a layer formed by esters or alkyl carbonates is usually suppressed due to the presence of EC [72]. Thus, most studies in terms of SEI focus on SEI formation as a product of the reaction between EC and lithium ions [73]. Aurbach et al. suggest the following reaction:

$$C_3H_4O_3(EC) + 2e^- + 2Li^+ \rightarrow (CH_2OCO_2Li)_2 + C_2H_4 \qquad (2.4)$$
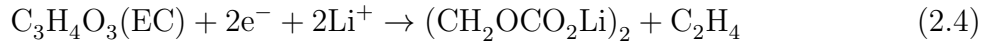
Knowledge about the chemical composition of SEI is more or less clear due to intensive surface spectroscopic investigations by Aurbach and co-workers on carbonaceous anodes in various non-aqueous electrolytes that utilize both in situ and ex situ approaches [56; 74; 75; 76]. However, the mechanism behind SEI formation is relatively unclear even though there are two major models proposed so far; Peled's model and Besenhard's model [56].

Peled's model proposed SEI as a two-dimensional passivation film established via a surface reaction [77]. Originally Peled suggested the 2D film model for a lithium metal surface and Dahn applied this model to carbonaceous electrodes [56]. Adoption to graphitic material is not simple because the chemical properties of SEIs were different despite the fact that fully lithiated graphite and lithium metal have similar potentials. With graphitic material, the formation process of SEI does not start until the potential of an anode is cathodically polarized to a certain level. This is because the intrinsic potential of carbonaceous materials are much higher than the reduction potential for most solvents and salts [56]. On the other hand, with a lithium metal, SEI forms instantly upon contact with electrolytes. Endo et al. investigated the decomposition of an electrolyte (i.e., SEI formation) on a graphite anode by electron spin resonance [56; 78]. They found that SEI formed on carbonaceous anodes primarily consisted of the decomposition products of decomposed solvents, such as EC, in the solvation sheath of lithium ion, which migrates toward the negatively charged anode surface [56]. In addition, they also mentioned that the reduction of cyclic carbonates such as EC would become major composition of SEI, while the linear carbonates in the mixture are relatively inconsequential [56]. Wang et al. observed similar phenomena through a numerical investigation with density functional theory. Even though the reduction of a free EC molecule is very unlikely, the coordination of a lithium ion to an EC molecule renders one- or two-electron reduction processes thermodynamically possible in a supermolecular structure [56; 73]. With all of these efforts, the 2D film model is confirmed even for carboneous material to clarify the difference against lithium metal.

Peled's model also established a theoretical basis for electrolyte additives. Peled et al. proposed to use a data bank of the rate constant (k_e) of reduction in aqueous media to find ideal electrolytes based on a fair correlation between this constant and SEI formation potential. SEI formation potential plays an important role because SEI must be completed far before the cointercalation of a solvent occurs. This model shows that ideal electrolytes must have $k_e < 10^9$ [1/s] that corresponds to AsF_6^-, EC, vinylene carbonate and CO_2 [77].

Besenhard's model is based on another difference between lithium metal and carbonaceous material different from the selective reduction shown in Peled's model, where the presence of interlayer voids of graphite can accommodate both lithium ions and solvent molecules [56]. This model suggests that the reductive reaction of an electrolyte in contact with graphite might not be a simple surface reaction as proposed in Peled's model, but a more complex reaction where a solvent can cointercalate into graphene layers before it decomposes [56]. Therefore, the passivation film can penetrate the structure of graphite and form a ternary graphite intercalation compound (GIC) [56; 79]. However, this model is not proven at a microscopic level. All of the in situ X-ray diffraction (XRD) measurements conducted by other researchers could not show proof of a substantial change in the interlayer distance around the cointercalation potential [56; 76; 80]. Furthermore, the thermodynamic stability of the ternary GICs is also questionable. The intercalation of a bare lithium ion into two giant graphene ions is obviously more favorable compared to the intercalation of solvated molecular dipoles by solvent species [56; 81].

In this study, the secondary reaction, claimed by Aurbach et al. (Equation 2.4), based on Peled's model is formulated in the battery simulation.

2.6.2 SEI decomposition at elevated temperatures

The SEI prevents irreversible reactions of electrolytes on electrode surfaces that are otherwise thermodynamically favorable [56]. At room temperature, this layer, formed in EC-based electrolyte, is stable and has negligible reactivity. However, under high temperatures or during long-term storage, their stability is still doubtful.

The stability of carbonaceous anodes in electrolytes was studied utilizing DSC by Tarascon and co-workers [82]. During this study they found that there was a thermal transition at 120 °C prior to the reaction between lithiated carbon and fluorinated polymers on the anode (Figure 2.18). In fact, it is know that the onset temperature of SEI decomposition highly depends on the type of salt and electrolyte [66]. For 1 M $LiPF_6$ in EC and DEC, the onset temperature was reported as 105 °C, whereas, with $LiBF_4$, it is as low as 60 °C [83; 84]. This SEI decomposition process was described to form Li_2CO_3 based on previous understandings of SEI chemical composition and the thermal stability of lithium alkyl carbonates [56; 85; 86; 87]. They concluded the transition is due to SEI decomposition by comparing anodes with and without rinsing in DMC. When SEI was washed away from DMC rinsing, the transition at 120 °C did not appear. Instead, large spikes of heat flow were observed at 300 °C with an anode that is not protected by SEI layers (Figure 2.18). The influence from damaged SEI is harmful for cell performance not only in terms of heat release but also for the impedance of the electrode/electrolyte interface. The damaged

SEI has to be repaired constantly by the same electrochemical reactions that occurred in the initial formation process, which consumes the limited lithium ion source in the cell and increases impedance.
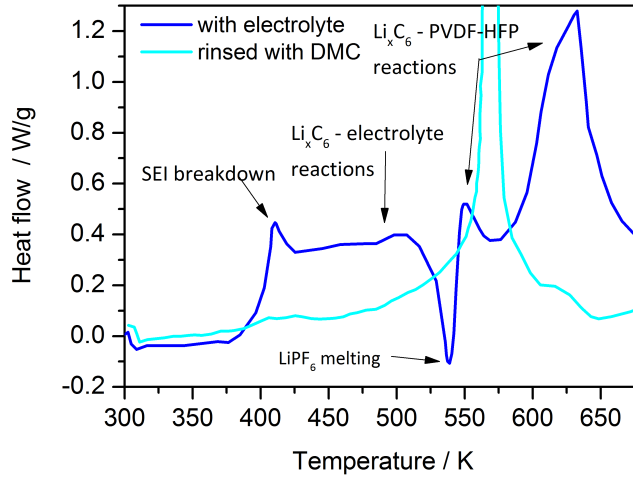

Figure 2.18: DSC trace of the reactions in a fully lithiated MCMB25-28 graphite anode with electrolyte based on ref. [82].

Tarascon and co-workers suggested that the SEI on a carbonaceous anode could be subject not only to simple dissolution, but also to decomposition at elevated temperatures turning into Li_2CO_3 [56; 82]. Dahn and co-workers supported their hypothesis and proposed the thermal decomposition of the SEI via the transformation of metastable alkyl carbonate, $(CH_2OCO_2Li)_2$, into stable lithium carbonate, Li_2CO_3, (Equation 2.5) [83; 84; 88; 89]. They performed accelerating rate calorimetry (ARC) on anode samples to study the reaction between lithium-containing carbon and a nonaqueous electrolyte.

$$(CH_2OCO_2Li)_2 \rightarrow Li_2CO_3 + C_2H_4 + CO_2 + \frac{1}{2}O_2 \qquad (2.5)$$
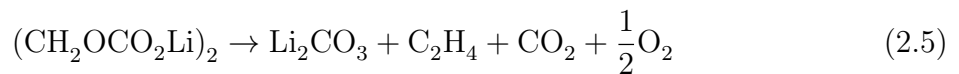
Amine and co-workers also proved their suggestion by studying the change of surface chemistry on well-cycled carbonaceous anodes stored under elevated temperature [56; 90]. They conducted XPS and observed significant amount of Li_2CO_3 on graphite surface after storage at 70 °C for prolonged durations [56]. Their results also show decreasing ether/alkoxide signals, in addition to elemental carbon, which is also evidence for the hypothesis of Dahn and co-workers.

In this work, the SEI decomposition is assumed to proceed as described in Equation 2.5, in the battery simulation.

2.7 Other components: separator and current collectors

There are two battery components directly attached to electrodes: separator and current collectors.

Lithium ion cells use microporous films to electrically insulate the positive and negative electrodes [15]. The thickness is usually within 10 to 30 μm. All current commercialized lithium ion cells that contain liquid electrolyte utilize microporous polyolefin materials because of their excellent mechanical properties, chemical stability and reasonable cost [15]. In general, the microporous polyolefin material is made of Polyethylene (PE), Polypropylene (PPE) or laminates of polyethylene and polypropylene. The low melting point of polyethylene also acts as a thermal fuse to avoid an internal short circuit [91]. Loss of porosity and the shutdown of the separator can be observed when temperatures approach the melting point of polymer (135 °C for polyethylene and 165 °C for polypropylene) [15; 91]. To accommodate the advantages of distinct materials, tri-layer materials of PPE/PE/PPE have been developed. PPE is used to keep the quality of the film and PE with a low melting point is used to shutdown the cell if it reaches to an over-temperature condition [15].

The most commonly used anode and cathode current collectors are copper and aluminum, respectively. Copper is widely used on the anode side because it is stable at a low potential and offers excellent conductivity [92]. The lack of a passivation layer against a non-aqueous electrolyte on the metal surface makes it possible for copper ions (Cu^+ or Cu^{2+}) to be readily dissolved from a bare metal surface. There are three reasons why aluminum is the most common material used for the current collector of a cathode: (1) aluminum foil is not doped with the lithium ion in a potential range used as the collector, (2) aluminum has high resistivity against corrosion, and (3) aluminum is electronically conductive [15; 93]. In our simulation, the target cells are assumed to have these types of current collectors.

2.8 Continuum modeling and simulation of lithium-ion batteries

2.8.1 Overview

Most theory used in continuum modeling of lithium ion batteries was first developed for other battery/electrochemical systems such as lead acid, alkaline zinc-MnO_2, molten

salt LiAl-FeS, and nickel-metal hydride [94]. As an early theoretical work, Newman and Tiedemann presented general governing equations for porous electrodes [95; 96]. Newman also presented similar equations for applications to electrochemical systems in general [97]. Based on the governing equations shown by Newman and co-workers, Wang et al. developed a micro-macroscopic coupled model for batteries and fuel cells utilizing the volume-averaging technique, that includes solid-state physics of electrode active materials and interface morphology and chemistry [96; 98]. General energy balance for battery systems was also introduced by Newman and co-workers [96; 99]. Later, the energy balance was extended for insertion battery systems in the same group [96; 100]. Botte et al. accommodated the effect of side reactions in the thermal behavior of a cell extending the theory by energy balance [96; 101].

Electrochemical models for secondary lithium batteries have been developed utilizing simplified equations for different limiting cases [96; 102]. The simplest model is the Single-Particle Model (SPM) that incorporates the effects of transport phenomena in a simple manner [103; 104]. In the SPM, diffusion and intercalation are modeled in a single particle, which represents the entire thickness of the electrode [102; 103]. It considers that each electrode has the single particle with the same surface area as the electrode. This model neglects the concentration and potential effects in the solution phase between the particles [103; 105]. Anode and cathode reactions presented in Equation 2.1 are took into account in the anode and cathode particles. Because of simplifications, computational time of this model is very short but is only valid for limited conditions, such as low rates and thin electrodes [103; 105]. A parabolic profile approximation for the lithium concentration within the particle provides greater efficiency in computational time [106].

A slightly more complex model is the ohmic porous-electrode model [103]. This model considers solid- and electrolyte- phase potentials and currents, however it neglects the spatial variation of the concentrations [103]. This model assumes either linear, Tafel, or exponential kinetic electrochemical reactions [103] and can also be incorporated with additional phenomena such as porosity dependent conductivities. It is also utilized for optimizing the thickness of a separator/electrodes and spatial variations of porosity within electrodes [103; 107; 108; 109; 110].

The Pseudo-two-Dimensional (P2D) model extends the ohmic porous-electrode model by including diffusion in the electrolyte and solid phases with Butler-Volmer kinetics [103]. Newman and co-workers developed a P2D model with a concentrated solution theory for electrolyte diffusion [111]. This model describes the internal behavior of lithium ion batteries while accounting for the combination of anode and cathode electrodes, a separator and the current collector within the cell (Figure 2.19).
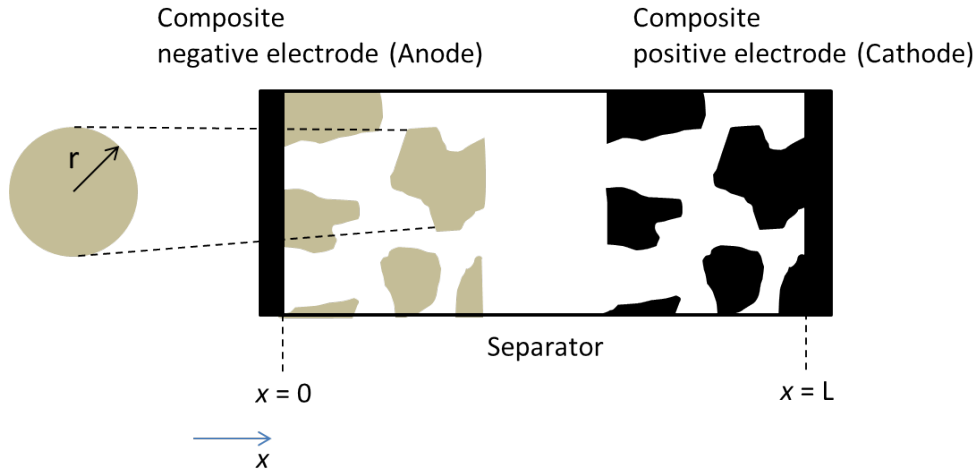
Figure 2.19: Schematic of sandwich of electrodes and separator in P2D model based on ref. [103].

This P2D model was generic enough to improve understanding of the battery system and inspired the development of similar models [95; 96; 102; 112; 113; 114; 115; 116; 117; 118; 119; 120]. This physics-based model is the most commonly used by researchers and is utilized to solve for the electrolyte concentration/potential, solid-state potential, and solid-state concentration within the porous electrodes [103]. Based on the principles of transport phenomena, electrochemistry, and thermodynamics, this simulation can solve governing equations (partial differential equations) within seconds to minutes [103].

The most complicated continuum model for a battery is three-dimensional (3D) model [121]. A 3D model requires more computational time, however, it can investigate 3D local distributions of micro-variables such as ionic concentration and potential through distinct phases of battery components (i.e., solid and liquid phases). In comparison, 1D and 2D models only focus on the macro-scale distribution of state variables [121].

In this study, we utilize a battery model based on the pseudo-two-dimensional model in order to take advantage of shorter computational times.

The basis of continuum model for porous electrodes was introduced by Newman and Tiedemann as described previously in Section [95]. In porous electrode theory, the exact positions and shapes of particles and pores in the electrodes are not specified [94]. Properties are averaged over a small volume which is large compared to pore structure. The electrodes are viewed as a superposition of active material, binder, and electrolyte, and these phases coexist at every point in the model [94]. The particles of active material are generally modeled as spheres. Phases between electrodes and electrolyte are coupled with each other via mass balances and reaction rates depend on potential differences between phases [94]. Electroneutrality is assumed on all phases considering that the thickness of

a double layer is small enough compared to pore volume [94]. The governing equations that describe the electrochemical performance of cell with porous electrodes are reviewed by Thomas and Newman [94]. In general, these governing equations need to be numerically solved because using Butler-Volmer kinetics makes the governing equations nonlinear [94].

Detailed equations and methods used in this work are explained in Section 3.2.

2.8.2 Thermal simulations of lithium ion batteries

Thermal calculations in battery simulations are computationally expensive. There is much research that decouples thermal equations from the electrochemical equations by using a global energy balance [103]. One drawback of the decoupled model is that it makes it impossible to trace the influence on the performance of cells by temperature. However, there are thermal models reported to couple with electrochemical models for both single cells and cell stacks. [99; 103; 122; 123]. The global energy balance is only valid when the distribution of the reaction is homogeneous within a whole cell. However, it is necessary to include the local variations of a reaction current and the state of charge (SOC) to accurately estimate heat generation in a cell [100; 103]. There are studies which incorporate local heat generation. Guo et al. presented a simplified thermal model applied to a single particle [103; 124]. Other researchers showed that 2D thermal-electrochemical models coupled with local heat generation predicted discharge performance at different operating temperatures [103; 125; 126]. Recently, 3D thermal models have been reported to better understand the dynamic operation and control of cells [103]. Because of its heavy computational burden, the 3D models are required to make approximations which result in some drawbacks. For example, some models cannot monitor the thermal effect of electrochemical parameters and other models require empirical inputs from experiments [103; 127; 128]. So far no work has been shown regarding thermal simulation with additional thermal effects other than the electrochemistry of normal cell operations [96].

In this study, we tackled the issue of the additional thermal effects in order to deal with runaway chemistry of lithium ion batteries.

3 Modeling and simulation methodology

3.1 Overview of modeling methodology

3.1.1 Multi-scale continuum model

As reviewed in Chapter 2, the mechanisms behind a lithium ion battery range over several scales, from atomistic to full-cell scale. As briefly mentioned in Section 2.8, battery models must be incorporated with a multi-scale model to reproduce simultaneous phenomena that occur inside of a battery. Similar to other studies of the P2D model, the software utilized in this work can distinguish four scales from particle to single cell scales as shown in Figure 3.1. In this work, as the target temperature is elevated, actual calculations are conducted among two scales: electrode sandwich and a cell scales. On the particle scale, the intercalation and extraction of lithium ions are generally modeled on lithium diffusion in solid bulk material that becomes particularly dominant at lower temperatures. Thus, we made an assumption that the diffusion into solid bulk is sufficiently fast.

Model and simulation based on the atomistic scale are not conducted in this study because the models in this work are based on continuum theory. Additionally, battery pack models are also not included because this work focuses on the electrochemistry within a cell instead of system modeling. To reduce computational costs, all of the scales are individually modeled in one dimension (1D). A detailed explanation of the computational spatial discretization of cell components is provided in Section 3.5. Mass and charge transport within a liquid electrolyte is modeled off of electrochemical processes within an electrode sandwich. Modeling of mass and charge transport is reviewed in Section 3.3. The electrode sandwiches are aligned side by side from the center to the surface of a cell in order to model the radial configuration of a wounded cylindrical cell in 1D (Figure 3.2).

On the scale of radial configuration, heat transfer through a cell is calculated in the model. As discussed in Section 2.8.2, thermal calculation is computationally expensive. In order to deal with this problem, a model reduction method is applied for thermal calculation.
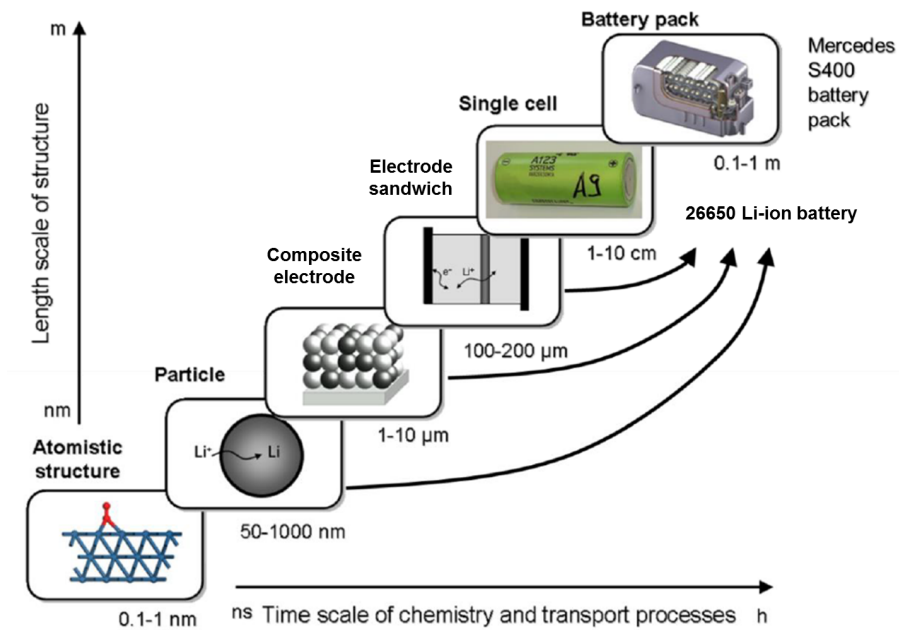
Figure 3.1: Time and length scales of processes in batteries [129]. The picture of battery pack is from ref. [130].
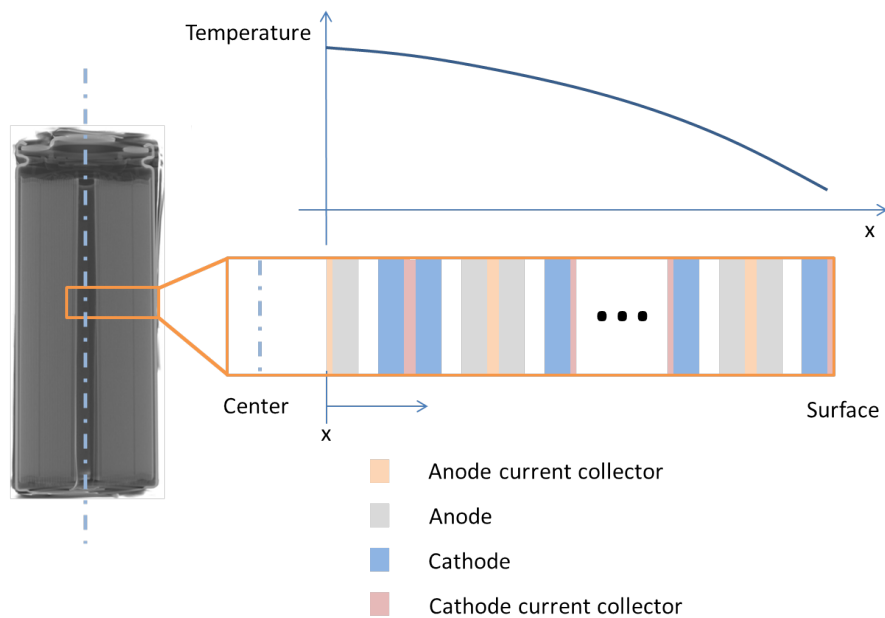

Figure 3.2: Schematic of aligned electrode sandwich model and an example temperature distribution in the radial direction when ambient temperature is lower than inner temperature of a cell.

Details of the heat transfer model and the reduction technique are explained in Section 3.4. The models in this study are simulated using a coupled software of in-house developed code, Detailed Electrochemistry and Numerical Impedance Simulation (DENIS), and an open source software developed at the California Institute of Technology, Cantera [131]. More information on this software is provided in Section 3.6.

3.1.2 Governing equations

The governing equations used in our battery simulation are shown in Table 3.1. The equations summarized in this work are based on three main theories behind battery simulations and will be explained in the following sections. These theories are the electrochemistry (i.e., thermodynamics and kinetics) of electrodes (Section 3.2), mass and charge transfer in liquid electrolyte (Section 3.3), and heat transfer through a cell (Section 3.4).

The section on the electrochemistry of electrodes (Section 3.2) reviews (1) how equilibrium potentials of electrodes relate to thermodynamic properties (ΔG, ΔH and ΔS), (2) how the kinetics of electrode reactions are represented by the Butler-Volmer equation, and (3) how thermodynamic properties of pure and blended electrode materials are obtained through experimental results.

As a condition of liquid electrolyte, dilute solution theory is applied to make it easier for simulations to deal with a wide range of elevated temperatures. Section 3.3 reviews mass and charge conservation law based on the dilute solution theory.

Section 3.4 reviews energy conservation and the details of heat source terms.

Section 3.5 introduces computational spatial discretizations and the general parameters utilized in simulations, such as the dimensions and properties of electrodes and the kinetic parameters of reactions.

Table 3.1: Governing equations of lithium ion battery model based on ref. [129].

Physicochemical process	Model equation

Thermodynamics (Section 3.2)

Half-cell equilibrium potential $\quad \Delta\phi_{\mathrm{eq}}\left(c_{\mathrm{Li}}\right) = -\dfrac{\Delta G\left(c_{\mathrm{Li}}\right)}{zF} = -\dfrac{\Delta H\left(c_{\mathrm{Li}}\right) - T\Delta S\left(c_{\mathrm{Li}}\right)}{zF}$

Kinetics (Section 3.2)

Butler-Volmer Kinetics $\qquad i_{\mathrm{F}}^{\mathrm{V}} = i_0 \left\{ \exp\left(\dfrac{\alpha_{\mathrm{a}}F}{RT}\eta_{\mathrm{act}}\right) - \exp\left(-\dfrac{\alpha_{\mathrm{c}}F}{RT}\eta_{\mathrm{act}}\right) \right\}$

Exchange current density $\qquad i_0 = i_{00}{\cdot}c_{\mathrm{Li,el}}^{a}{\cdot}X_{\mathrm{Li,bulk}}^{b}{\cdot}(1 - X_{\mathrm{Li,bulk}})^{c}{\cdot}\exp\left(-\dfrac{E_{\mathrm{act}}}{RT}\right)$

Activation overpotential $\qquad \eta_{\mathrm{act}} = \Delta\phi - \Delta\phi_{\mathrm{eq}}\left(c_{\mathrm{Li}}\right) - \eta_{\mathrm{conc}}$

Potential step $\qquad \Delta\phi = \phi_{\mathrm{elde}} - \phi_{\mathrm{elyt}}$

Total current density $\qquad i = \displaystyle\int_{y=0}^{L_{\mathrm{elde}}} \left(i_{\mathrm{F}}^{\mathrm{V}} + i_{\mathrm{dl}}^{\mathrm{V}}\right) \mathrm{d}y$

Current density of electrochemical double-layer $\qquad i_{\mathrm{dl}}^{\mathrm{V}}\left(t\right) = A_{\mathrm{dl}}^{\mathrm{V}}\left(\Delta\phi\right)\dfrac{\partial(\Delta\phi)}{\partial t}$

Cell voltage $\qquad E(i) = \phi_{\mathrm{ca}}(i) - \phi_{\mathrm{an}}(i) = E_{\mathrm{eq}} - \eta(i)$

Transport in liquid electrolyte (dilute solution theory) (Section 3.3)

Mass conservation $\qquad \dfrac{\partial(\epsilon\rho_i)}{\partial t} = \nabla\left(D_i\nabla\rho_i\right) + \nabla\left(D_i^{\mathrm{migr}}\nabla\phi\right) + M_i\dot{s}_i^{V}$

Charge conservation $\qquad \nabla(\sigma\nabla\phi) = b$

Table 3.1: Governing equations of lithium ion battery model (continued)

Physicochemical process	Model equation

$$\sigma = \sum_i \left(\frac{z_i^2 F^2}{RT} \frac{D_i \rho_i}{M_i} \right)$$

$$b = -\sum_i \left\{ \nabla \left(\frac{z_i D_i F}{M_i} \nabla \rho_i \right) \right\} - \sum_i z_i F \dot{s}_i^{\mathrm{V}}$$

Heat transfer (Section 3.4)

Energy conservation

$$\rho_{\mathrm{eff}} c_{\mathrm{p}}^{\mathrm{eff}} \frac{\partial T}{\partial t} = \nabla \left(\lambda^{\mathrm{eff}} \nabla T \right) + \sum_j \dot{q}_j^{\mathrm{V}}$$

Reversible heat

$$\dot{q}_{\mathrm{rev}}^{\mathrm{V}} = \frac{i^{\mathrm{V}}}{zF} \left\{ \sum_e \left(-T \Delta_R S_e^{\mathrm{m}} \right) \right\}$$

Ohmic/Reversible/Polarization heat

$$\dot{q}_j^{\mathrm{V}} = i^{\mathrm{V}} \left\{ \sum_l \left(\eta_j \right) \right\}$$

Electrochemical heat

$$\dot{q}_{\mathrm{chem}}^{\mathrm{V}} = \dot{q}_{\mathrm{rev}}^{\mathrm{V}} + \dot{q}_{\mathrm{pol}}^{\mathrm{V}} = i^{\mathrm{V}} \left(\frac{\Delta H}{zF} + \Delta \phi \right)$$

Heat by runaway chemistry (with charge transfer reaction)

$$\dot{q}_{\mathrm{run,char}}^{\mathrm{V}} = \sum_n r_n \left(\Delta H_n + zF \Delta \phi \right)$$

Heat by runaway chemistry (without charge transfer reaction)

$$\dot{q}_{\mathrm{run,non\text{-}char}}^{\mathrm{V}} = \sum_n r_n \Delta H_n$$

3.2 Electrochemistry

3.2.1 Potentials and thermodynamics of batteries

The key concept of electrode potentials is reversibility which is used to treat processes thermodynamically. This is because the process on electrodes involves a phenomena that can move electrodes in two opposite directions from the equilibrium position [132]. In electrochemistry, we generally need to distinguish three types of reversibility: chemical reversibility, thermodynamic reversibility and practical reversibility.

Upon chemically reversible reactions, new reactions do not appear reversing the reaction (i.e., reactants of the forward reaction can be products of the backward reaction and vice versa) [132]. For example, the overall cell reaction shown in Equation 2.1 is the chemically reversible process. A process is thermodynamically reversible when the process can be reversed by means of infinitesimal changes in a property of the system without any energy dissipation (i.e., no increase of entropy) [133]. A cell that is chemically irreversible cannot behave reversibly in a thermodynamic sense [132]. A chemically reversible cell may operate in both in a manner approaching thermodynamic reversibility and irreversibility. In fact, as actual processes always happen in a finite length of time, they cannot proceed with strict thermodynamic reversibility [132]. However, there is a case where a process can in practice proceed in a way that thermodynamic equation can be applied with a certain degree of accuracy. This type of condition is called practically reversibility.

The processes on electrodes are assumed to be practically reversible. In this case, we rely on the Nernst equation (Equation 3.1) to express electrode potential as a function of the concentration of participants in the electrode process [132].

$$E = E_{\mathrm{eq}} + \frac{RT}{zF} \ln \frac{c_{\mathrm{O}}}{c_{\mathrm{R}}},$$

(3.1)

where O and R are the participants in the electrode process of:

$$\mathrm{O} + ze^- \leftrightarrow \mathrm{R}.$$

(3.2)

Because the process on electrodes are thermodynamically reversible, Gibbs free energy can be referenced for the maximum net work. (Equation 3.3) [132].

$$\begin{aligned}
\Delta G &= \text{charge passed} \times \text{reversible potential difference} \\
&= -zF\Delta\phi_{\mathrm{eq}}.
\end{aligned}$$

(3.3)

where F is Faraday's constant and we consider E to be positive when a cell reaction is spontaneous. This is justified by the fact that net work done when the infinitesimal charge traveling from the anode to the cathode is equal to the product of the charge and the potential difference, E.

Substitute $\Delta G = \Delta H$ - $T \Delta S$ to Equation 3.3,

$$\Delta\phi_{\text{eq}} = -\frac{\Delta G}{zF} \quad = -\frac{\Delta H - T\Delta S}{zF}. \tag{3.4}$$

Equation 3.4 provides a relationship between equilibrium potential and thermodynamic properties that is also utilized in thermal calculations. The thermodynamic properties used in this work are reviewed in Sections 3.5.3 and 3.5.4.

3.2.2 Kinetics of electrode reactions

To quantitatively rationalize electrode kinetics, we first review homogeneous kinetics in dynamic equilibrium [132]. Consider the simple unimolecular elementary reactions as shown in Equation 3.5.

$$A \underset{k_{\text{b}}}{\overset{k_{\text{f}}}{\rightleftharpoons}} B, \tag{3.5}$$

where rates of forward and reverse processes (v_{f} and v_{b}) are

$$v_{\text{f}} = k_{\text{f}}c_{\text{A}}, \tag{3.6}$$

$$v_{\text{b}} = k_{\text{b}}c_{\text{B}}. \tag{3.7}$$

k_{f} (forward) and k_{b} (reverse) are rate constants of reactions with dimensions of s^{-1}. c is the concentration of a participant. The net conversion rate of A to B can be described as:

$$v_{\text{net}} = k_{\text{f}}C_{\text{A}} - k_{\text{b}}C_{\text{B}}. \tag{3.8}$$

This argument can also apply to electrode kinetics (Equation 3.2), as the equilibrium is characterized by the Nernst equation. In this case, the electrode current can be related to the rates of processes.

$$v_{\mathrm{f}} = k_{\mathrm{f}} c_{\mathrm{O}} = \frac{i_{\mathrm{c}}}{zFA}, \tag{3.9}$$

$$v_{\mathrm{b}} = k_{\mathrm{b}} c_{\mathrm{R}} = \frac{i_{\mathrm{a}}}{zFA}, \tag{3.10}$$

where i_{c} is a cathodic current the because forward reaction in the electrode kinetic is a reduction. Likewise, the reverse reaction has an anodic current i_{a}. A is a specific area.

Thus, net reaction rate is

$$v_{\mathrm{net}} = k_{\mathrm{f}} c_{\mathrm{O}} - k_{\mathrm{b}} c_{\mathrm{R}} = \frac{i}{nFA}. \tag{3.11}$$

The overall total current is

$$i = i_{\mathrm{c}} - i_{\mathrm{a}} = zFA \left(k_{\mathrm{f}} c_{\mathrm{O}} - k_{\mathrm{b}} c_{\mathrm{R}} \right). \tag{3.12}$$

The rate constant k is known to vary with temperature in a certain manner by experimental fact: $\ln k$ is proportional to $1/T$ (Equation 3.13) [132].

$$k = f \exp \left(-\frac{E_{\mathrm{act}}}{RT} \right). \tag{3.13}$$

Arrhenius first recognized the generality of this behavior, thus, this equation is often called an Arrhenius equation. E_{act} is known as the activation energy with units of energy because the exponential factor is similar to the probability of using thermal energy to surmount an energy barrier of height E_{act} [132]. f is called a frequency factor for expressing the frequency of attempts to surmount the barrier [132].

When considering the reaction path in terms of potential energy along a reaction coordinate, the activation energy is often identified as the height of the maximum above a valley. In another notation, we can regard E_{act} as a change in standard internal energy while overcoming a transition state [132]. In this case, E_{act} can be also expressed as $\Delta E^{\ddagger}$, the standard internal energy of activation. Similarly, the standard enthalpy of activation, $\Delta H^{\ddagger}$, is $\Delta E^{\ddagger} + \Delta(PV)^{\ddagger}$ where $\Delta(PV)^{\ddagger}$ is actually neglected under a condensed-phase reaction so that $\Delta H^{\ddagger} \approx \Delta E^{\ddagger}$. Thus, the Arrhenius equation can be expressed with $\Delta H^{\ddagger}$:

$$k = f \exp \left(-\frac{\Delta H^{\ddagger}}{RT} \right). \tag{3.14}$$

Since $\Delta S^{\ddagger}/R$ is a dimensionless constant, the frequency factor A can be also expressed as $f' \exp\left(\Delta S^{\ddagger}/R\right)$. If we substitute this with an Arrhenius equation (Equation 3.13):

$$k = f' \exp\left(-\frac{\Delta H^{\ddagger} - T\Delta S^{\ddagger}}{RT}\right), \tag{3.15}$$

$$= f' \exp\left(-\frac{\Delta G^{\ddagger}}{RT}\right), \tag{3.16}$$

where $\Delta G^{\ddagger}$ is the standard free energy of activation. Equation 3.16 is also an empirical generalization of reality, like Equation 3.13 and these expressions do not depend on a specific theory of kinetics [132].

Let us consider a one-step, one-electron process as our target electrode kinetics of lithium-ion batteries only involves one electron as shown in 2.1. z in Equation 3.2 is unity in this case (Equation 3.17).

$$\text{O} + e \underset{k_{\text{b}}}{\overset{k_{\text{f}}}{\rightleftharpoons}} \text{R}. \tag{3.17}$$

To develop a theory of electrode kinetics, the standard free energy of activation, $\Delta G^{\ddagger}$, is expressed as a function of electrode potential utilizing Equation 3.3 [132]. In general, electrode potentials are considered to be reference potentials.

If the potential of an electrode process is changed by ΔE to a new value E'', then the relative energy of the electron resident on the electrode changes by $-F\Delta E'' = -F(E'' - E')$, where former electrode potential is defined as E' (Figure 3.3). Likewise, the standard free energy is also affected by the potential change. Looking at the barrier for oxidation, $\Delta G_{\text{a}}''^{\ddagger}$, it becomes less than $\Delta G_{\text{a}}'^{\ddagger}$ by a fraction of the total energy change. The fraction, $1 - \alpha$, is called a transfer coefficient and can vary from zero to unity [132].

Thus, we can formulate the anodic and cathodic free energy of activation, $\Delta G_{\text{a}}^{\ddagger}$ and $\Delta G_{\text{c}}^{\ddagger}$, with the transfer coefficient:

$$\Delta G_{\text{a}}''^{\ddagger} = \Delta G_{\text{a}}'^{\ddagger} - (1 - \alpha)F(E'' - E'), \tag{3.18}$$

$$\Delta G_{\text{c}}''^{\ddagger} = \Delta G_{\text{c}}'^{\ddagger} - \alpha F(E'' - E'). \tag{3.19}$$

Assuming the rate constants follow the Arrhenius equation shown in Equation 3.16, the rate constants of forward and reverse reactions are:
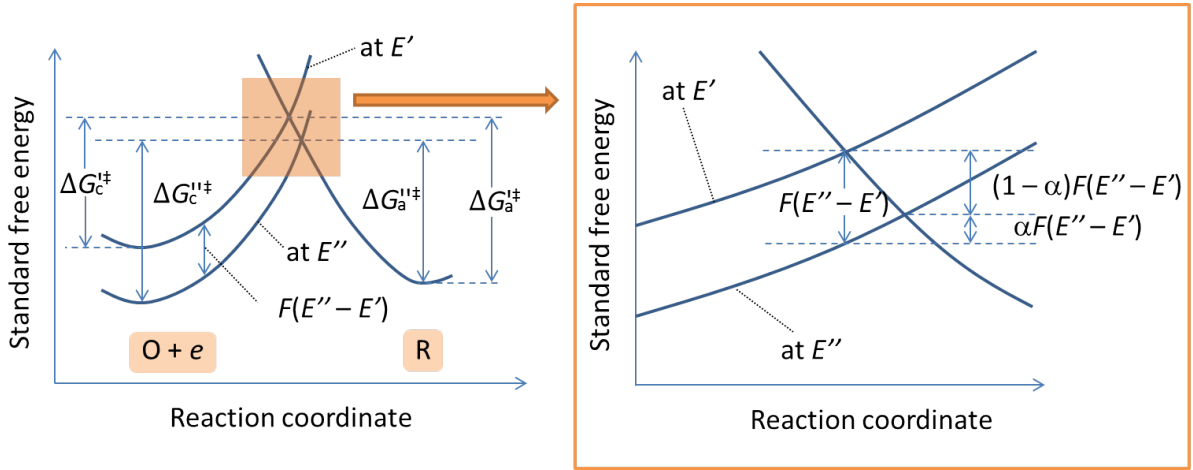
Figure 3.3: Effects of a potential change on the standard free energies of activation for oxidation and reduction based on ref. [132].

$$k_{\mathrm{f}} = f_{\mathrm{f}} \exp\left(-\frac{\Delta G_{\mathrm{c}}''^{\ddagger}}{RT}\right), \tag{3.20}$$

$$k_{\mathrm{b}} = f_{\mathrm{b}} \exp\left(-\frac{\Delta G_{\mathrm{a}}''^{\ddagger}}{RT}\right). \tag{3.21}$$

Substituting the free energy of activation (Equation 3.18 and 3.19) gives:

$$k_{\mathrm{f}} = f_{\mathrm{f}} \exp\left(-\frac{\Delta G_{\mathrm{c}}'^{\ddagger}}{RT}\right) \exp\left\{-\alpha\frac{F(E''-E')}{RT}\right\}, \tag{3.22}$$

$$k_{\mathrm{b}} = f_{\mathrm{b}} \exp\left(-\frac{\Delta G_{\mathrm{a}}'^{\ddagger}}{RT}\right) \exp\left\{(1-\alpha)\frac{F(E''-E')}{RT}\right\}. \tag{3.23}$$

In the special case of $c_{\mathrm{O}} = c_{\mathrm{R}}$, $E'' = E'$ from the Nernst equation and $k_{\mathrm{f}}c_{\mathrm{O}}^* = k_{\mathrm{b}}c_{\mathrm{R}}^*$ in equilibrium where c^* is bulk concentration, thus $k_{\mathrm{f}} = k_{\mathrm{b}}$ [132]. This means that E' is the potential when forward and reverse reaction rates are identical, and k' is the standard rate constant [132]. Using the standard rate constant, Equations 3.22 and 3.23 can be simplified as:

$$k_{\mathrm{f}} = k' \exp\left\{-\alpha\frac{F(E''-E')}{RT}\right\}, \tag{3.24}$$

$$k_{\mathrm{b}} = k' \exp\left\{(1-\alpha)\frac{F(E''-E')}{RT}\right\}. \tag{3.25}$$

Substituting these into Equation 3.12 yields:

$$i = FAk' \left[c_O \exp\left\{ -\alpha \frac{F(E'' - E')}{RT} \right\} - c_R \exp\left\{ (1 - \alpha)\frac{F(E'' - E')}{RT} \right\} \right]. \quad (3.26)$$

This current-potential relation is the basis of almost any equation of charge-transfer kinetics. There are several expressions derived from this relation and these are widely known as Butler-Volmer formulation, named after the pioneers of this field [132].

One commonly used equation in battery simulation is the Butler-Volmer formulation with an exchange current under the assumption of a no-mass transfer effect which is also used in this work.

The exchange current, i_0, is introduced in order to utilize equilibrium potential in the Butler-Volmer equation and is defined in equilibrium when the net current, i, is zero to form Equation 3.26 [132]:

$$i_0 = FAk^0 c_O^* \exp\left\{ -\alpha \frac{F(E_{eq} - E')}{RT} \right\} = FAk^0 C_R^* \exp\left\{ (1 - \alpha)\frac{F(E_{eq} - E')}{RT} \right\}. \quad (3.27)$$

Substituting the exchange current (Equation 3.27) into the Butler-Volmer formulation of Equation 3.26 provides:

$$i = i_0 \left[\frac{c_O}{c_O^*} \exp\left\{ -\alpha \frac{F\eta}{RT} \right\} - \frac{c_R}{c_R^*} \exp\left\{ (1 - \alpha)\frac{F\eta}{RT} \right\} \right], \quad (3.28)$$

where $\eta = E'' - E_{eq}$ is known as overpotential. If the current is kept low enough so surface concentration does not differ largely from the bulk value, Equation 3.28 becomes:

$$i = i_0 \left[\exp\left\{ -\alpha \frac{F\eta}{RT} \right\} - \exp\left\{ (1 - \alpha)\frac{F\eta}{RT} \right\} \right]. \quad (3.29)$$

The kinetic parameters used in our simulation are summarized in Section 3.5.2.

3.3 Mass and charge transfer

The Nernst-Planck equation is utilized to model the conservation of mass under the theory of dilute solution [129; 134]. This equation describes the flux of ions under the influences of ion concentrations and electric potential [129]:

$$\frac{\partial(\epsilon\rho_i)}{\partial t} = \nabla(D_i\nabla\rho_i) + \nabla(D_i^{\mathrm{migr}}\nabla\phi) + M_i\dot{s}_i^{\mathrm{V}}. \tag{3.30}$$

On the right-hand side of Equation 3.30, the terms represents diffusion, migration and convection, respectively. Diffusion is a process that results from random motion of molecules by which there is a net flow from a region of high concentration to a region of low concentration, whereas migration is dependent on electric field. Accompanying mass conservation, the equation of charge neutrality is introduced to address a number of unknowns [129].

$$\sum(\epsilon c_i z_i) = 0. \tag{3.31}$$

Substituting Equation 3.31 into the Nernst-Planck equation (3.30) provides the equation for the conservation of charge [134].

$$\nabla\sum_i\left(\frac{z_i^2 F^2}{RT}\frac{D_i\rho_i}{M_i}\right)\nabla\phi = -\sum_i\left\{\nabla\left(\frac{z_i D_i F}{M_i}\nabla\rho_i\right)\right\} - \sum_i\left(z_i F\dot{s}_i^{\mathrm{V}}\right), \tag{3.32}$$

which is a typical form of the conservation of charge equation:

$$\nabla(\sigma\nabla\phi) = b. \tag{3.33}$$

3.4 Heat transfer

3.4.1 Principles of heat transfer in batteries

Thermal energy caused by an exothermic reaction or Joule heating accumulation inside of a cell, is able to dissipate at the cell surface. This is modeled by the conservation of energy equation which results in a temperature gradient inside of a cell [135]. This equation is:

$$\rho^{\mathrm{eff}}c_{\mathrm{p}}^{\mathrm{eff}}\frac{\partial T}{\partial t} = \nabla\left(\lambda^{\mathrm{eff}}\nabla T\right) + \sum_j\dot{q}_j^{\mathrm{V}}. \tag{3.34}$$

The first term on the right-hand side is heat flux by conduction. The second term consists of five types of heat sources: reversible heating, polarization heating, resistive heating, Ohmic heating, and heat by runaway chemistry. The first four types are heat fluxes found in nominal cell operation.

Reversible heat relates to randomness depending on the location of lithium ions within the active material structure during reversible intercalation/extraction processes. Thus utilizing the entropy of lithium intercalation, it is defined as [135]:

$$\dot{q}_{\text{rev}}^{\text{V}} = \frac{i^{\text{V}}}{zF} \sum_e (-T \cdot \Delta_{\text{R}} S_e^{\text{m}}), \tag{3.35}$$

where e is the anode/cathode.

Polarization heating is caused by overpotentials. In this work, two types of overpotentials are considered: activation overpotential η_{act} and concentration overpotential η_{conc}.

$$\dot{q}_{\text{pol}}^{\text{V}} = i^{\text{V}} \sum_e (\eta_{\text{act},e} + \eta_{\text{conc},e}). \tag{3.36}$$

For convenience in this simulation, reversible heat and polarization heat are merged and the combined heat is expressed as electrochemical heat. This electrochemical heat is derived considering reaction enthalpy of intercalation/extraction processes ($\Delta H_{\text{in/ex}}$), assuming constant pressure and work is provided by the ion current (dW/dt) [129; 136].

$$\dot{q}_{\text{rev}}^{\text{V}} + \dot{q}_{\text{pol}}^{\text{V}} = \dot{q}_{\text{chem}}^{\text{V}} = \frac{dW}{dt} + r \cdot \Delta H_{\text{in/ex}} \tag{3.37}$$

$$= i \cdot E + i \cdot \frac{\Delta H}{zF} \tag{3.38}$$

$$= i \left(\frac{\Delta H}{zF} + \Delta \phi_e \right). \tag{3.39}$$

In addition to reversible and polarization heating caused by the intercalation process, heat can be released through several internal resistances of cell components. We refer to the heat caused by resistances of liquid electrolyte and current collectors as resistive heat and ohmic heat, respectively.

$$\dot{q}_{\text{res/ohm}}^{V} = i^{\text{V}} \sum_h (\eta_{\text{res/ohm},h}), \tag{3.40}$$

here, h corresponds to the electrolyte in an anode/separator/cathode for resistive heat and in current collectors for ohmic heat, respectively.

Furthermore, heat released from runaway chemistry is included in the heat sources. The runaway chemistries have both charge transfer and non-charge transfer reactions [137].

As shown in Equation 3.41 charge transfer reaction involves heat through potential effect, in addition to heat expressed with reaction enthalpy.

$$\dot{q}_{\text{run,char},e}^{\text{V}} = \sum_n k_{n,\text{char}} \left(\Delta H_n + zF\Delta\phi_e \right), \tag{3.41}$$

where n shows each reaction and $k_{n,\text{char}}$ is a rate constant of charge-transfer reaction. The rate constant form is identical to Equation 3.22:

$$k_{n,\text{char}} = f \sum_i c_i \exp\left(-\frac{E_{\text{act}}}{RT} \right) \exp\left(\alpha \frac{zF}{RT}\Delta\phi \right). \tag{3.42}$$

Only the rate constant of forward reaction is considered because we model runaway chemistry as global kinetics, which are known as irreversible reactions through experiments. The details of each runaway chemistry reaction are explained in Chapter 4.

On the other hand, non-charge transfer reactions exclude the effect of potentials. The heat from a non-charge transfer reaction is:

$$\dot{q}_{\text{run,non-char}}^{\text{V}} = \sum_n k_{n,\text{non-char}} \Delta H_n, \tag{3.43}$$

where the Arrhenius equation of the first order reaction is assumed for the rate constant of the non-charge transfer reaction, $k_{n,\text{non-char}}$.

$$k_{n,\text{non-char}} = f \sum_i c_i \exp\left(-\frac{E_{\text{act}}}{RT} \right). \tag{3.44}$$

Finally, boundary conditions of the energy conservation equation at the center and the surface of a cell are defined as [129]:

$$\rho^{\text{eff}} c_{\text{P}}^{\text{eff}} \frac{\partial T}{\partial t}\bigg|_{x=center} = 0, \tag{3.45}$$

$$\dot{q}|_{x=surface} = \alpha_{\text{conv}}(T_{\text{surf}} - T_{\text{amb}}) + \epsilon_{\text{surf}}\sigma_{\text{s}}(T_{\text{surf}}^4 - T_{\text{amb}}^4). \tag{3.46}$$

At the center, no heat escapes, whereas heat dissipates at the surface of a cell by thermal convection and thermal radiation. The first term of Equation 3.46 represents convective heat transfer assuming Newton's law of cooling, in which the heat transfer coefficient is

independent of the temperature difference between the object and the environment. The second term corresponds to the radiative heat transfer under the Stefan-Boltzmann law.

The parameters utilized in these simulations are shown in Section 3.5.

3.4.2 Model reduction for temperature calculation

As discussed in Section 2.8.2, a reduced model is utilized for thermal calculations in our battery simulations because the ideal thermal model is computationally expensive. In our simulation, we conducted thermal calculations with a reduced model developed by Hedwig [135]. Figure 3.4 shows a schematic of the model reduction method.
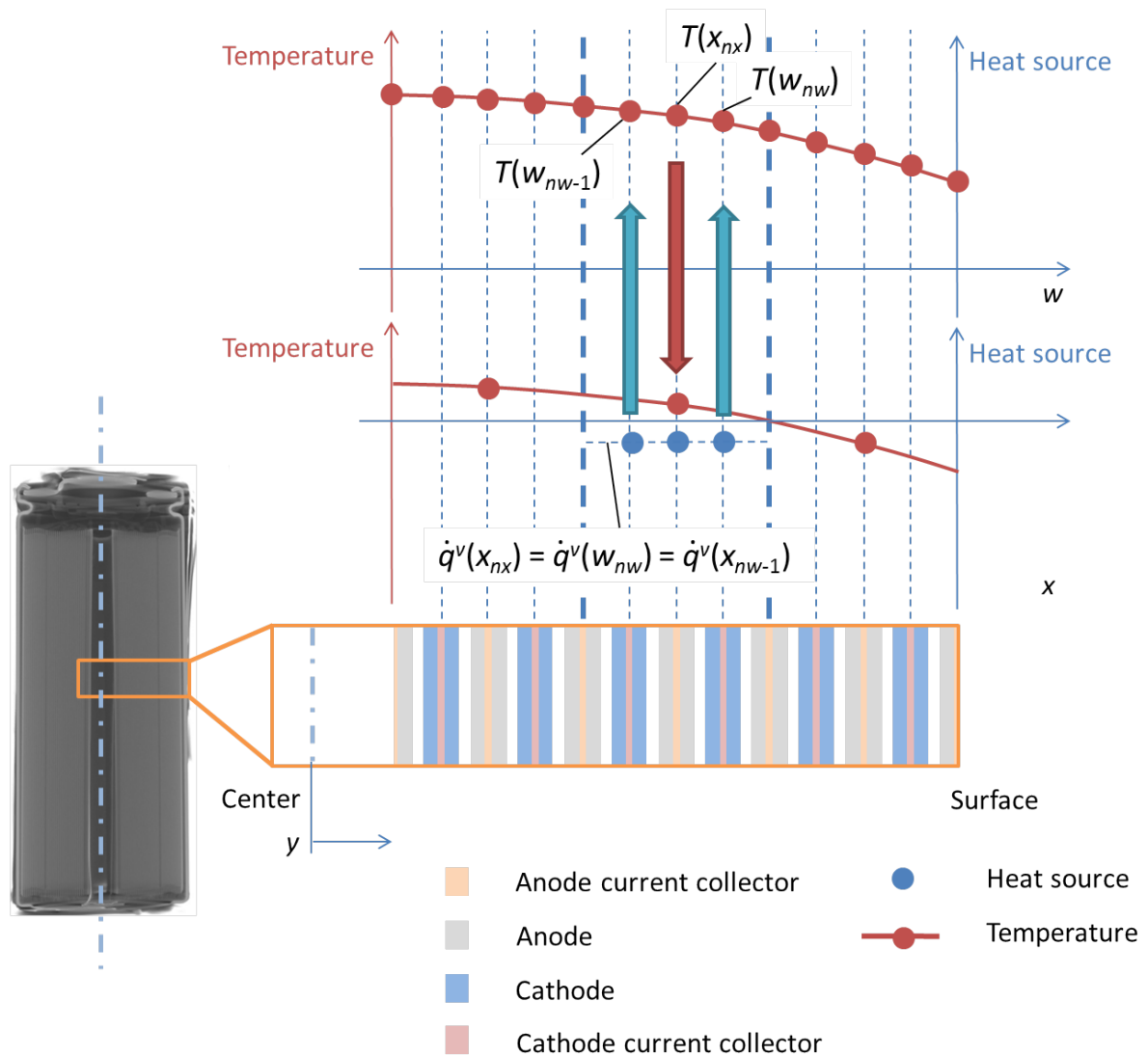
Figure 3.4: Schematics of model reduction method for the temperature calculation.

In the reduced model, the number of temperature and heat source grid points are temporarily reduced. Once all temperatures are available on the reduced grids by solving the energy conservation equation, the temperature values are returned to the original grid numbers by interpolating between the reduced grid points. When we define the original grid in x coordinate and the reduced grid in x' coordinate in condition of $x'_{m-1} < x_n \leq x'_m$, the temperature of the original grid can be expressed as:

$$T(x_n) = T(x'_{m-1}) + \frac{T(x'_m) - T(x'_{m-1})}{x'_m - x'_{m-1}} \cdot (x_n - x'_{m-1}), \tag{3.47}$$

where n and m are grid numbers at the x and x' coordinates, respectively.

In range of $x_n \leq x'_{m=1}$, temperatures at the original grids are defined as:

$$T(x_n) = T(x'_{m=1}). \tag{3.48}$$

Similarly, for $x_{m=max} \leq x_n$,

$$T(x_n) = T(x_{m=max}). \tag{3.49}$$

The heat sources from the reduced grid points are obtained by averaging the values on the original grid which are located within the reduced grid.

$$\dot{q}_{x'} = \langle \dot{q}_x \rangle_n. \tag{3.50}$$

In this work, we used 12 control volumes for discretization in the reduced coordinate (w coordinate in Figure 3.4).

3.5 Parametrization of the battery model

3.5.1 Physical and geometric parameters of batteries

The physical and geometric parameters of target cells utilized in our simulations are shown in Table 3.2 and 3.3. The thickness and surface area sizes were obtained by measuring the actual electrodes and current collectors that were removed from the target cells. The tortuosities are estimated values. The porosity of the LFP cell was estimated through a Scanning Electron Microscopy (SEM) image taken by Hellwig. The SEM image was also

utilized to estimate the value of the blend cathode cell [129]. The densities are fitted to experimental values within a practical range shown in literature [129; 138]. As for thermal conductivity and capacity, an average value is used for an electrode sandwich [135]. The thermal conductivity and capacity of LFP were referenced from literature and the same values are utilized for the blend material [135; 138]. These parameters were obtained and validated in previous works by Hellwig, Hedwig and Bartsch [129; 135; 138].

As for thermal properties of a cell surface, the convective heat transfer coefficient α_{conv} is set as 5.0 W/(m^2·K) assuming natural convection. The emissivity ϵ_{surf} is estimated as 0.8 from the fact that the values of typical steel casing are reported in a range between 0.7 and 0.9 [129]. Double-layer capacitance and electric resistance used in this work are shown in Table 3.4. These values are based on work by Hellwig [129]. The thickness of SEI is discussed in Section 4.1.

Table 3.2: Physical and geometric parameters of a cell with LiFePO$_4$ cathode [129; 135].

	Unit	Anode	Cathode	Separator	Anode current collector	Cathode current collector
Thickness	[μm]	35.5	79.5	20.0	15.0	15.0
Surface area	[m^2]			0.171		
Tortuosity	-	1.2		1.0	-	-
Porosity		0.27	0.33	0.5	-	-
Density	[kg/m^3]	2541	1512	-	-	-
Thermal conductivity	[W/m·K]			1.02		
Thermal capacity	[kJ/m^3·K]			1850		

Table 3.3: Physical and geometric parameters of a cell with blend (NCA/LMO) cathode [138].

	Unit	Anode	Cathode	Separator	Anode current collector	Cathode current collector
Thickness	[μm]	49.0	50.0	26.4	23.0	31.0
Surface area	[m^2]			0.159		
Tortuosity	-	1.2		1.0	-	-
Porosity		0.27	0.33	0.5	-	-
Density	[kg/m^3]	1650	3238	-	-	-
Thermal conductivity	[W/m·K]			1.02		
Thermal capacity	[kJ/m^3·K]			1850		

Table 3.4: Double-layer capacitance and electric resistance based on work by Hellwig [129].

	Unit	
Anode double layer capacitance	F/m^2	0.02
Cathode double layer capacitance	F/m^2	0.1
Serial resistance	$\Omega \cdot m^2$	5.0×10^{-4}

3.5.2 Kinetic parameters of electrodes

Tables 3.5 and 3.6 show the kinetic parameters of the Butler-Volmer equation for cells with an LFP cathode and a blend cathode, respectively. As mentioned in Chapter 2, we assumed that both cells have the same type of anode. We use a value shown in literature for anodic and cathodic symmetry factors, α, for both target cells [129]. The exchange current densities, i_{00}, for both LFP and blend cells are fitted values with experimental discharge curves of various C-rates and temperatures. The activation energy of the blended cell is assumed to be a value similar to that of NCA and a value shown by Guo et al. were used in our simulation [139]. Other activation energies are obtained through literature or fitted against experiments by Hellwig and Hedwig [129; 135]. The details of the discharge curves of these cells in nominal operational conditions are reviewed in Section 5.1.2. The kinetic parameters of runaway chemistries are discussed in Chapter 4.

Table 3.5: Kinetic parameters for the Butler-Volmer equations of a cell with $LiFePO_4$ cathode [129; 135; 140].

	Unit	Anode	Cathode
Exchange current density i_{00}	$[A/m^3]$	3.12×10^{15}	1.79×10^{12}
Activation energy E_{act}	$[J/mol]$	53411	41367
Symmetry factor α	-	0.5	0.5

Table 3.6: Kinetic parameters for the Butler-Volmer equations of a cell with blend cathode.

	Unit	Anode	Cathode
Exchange current density i_{00}	$[A/m^3]$	3.12×10^{15}	1.275×10^{10}
Activation energy E_{act}	$[J/mol]$	53411	30000
Symmetry factor α	-	0.5	0.5

3.5.3 Thermodynamic properties of pure electrode material

The thermodynamic quantities (entropy and enthalpy of lithium intercalation) of pure electrodes are obtainable through OCV of electrodes. The OCV corresponds to equilibrium potential, ϕ_{eq}, thus the entropy of intercalation is calculated by:

$$\Delta S = -\left(\frac{\partial \Delta G}{\partial T}\right)_{\mathrm{P}} \tag{3.51}$$

$$= zF\left(\frac{\partial \Delta \phi_{\mathrm{eq}}}{\partial T}\right)_{\mathrm{P}}, \tag{3.52}$$

in a one-electron process $(z = 1)$,

$$\Delta S = F\left(\frac{\partial \Delta \phi_{\mathrm{eq}}}{\partial T}\right)_{\mathrm{P}}. \tag{3.53}$$

The definition of enthalpy and free energy (Equation 3.3) gives:

$$\Delta H = \Delta G + T \Delta S \tag{3.54}$$

$$= zF\left\{T\left(\frac{\partial \Delta \phi_{\mathrm{eq}}}{\partial T}\right)_{\mathrm{P}} - E\right\}. \tag{3.55}$$

The thermodynamic properties of electrodes in this work are calculated based on OCV presented in literature. The values as a function of lithium concentrations utilized in this work are shown in Figure 2.6, 2.8, 2.10, and 2.12 in Chapter 2 [138; 140].

3.5.4 Thermodynamic properties of blended electrode material

We obtained the thermodynamic quantities of blend electrode material fromn the observation presented by Tran et al. that shows each component behaves as a pure material within the blend, as explained in Section 2.4.5 [48; 138]. Because of software requirements, we prepared a set of thermodynamic properties that represent the behavior of a NCA/LMO blend by applying weighting factors on the blend components [138]. The specific entropy of lithium intercalation for the blend, $\Delta S_{\mathrm{blend}}$, with units of J/(mol·K) is expressed as:

$$\Delta s_{\mathrm{blend}} = X_{\mathrm{NCA}} \cdot \Delta S_{\mathrm{NCA}} + X_{\mathrm{LMO}} \cdot \Delta S_{\mathrm{LMO}}, \tag{3.56}$$

where X_{NCA} and X_{LMO} are a mole fraction of lithium ions in each component:

$$X_{\text{NCA}} = \frac{n_{\text{NCA}}}{n_{\text{NCA}} + n_{\text{LMO}}} = \frac{c_{\text{NCA}} \cdot w_{\text{NCA}}}{c_{\text{NCA}} \cdot w_{\text{NCA}} + c_{\text{LMO}} \cdot w_{\text{LMO}}}, \quad (3.57)$$

$$X_{\text{LMO}} = \frac{n_{\text{LMO}}}{n_{\text{NCA}} + n_{\text{LMO}}} = \frac{c_{\text{LMO}} \cdot w_{\text{LMO}}}{c_{\text{NCA}} \cdot w_{\text{NCA}} + c_{\text{LMO}} \cdot w_{\text{LMO}}}, \quad (3.58)$$

where c_{NCA} and c_{LMO} are lithium concentrations, and w_{NCA} and w_{LMO} are weight ratios of NCA and LMO to the total mass of the blend, respectively. Similarly, we obtained the enthalpy of lithium intercalation for the blend [138]. The thermodynamic quantities utilized in this work are shown in Figure 3.5.
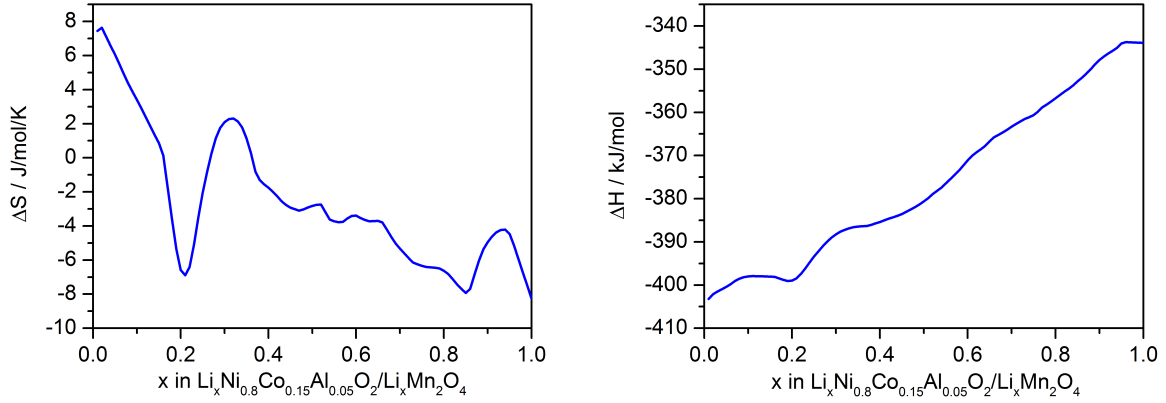
(a) Entropies of lithium intercalation.   **(b)** Enthalpies of lithium intercalation.

Figure 3.5: Thermodynamic properties of NCA/LMO blend cathode [138].

The validation of the thermodynamic properties and the weighting method have been reported by Bartsch [138].

3.5.5 Thermodynamic properties of runaway chemistry

Thermodynamic properties, i.e., enthalpies of formation, of species in runaway chemistry are necessary to calculate the reaction enthalpies. For most species, the thermodynamic properties are described by NASA polynomials that provide temperature dependent thermodynamic properties [141]. We chose the NASA polynomials with five terms in the heat capacity instead of one with seven terms due to a restriction with the Cantera software. When the polynomials are not available for a species in a database, we took one of three choices: (1) estimate temperature-independent values through available thermodynamic properties of a reaction such as the reaction enthalpy, (2) use a temperature-independent

value shown in literature, or (3) calculate the polynomial using available heat capacities lists.

In our models, we derived the thermodynamic properties of a metastable SEI, $(CH_2OCO_2Li)_2$, NCA, $LiNi_{0.8}Co_{0.18}Al_{0.05}O_2$, and decomposed NCA, $LiNi_{0.8}Co_{0.18}Al_{0.05}O$, utilizing the reaction enthalpy of SEI decomposition and NCA decomposition, respectively.

Table 3.7: Thermodynamic property of metastable SEI and NCAs.

Species	H_0 [kJ/mol]
$(CH_2OCO_2Li)_2$	-1513.2
$LiNi_{0.8}Co_{0.18}Al_{0.05}O_2$	-221.6
$LiNi_{0.8}Co_{0.18}Al_{0.05}O$	-33.6

The temperature-independent properties in literature are chosen for a stable SEI, Li_2CO_3, and LiC_6.

Table 3.8: Thermodynamic property of stable SEI and LiC_6.

Species	H_0 [kJ/mol]
Li_2CO_3	-1214.1
LiC_6	-11.65

We derived NASA polynomial coefficients of liquid and gaseous ethylene carbonate. This approach is possible when lists of heat capacities in various temperatures are available for a species. These polynomials have three types of equations: heat capacity (Equation 3.59), standard enthalpy of formation (Equation 3.60), and standard entropy of formation (Equation 3.61).

$$\frac{C_p^0(T)}{R} = a_1 + a_2 T + a_3 T^2 + a_4 T^3 + a_5 T^4. \tag{3.59}$$

$$\frac{H^0(T)}{RT} = a_1 + a_2 \frac{T}{2} + a_3 \frac{T^2}{3} + a_4 \frac{T^3}{4} + a_5 \frac{T^4}{5} + \frac{b_1}{T}. \tag{3.60}$$

$$\frac{S^0(T)}{R} = a_1 \log T + a_2 T + a_3 \frac{T^2}{2} + a_4 \frac{T^3}{3} + a_5 \frac{T^4}{4} + b_2. \tag{3.61}$$

First, we obtained coefficients $a_1 \sim a_5$ by curve fitting Equation 3.59 with an available series of heat coefficients as a function of temperature. The series of the heat coefficients for gas and liquid EC are taken from a data set published by the National Institute of Standards and Technology (NIST) and Vogdanis et al., respectively [142; 143]. Tables 3.9 and 3.10 show the series of heat capacity used in this work. Figure 3.6 shows the results

of curve fitting for the NASA polynomials of heat capacity over a gas constant. The coefficients of each term are assumed to be $a_1 \sim a_5$. The values obtained are summarized in Table 3.11.

Then, b_1 is calculated with standard enthalpies of formation for gas and liquid EC ($H^0_{g(T=237K)} = -604.3$ kJ/mol, $H^0_{l(T=237K)} = -578.0$ kJ/mol) at 298 K by substituting the coefficients $a_1 \sim a_5$ obtained with the heat capacity into Equation 3.60. We refer the NIST database for standard enthalpies.

Obtaining b_2 is not as simple as getting b_1 because the standard entropies of formation are not available for neither gas nor liquid EC (S^0_g, S^0_l). Thus, the standard enthalpy of formation for liquid EC is obtained by applying the entropy of phase transition between solid and liquid obtained by Equation 3.62. Here, the standard entropy for solid ($S^0_s = 132.54$ J/mol·K) is taken from the NIST [133; 142].

$$\Delta S_{\text{trans}} = \frac{\Delta H_{\text{trans}}}{T}. \tag{3.62}$$

Likewise, the standard enthalpy of formation for gas is obtained through the entropy of phase change between liquid and gas. The entropies of the phase change are also taken from the NIST database [142]. The standard entropies of formation for liquid and gas used in this work are $S^0_l = 175.0$ J/mol·K and $S^0_g = 315.0$ J/mol·K.

The coefficients for the NASA polynomials utilized in this work are shown in Table 3.11. The details of the reactions of runaway chemistry are discussed in Chapter 4 and the coefficients shown here are utilized in our simulation.

$y = 5.0 \times 10^{-12}x^4 - 4.0 \times 10^{-9}x^3 - 2.0 \times 10^{-5}x^2 + 0.0436x - 1.16$ $y = 8.0 \times 10^{-5}x^2 + 0.1003x - 3.9763$

(a) Gaseous EC   **(b)** Liquid EC
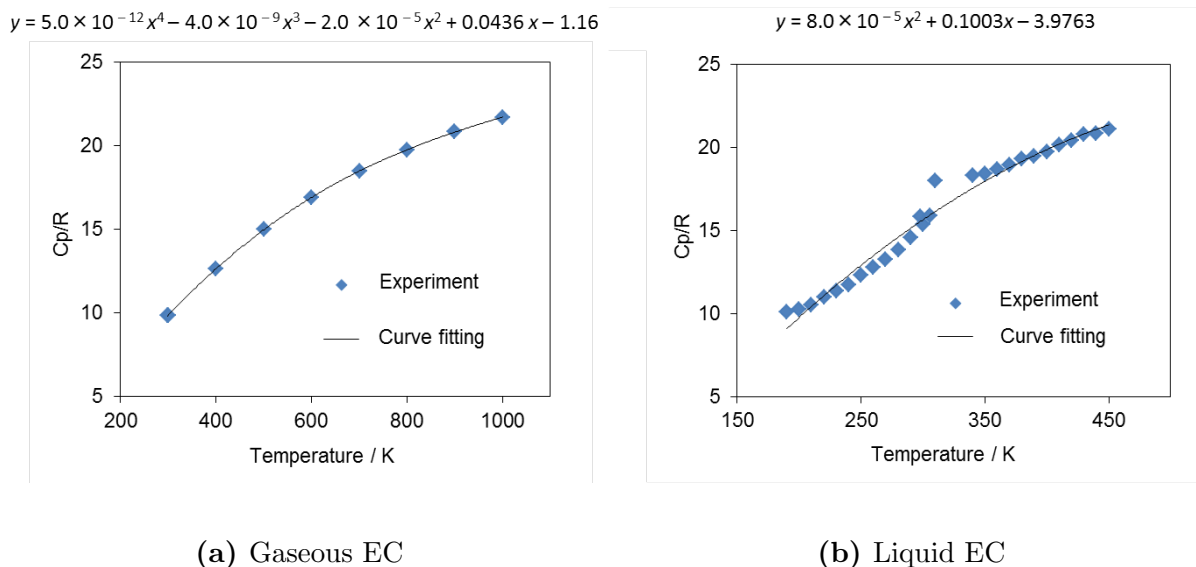
Figure 3.6: Curve fitting of C_p/R for the NASA polynomials of gaseous and liquid EC [142; 143].

Table 3.9: Heat capacity of gas EC [142]

T [K]	C_p/R	C_p [J/mol· K]
298.15	9.81	81.6
300	9.86	82.0
400	12.6	104.9
500	15.0	124.5
600	16.9	140.5
700	18.5	153.5
800	19.7	164.1
900	20.8	173.0
1000	21.7	180.4

Table 3.10: Heat capacity of liquid EC [143]

T [K]	C_p/R	C_p [J/mol· K]
180	7.20	59.90
190	10.11	84.10
200	10.26	85.30
210	10.50	87.30
220	10.97	91.20
230	11.35	94.40
240	11.75	97.70
250	12.32	102.4
260	12.76	106.1
270	13.24	110.1
280	13.82	114.9
290	14.56	121.1
298	15.83	131.6
300	15.36	127.7
306	15.89	132.1
310	18.00	149.7
340	18.32	152.3
350	18.43	153.2
360	18.69	155.4
370	18.95	157.6
380	19.28	160.3
390	19.48	162.0
400	19.75	164.2
410	20.12	167.3
420	20.39	169.5
430	20.76	172.6
440	20.81	173.0
450	21.07	175.2

Table 3.11: Coefficients of the NASA polynomials for gas and liquid EC, $C_3H_4O_3$.

Species	a_1	a_2 [1/K]	a_3 [1/K^2]	a_4 [1/K^3]	a_5 [1/K^4]	b_1 [K]	b_2
EC gas	-1.17	0.0436	-2.0×10^{-5}	-4.0×10^{-9}	5.0×10^{-12}	-6.19×10^4	32.4
EC liquid	-6.9763	0.1003	-0.00008	0.0	0.0	-7.11×10^4	34.5

3.6 Simulation software

3.6.1 DENIS

The host software utilized in this work is an in-house developed software package, DENIS (Detailed Electrochmistry and Numerical Impedance Simulation) that has been worked on by Prof. Bessler and his group since 2004 [144; 145]. DENIS was originally developed for the numerical simulation of fuel cells such as a Solid Oxide Fuel Cell (SOFC) and a Polymer Electrolyte Membrane Fuel Cell (PEMFC). It was later extended to battery models including a conventional lithium ion battery, a lithium-oxygen battery, and a lithium-sulfur battery [134; 146; 147].

DENIS is written in C/C++ and is capable of conducting electrochemical simulations in 1D and in both transient and steady-state simulations. All of the simulations in this work are conducted using a transient simulation to reproduce phenomena such as linear heating of a cell and components, which is in a similar environment as differential scanning calorimetry (DSC). DENIS consists an extrapolation integrator for linearly implicit ODEs (LIMEX) to solve Ordinary Differential Equations (ODE) and Differential-Algebraic Equations (DAE) [148].

In this work, the battery electrochemistry (i.e., the Butler-Volmer equation) is solved in DENIS, and the runaway chemistries are managed in Cantera (Figure 3.7). DENIS reads ASCII based input files from DENIS and Cantera as well as thermodynamic parameter data of a cathode and an anode, and handles them accordingly. We can specify general settings such as spatial computational discritizations, phase management, or battery kinetic parameters in the DENIS input file. DENIS interacts with Cantera in each time step and DENIS provides state variables such as temperature, pressure, or concentrations of species, while CANTERA returns chemical source terms. The governing equations of battery electrochemistry are solved in LIMEX. TDENIS also outputs ASCII based text files which allows easy handling of data in a commercial software for scientific graphing and data analysis. Details on Cantera are explained in Section 3.6.2.

3.6.2 Cantera

Cantera software is an object-oriented C++ based software toolkit for chemical kinetics, thermodynamics, and transport processes [131]. It is an open source software that was developed by Prof. Goodwin at the California Institute of Technology and is coupled internally with DENIS. Cantera is functionally available throughout the simulation time of the host software, DENIS.
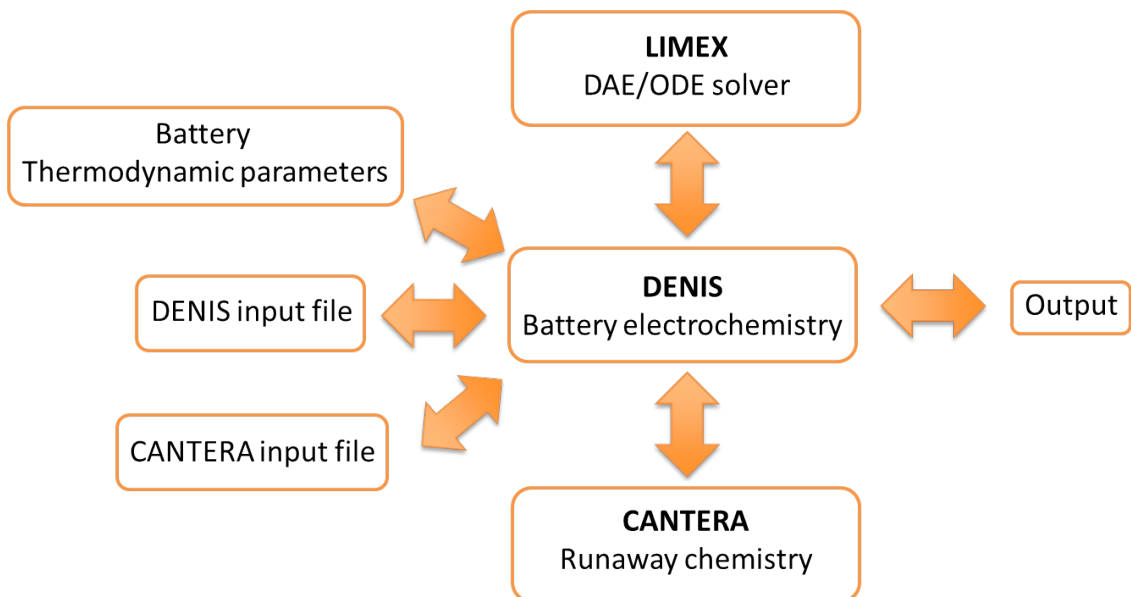
Figure 3.7: Schematics of software coupling.

We added a feature which enables researchers to calculate reaction enthalpy in Cantera in order to realize thermal simulation of runaway chemistry. In this work, Cantera specifically returns reaction enthalpies and reaction rates of runaway chemistries to DENIS that are represented in Equations 3.41, 3.42, 3.43, and 3.44.

The kinetic and thermodynamic parameters of runaway chemistries shown in Section 3.5.5 and Chapter 4 are stated in a Cantera input file. The charge-transfer and non-charge-transfer reactions are set as "edge_reaction" and "surface_reaction" in the Cantera definition, respectively. The electron is set as a metal type species so Cantera ignores the concentration of electrons when it calculates the reaction rate while the solid phase is specified as an incompressible solid. In addition to the thermodynamic properties discussed in Section 3.5.5, other parameters are taken from the pre-installed database with Cantera in which general parameters of common gaseous types such as oxygen or carbon dioxide are available. Most of the parameters in the database are in the form of the NASA polynomials.

3.6.3 Simulations of differential scanning calorimetry (DSC)

In this work, simulations of DSC that are made for both validating and estimating thermodynamic/kinetic parameters will be explained in Chapter 4.

Differential scanning calorimetry (DSC) is an experimental thermoanalytical technique that measures energy transferred as heat to or from a sample at constant pressure during physical or chemical changes [133]. It includes the term "differential" because of the

behavior of the sample is compared to that of a reference material (Figure 3.8) [133]. The term "scanning" refers to the temperature of the sample and the reference are scanned during the analysis [133]. An important restriction of DSC is that the temperature of the sample needs to be homogeneous throughout the material. This means that the sample must be small enough in order of micrograms so that a temperature gradient does not appear inside.
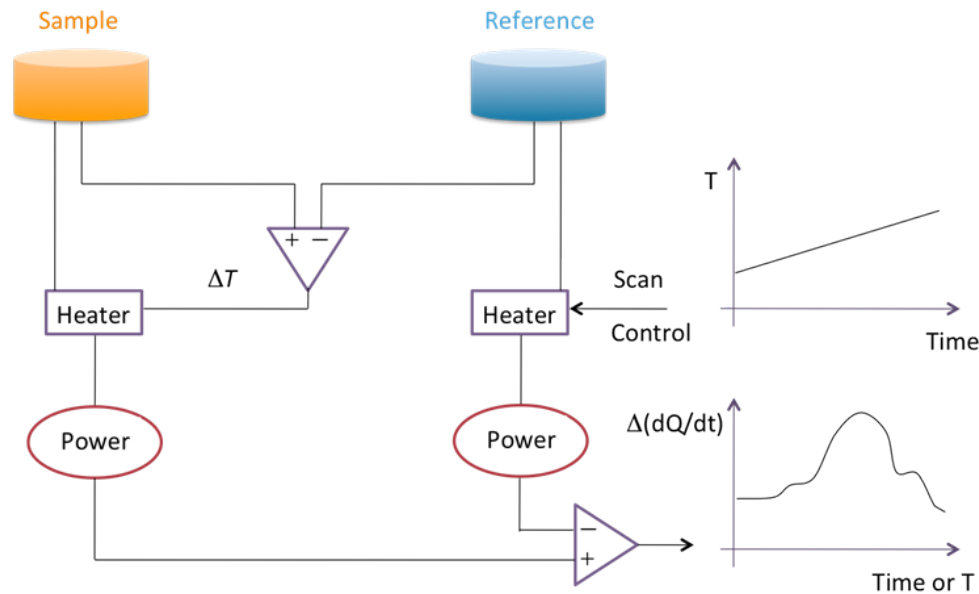
Figure 3.8: Schematics of DSC.

When no physical or chemical changes happen in the sample under a temperature change of $\Delta T = T - T_0$, the heat transferred to the samples can be described as:

$$q_p = C_p \Delta T \tag{3.63}$$

where we assume that C_p is independent of temperature.

In DSC, generally, the temperature is changed linearly. Therefore, we define the ΔT as βt so that $T = T_0 + \beta t$ where t is time. With the chemical and physical changes, the heat transferred would be $q_p + q_{ex}$ where q_{ex} is additional energy required to get the same change in temperature of the sample [133]. The heat, q_{ex}, can also be stated as a change in the heat capacity at constant pressure, C_p [133]:

$$C_{p,\text{ex}} = \frac{q_{p,\text{ex}}}{\Delta T} \tag{3.64}$$

$$= \frac{q_{p,\text{ex}}}{\beta t} \tag{3.65}$$

$$= \frac{P_{\text{ex}}}{\beta} \tag{3.66}$$

where P_{ex} is the additional electrical power used to equalize the temperature of the sample and the reference. In a typical DSC, the heat flow is traced through electrical power.

The definition of heat capacity at constant pressure is:

$$C_p = \left(\frac{\partial H}{\partial T} \right)_p . \tag{3.67}$$

With Equation 3.67, the enthalpy change within a temperature change between T_1 and T_2 of the sample can be expressed as:

$$\Delta H = \int_{T_1}^{T_2} C_{p,\text{ex}} dT \tag{3.68}$$

Equations 3.68 and 3.64 also imply that the sum of the heat transferred would be the enthalpy change. The formulations in CANTERA and DENIS use this theory to return the heat released from a target material and reproduce DSC results to effectively compare with experiments.

4 Results I: Development of chemical reaction mechanisms for thermal runaway

This chapter describes model developments and validations of chemical reaction mechanisms for thermal runaway. We investigated four types of exothermic runaway chemistries: (1) SEI formation (Section 4.1), (2) SEI decomposition (Section 4.2), (3) a combination of oxygen evolution from cathode material and solvent oxidation (Section 4.3), and (4) a combination of ethylene oxidation and lithium hydration (Section 4.4). The runaway chemistries were established in global reaction forms and the reaction parameters were obtained either through literature or fitting simulation results to experimental DSC data. DSC simulations were conducted for each electrode to validate and obtain the kinetic parameters of the global reactions.

4.1 SEI formation

4.1.1 Modeling and parametrization

We included the SEI in our model as it is known that SEI decomposition is the first exothermic reaction in thermal runaway situations as already reviewed in Section 2.6. Here, we explain the SEI formation mechanism implemented in our battery model to show general characteristics of the passivation layer in this section. The SEI formation is an exothermic reaction and it is believed that it also plays an important role in aging mechanism of a cell. Therefore, in addition to the SEI decomposition, it can be said that SEI formation constitutes a degradation mechanism in the cell. We assumed an irreversible global reaction (equation 4.1) for the SEI formation reaction which has been studied by Wang et al. utilizing Density Functional Theory (DFT) simulations as discussed in Section 2.6 [73]. SEI formation is a reaction involving charge transfer at the negative electrode.

$$C_3H_4O_3 + Li^+ + e^- \rightarrow 0.5\,(CH_2OCO_2Li)_2 + 0.5\,C_2H_4 \tag{4.1}$$

Ethylene carbonate ($C_3H_4O_3$) decomposes reacting with lithium ions and the metastable SEI (i.e., lithium ethylene dicarbonate, $(CH_2OCO_2Li)_2$) is formed as a product (Figure 4.6).
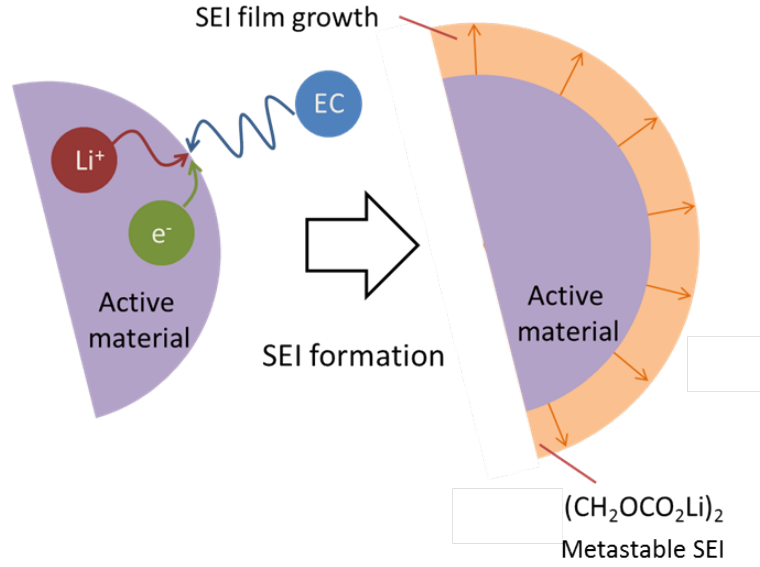
Figure 4.1: Schematics of SEI formation.

The rate constant of SEI formation is based on an a battery aging model by Safari et al. in which they also refer the DFT study by Wang et al. [149]:

$$k_{form} = f_f \prod_i c_i^{a_i} \exp\left(-\frac{\alpha F}{RT}\phi\right). \tag{4.2}$$

The parameters of Equation 4.2 are summarized in Table 4.1. In this study, we assume the reaction to be first order with respect to both the ethylene carbonate and the lithium ion concentration. Frequency factor is derived as $f_f = B \cdot f_f'$ to meet the unit of the rate constant following typical procedures for a CANTERA input file in this work. B is a constant whose unit depends on reaction orders and number of species.

In addition to the aging model, we included a SEI film growth model for the volumetric active surface area, A_{surf}, of the SEI formation reaction. In DENIS, the rate constant is multiplied with the active surface area to apply a 1D reaction to a 3D structure in order to obtain a volumetric reaction rate from surface reactions.

Table 4.1: Kinetic parameters for the SEI formation, †: based on ref. [149], ‡:assumed

Parameter	Unit	
Frequency factor, f_f'	[m/s]	$1.36 \times 10^{-12\dagger}$
Symmetry factor, α	-	$0.5^\dagger$
Reaction order of EC, $a_{C_3H_4O_3}$	-	$1^\dagger$
Reaction order of Li$^+$, a_{Li^+}	-	$1^\ddagger$

$$r_v = k \cdot A_{surf}. \tag{4.3}$$

We assumed exponential decay for the active surface area as a function of the SEI volume fraction, i.e., the SEI thickness. The employed functional relation is based on general assumptions of film growth, i.e., the active surface area diminishes as SEI grows (Equation 4.4) [150].

$$A_{surf,SEIform} = A_{surf,init} \exp\left(-\epsilon_{SEI} \cdot a_{growth}\right), \tag{4.4}$$

where ϵ_{SEI} and a_{growth} are the volume fraction of SEI and a film growth rate constant, respectively.

The initial volume specific surface area of SEI is estimated as 4.0×10^7 m^2/m^3.

Table 4.2: SEI thickness and active material parameters. The spherical partical is assumed to be 1 µm.

SEI thickness [nm]	1	10	100
SEI volume [m^3]	1.26×10^{-20}	1.27×10^{-19}	1.39×10^{-18}
Volume fraction of SEI	0.002	0.020	0.221

The film growth rate constant, a_{growth}, was chosen in a way that the SEI volume fraction (i.e., thickness) remains nearly constant at a certain value (i.e, SEI volume fraction increase is within 5% approximately in 4 days). To calculate the target volume fraction associated with the SEI thickness, we assumed a spherical particle for the active material and with a radius of approximately 1 µm according to Colclasure et al. [151]. As for the volume fraction of the active material, we use 0.33 as shown in Section 3.5.1. With these parameters, the volume fraction of SEI was estimated approximately between 0.002 and 0.2 as shown in Table 4.2 from the SEI thickness which has been reported in a range from 1 nm to 100 nm [66]. The simulation results with various film growth rate constants are shown in Section 4.1.2 and are compared at different temperatures in various state of charges.

4.1.2 Results and discussion

We investigated the characteristics of the film growth model with Equation 4.4 as a function of a film growth rate constant, a_{growth}. Simulations of SEI formation were conducted with various film growth rate constants (a_{growth} = 100, 250, 500, and 1000) under constant temperatures, 303 and 404 K, in fully charged condition (SOC = 100%). Figure 4.2 shows profiles of SEI volume fractions in an anode. SEI film is formed mainly by a potential between fully charged active material and electrolyte. The film grows rapidly until 0.1×10^6 sec (27 h), and then the decay in growth rate becomes prominent. The smaller the film growth rate constant becomes, the faster the SEI volume fraction increases following exponential characteristics. Temperature dependence of SEI film growth is more notable with a smaller film growth rate constant. When the film growth rate constant is 100, SEI volume fractions reach values of approximately 0.85 and 0.9 in 1.2×10^6 s (333 h) at temperatures of 303 K and 403 K, respectively. On the other hand, with a film growth rate constant of 500, the volume fractions of SEI reach 0.02 for both 303 K and 403 K in 333 h.
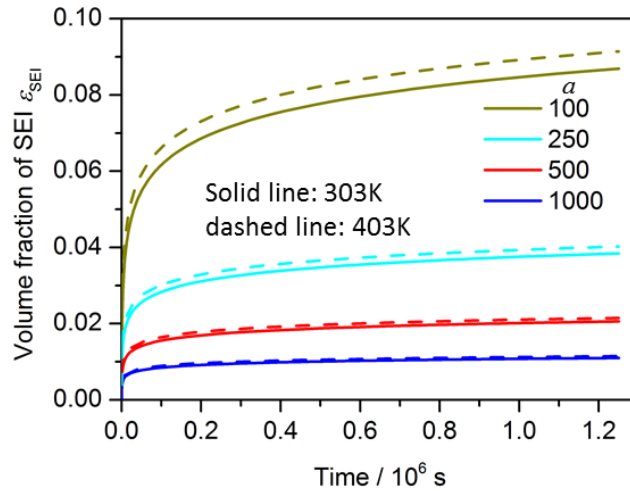
Figure 4.2: Volume fraction of SEI under the assumption of exponential film growth with various film growth rate constants, *a*.

In addition to the constant temperature, we examined the film growth behavior under a heating rate of 5K/min between 303K to 523 K in SOC of 100% and 50% (Figure 4.4a). The model behavior considering a constant heating rate was also checked as a preliminary study for the DSC simulation. Once the temperature reaches 523 K from the initial temperature of 303K, the temperature is kept constant. Due to the higher temperature, the SEI volume fraction in $a = 100$ case reaches approximately 0.9 and 0.95 which are 0.05 higher than that achieved considering a constant temperature of 303 K as shown in Figure 4.2. Similar to the dependence on temperature, the dependence on SOC is more
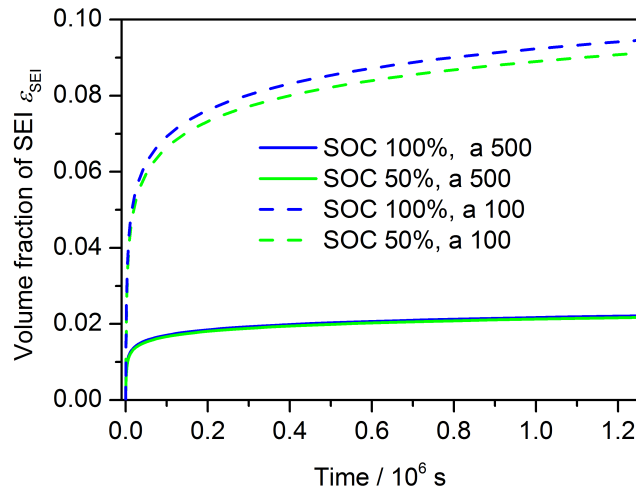
Figure 4.3: Volume fraction of the SEI with a SOC of 50 and 100% and a film growth rate constant of 100 and 500, respectively.

noticeable with a smaller film growth rate constant. The difference in model behavior between the SOC of 50% and 100% cases shows that the effect of the potential difference between active material and electrolyte is successfully included.

Moreover, heat flow is also examined in the same condition. Figure 4.4b shows the heat flow profile up to 15000 s (approximately 4 h). At 2640 s, a kink is observed as temperature reaches 523 K. Compared to SEI decomposition, SEI formation releases one order of magnitude less heat flow. During the temperature ramp, the heat flow is higher in the SOC 100% cases than in the SOC 50% cases because of faster SEI film growth as shown in Figure 4.4a. However, after reaching the constant temperature of 523 K, 100% cases exhibit almost the same amount of heat flow as 50% cases: the film growth rates in both SOC cases are nearly equal then. Figure 4.4a also shows that SEI volume fraction reaches over 0.045 by 15000 s when film growth rate constant is 100.

Considering that the SEI volume fraction of experimental data is within a range of 0.002 to 0.2 as shown in Section 4.1.1, the film growth rate constant needs to be approximately between 50 and 1000 from the discussion above. In this work, the film growth rate constant was assumed to be 100.
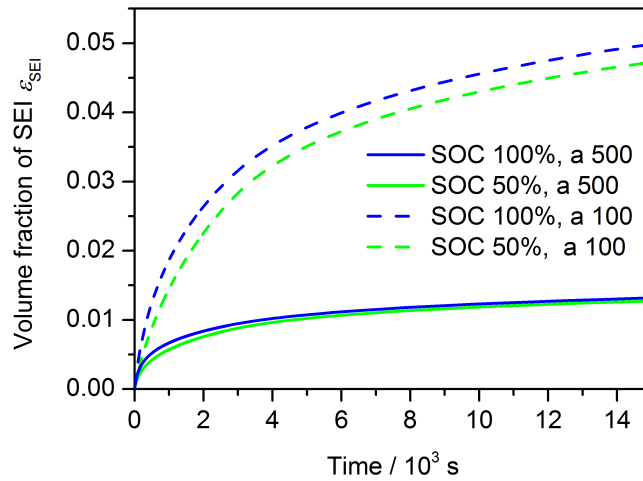
(a) SEI volume fraction
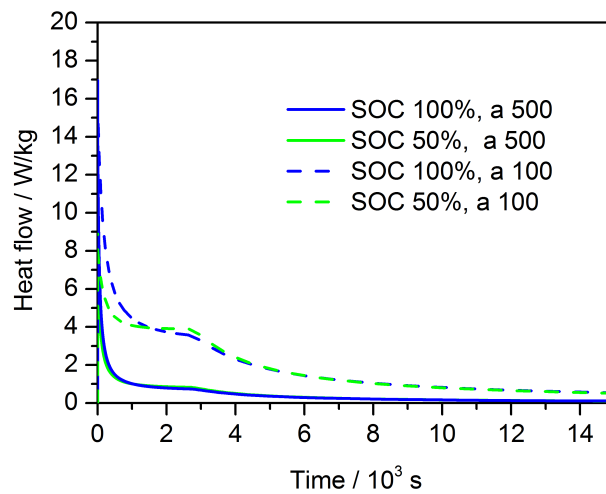
(b) Heat flow

Figure 4.4: SEI volume fraction and heat flow profiles at an SOC of 50% and 100% respectively with a flim growth rate constant of 100 and 500. Temperature, which initially is 303 K, remains constant, once it reaches a value of 523 K with constant heating rate of 5 K/min.

4.2 SEI decomposition

4.2.1 Modeling and parametrization

As another runaway mechanism on the anode side, we modeled an SEI decomposition reaction.

The SEI decomposition was modeled based on the reactions proposed by Aurbach and Wang et al. [73; 75]. This model was established in a global reaction form and assumes that the metastable SEI (lithium ethylene dicarbonate, $(CH_2OCO_2Li)_2$) becomes the stable SEI (lithium carbonate, Li_2CO_3) releasing oxygen, carbon dioxide and ethylene at a temperature of approximately 373 K and above as shown in Equation 4.5.

$$(CH_2OCO_2Li)_2 \rightarrow Li_2CO_3 + C_2H_4 + CO_2 + 0.5O_2 \qquad (4.5)$$
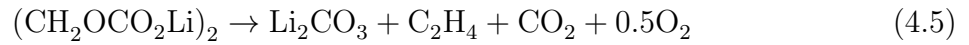
Here, C_2H_4, CO_2 and O_2 are realeased as gas (Figure 4.5).
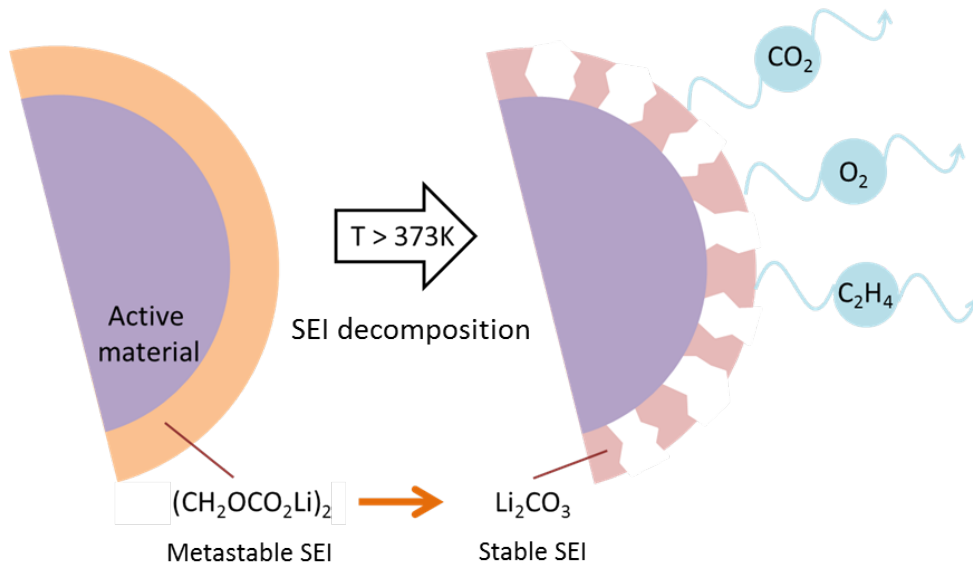
Figure 4.5: Schematics of SEI decomposition.

The reaction rate was modeled with an Arrhenius equation (Equation 4.6) assuming first-order kinetics.

$$k_{\text{decomp}} = f_d c_{\text{SEI}} \exp\left(-\frac{E_{\text{act}}}{RT}\right). \qquad (4.6)$$

This equation has the form of a non-charge trasfer reaction rate which is explained in Chapter 3. For the SEI decomposition simulation, this first-order assumption was taken

from theory proposed by Spotnitz et al. [21]. The kinetic parameters, an activation energy, E_{act}, and the reaction enthalpy (heat of reaction), ΔH, were also referenced from data by Spotnitz et al. [21]. A frequency factor, f_d was adjusted by fitting the model to the DSC result of SEI decomposition by Spotnitz et al.. These parameters are shown in Table 4.3. The enthalpy of formation of the metastable SEI was obtained using the heat of reaction by considering the difference between enthalpies of reactants and products. The weight to molar ratio was also taken from literature (Spotnitz et al.) [21].

Table 4.3: Kinetic parameters for the SEI decomposition by Spotnitz et al. [21]

Parameters	Unit	
Frequency factor	[m/s]	3.426×10^{30}
Activation energy	[J/mol]	2.81×10^5
Heat of reaction	[J/g]	257

Considering the higher density of the stable SEI as compared to the metastable SEI, we assumed that the surface of the active material can be exposed when $(CH_2OCO_2Li)_2$ turns to Li_2CO_3 as shown in Figure 4.5. The initial value of the volume specific surface area for the SEI decomposition was estimated as 5.0×10^7 m^2/m^3.

In the next section, in order to verify our SEI decomposition model and the implementation, we compare the DSC simulation result with a DSC result by Spotnitz et al. at a 10 K/min heating rate. The volume specific active surface area for the SEI decomposition reaction and its change is also discussed. Furthermore, we examined how parameters such as the activation energy and heating rates influence on DSC heat flow profiles.
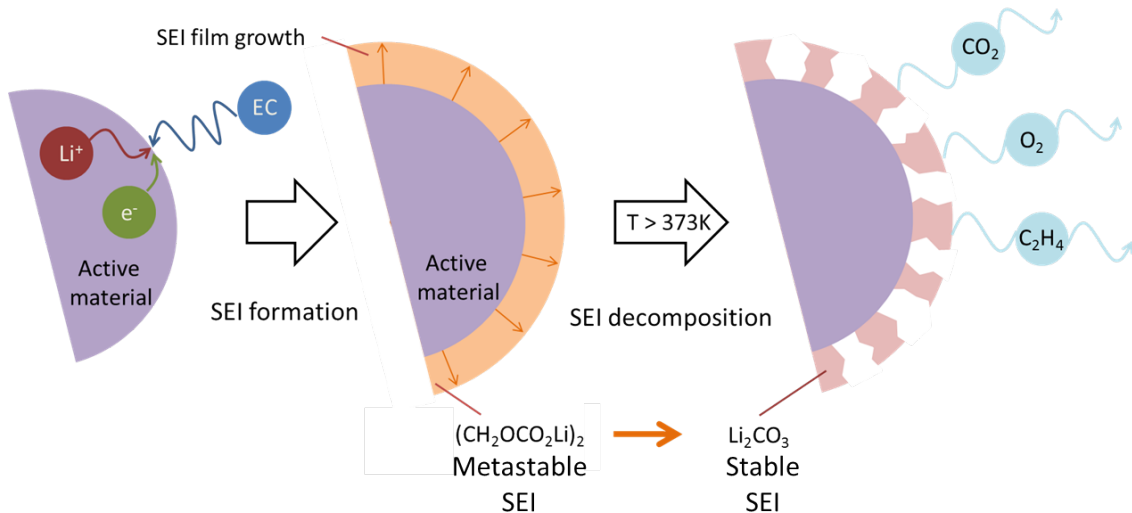
Figure 4.6: Schematics of SEI formation and decomposition.

Finally, utilizing both SEI formation (Section 4.1) and decomposition model, a DSC simulation of simultaneous reactions was conducted (Figure 4.6). The result is compared

with an experimental DSC result by Pasquier et al. [82]. In this simulation, we used a different frequency factor from the values shown in Section 4.2.1 because the peak of heat flow in the DSC experiment in Pasquier et al. is approximately 30 K higher than that of Spotnitz et al.. We chose 3.426×10^{26} m/s for the frequency factor in this simulation by fitting to Pasquier's experimental DSC result. At the same time, the initial volume fraction of SEI in this simulation was set as 0.18 due to a lower heat flow peak of the DSC experimental results than that of Spotnitz et al.. As for other parameters, the heating rate was set as 5 K/min in the same condition as that of Pasquier et al.. The initial volume fraction of ethylene carbonate was estimated based on a ratio of electrolyte (EC:DMC = 2:1) as shown by Pasquier et al.. We assumed that only EC contributes to the SEI formation as proved by experimental observation discussed in Section 2.6.1. In this DSC simulation, we focused on a temperature range from 363 K to 525 K in which the simultaneous reactions happen. The simulation result and the comparison to experimental data are shown in Section 4.1.2.

4.2.2 Results and discussion

DSC simulations of SEI decomposition were conducted to validate the parameters shown in Table 4.3. Figure 4.7 shows the comparison between our DSC simulations and results from Spotnitz et al. [21; 152]. The heat flow shows good agreement in the process of SEI decomposition considering a heating rate of 10 K/min. The SEI volume fraction profile indicates that SEI decomposes the most when the heat flow reaches its peak at approximately 385 K. The heat flow has an offset of 0.3 W/g based on the initial heat capacity and the heating rate as generally seen in experimental DSC data:

$$\dot{q}_{\text{offset}} = C_p^{\text{init}} \cdot \frac{dT}{dt}, \tag{4.7}$$

where C_p^{init} is the heat capacity (1.79 J/g·K) which is taken from Table 3 in Spotnitz et al. [21].

In the particular case discussed here, the initial volume fraction of SEI needed to be 0.85 to agree with the result shown by Spotnitz et al.. A volume fraction of 0.85, however, is too high when compared to the range of SEI volume fractions typically observed experimentally (see Section 4.1). Also, the simulated maximal heat flow is not fully in agreement with experimentally observed maximal heat flows. The simulated maximal heat flow is approximately 8 times higher than that of other DSC experimental results for graphitic anode materials, although still the assumption of the first-order reaction captures the qualitative behavior of SEI decomposition: the less the initial volume fraction becomes,
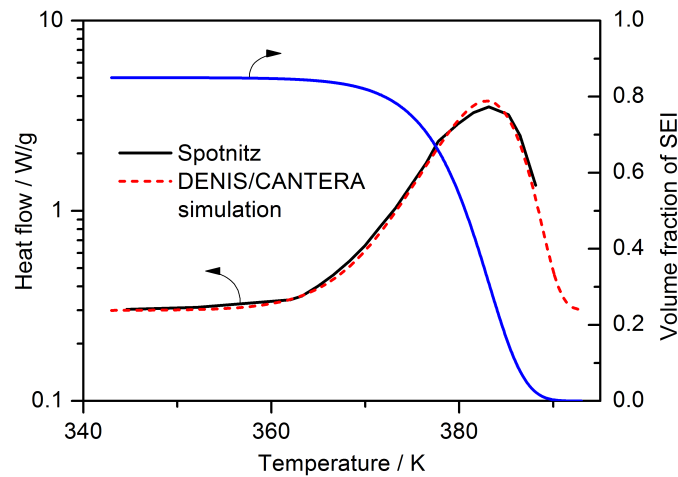
Figure 4.7: Comparison of DSC simulations with result by Spotnitz et al. [21; 152].

the less heat is released as shown in Figure 4.8. Therefore, the initial volume fraction was adjusted to reasonable values either by fitting to the experiment conducted by Pasquier et al. or by taking a realistic value within an experimentally observed range of SEI thickness in the following sections.
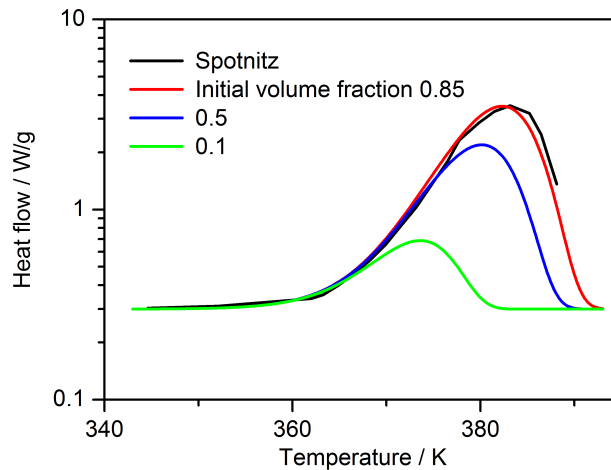
Figure 4.8: DSC simulation with various initial volume fractions of SEI in comparison with the DSC curve by Spotnitz et al. [21].

The SEI decomposition simulation also includes a model of a volume specific active surface area considered for the reaction to handle the volumetric effects of the SEI film decomposition in 1D simulations, similar to Equation 4.4 introduced for the SEI formation. This model uses a hyperbolic tangent and the following function is multiplied with the volumetric active surface area of the SEI decomposition reaction:

$$A_{\text{surf,SEIdecomp}} = \tanh\left(\frac{\epsilon_{\text{SEI}}}{a_{\text{decomp}}}\right),\tag{4.8}$$

where ϵ_{SEI} is the volume fraction of SEI, and a_{decomp} is a constant to be determined.

When the constant a_{decomp} is small enough, the volume specific active surface area remains at the initial value until the volume fraction nearly reaches zero due to a characteristics of the hyperbolic tangent that returns unity for high values. On the other hand, when the constant a has the same value as the initial volume fraction of SEI, the volumetric active surface area linearly decreases. Figure 4.9 shows comparison of DSC simulation results with various constants a. When the changes in the volumetric surface area are small ($a = 10^{-15}, 0.1$), the curve of heat flow shows sharp peak because of a sudden termination of the reaction. In fact, as shown in the experimental curves (Pasquier et al.), DSC experiments do not exhibit a sharp peak for the heat flow indicating a change in the reaction surface area [82]. With $a_{\text{decomp}} = 0.85$, the same value as the initial volume fraction of SEI, the heat flow curve shows good agreement with the curve of Spotnitz et al.. Therefore, the constant a_{decomp} is set in the same value as the initial volume fraction of SEI in the following sections.
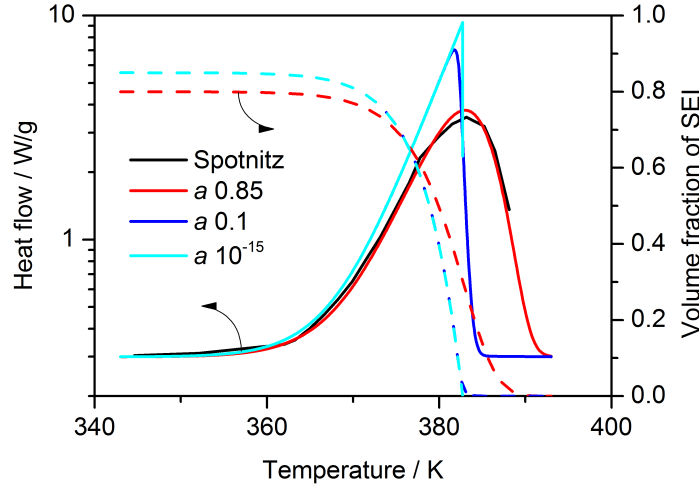
Figure 4.9: DSC simulation with various volumetric active surface area.

To verify the activation energy of the SEI decomposition, we examined heat flows of DSC simulations with activation energies of 285, 281, 275 and 270 kJ/mol (Figure 4.10). The lower the activation energies become, the lower the peak temperature shifts although the shape of curves is identical among all activation energies in the temperature range between 340 K and 400 K. Figure 4.10 shows that 5 kJ/mol difference in activation energy results in 10 K shifts of the heat flow peak. The activation energy of 281 kJ/mol gives the best agreement with the curve of Spotnitz et al..
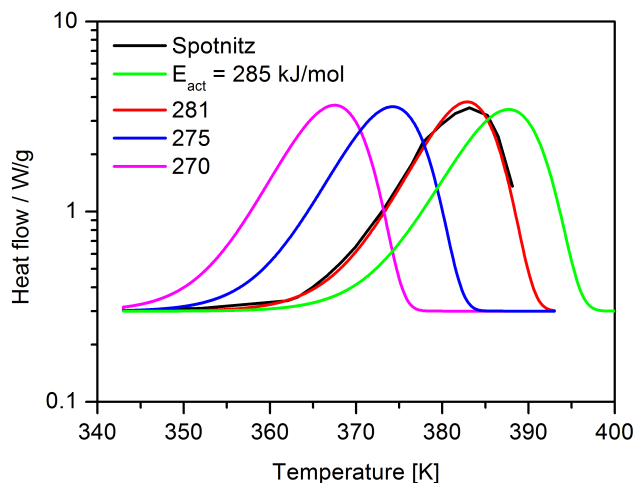
Figure 4.10: DSC simulation with various activation energies in comparison with the DSC curve by Spotnitz et al. [21].

Similar characteristics are observed when the frequency factor is varied: the shape of the curve does not change, however, the peak is shifted within temperatures ranging from 340 K to 400 K (Figure 4.11). The curve shifts approximately 10 K when the frequency factor differs an order of magnitude. The frequency factor of 3.426×10^{30} m/s agrees with the curve of Spotnitz et al.
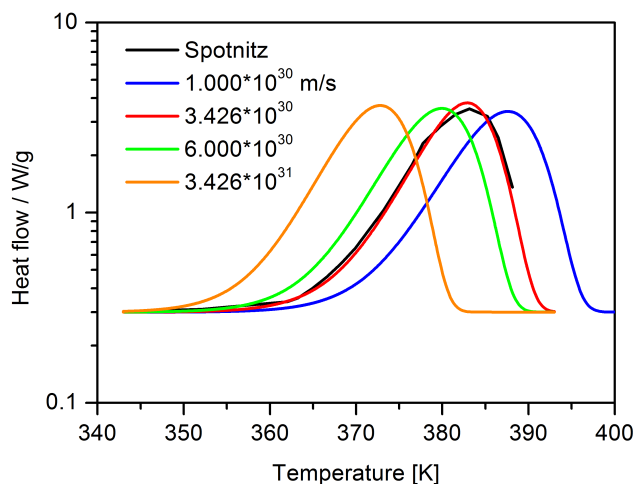
Figure 4.11: DSC simulation with various frequency factors in comparison with DSC curve by Spotnitz et al. [21].

In addition to the validations of the parameters discussed so far, heating rates are varied in 5, 10 and 20 K/min to see the effect on heat flow using the same parameters (Figure 4.12). The maximum heat flow is smaller when the heat rate is lower. This is because a smaller amount of SEI remains at a higher temperature with a lower heating rate, as
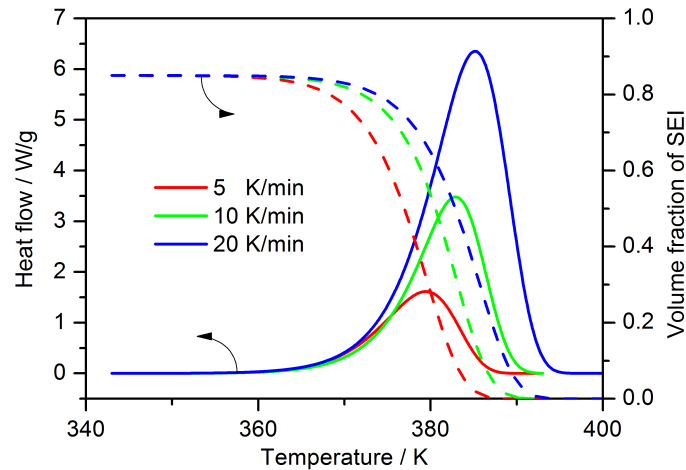
Figure 4.12: DSC simulation with various heat rates of 5, 10 and 20 K/min and temporal evolution of SEI volume fraction.

seen in profiles of SEI volume fractions, due to keeping the SEI at a lower temperature for longer time such that SEI decomposition can already happen. Another reason why larger heat flow is observed at a higher temperature is that the rate of progress of the reaction is also higher due to the Arrhenius equation. The profiles of heat flows also indicate that it is more likely that rapid temperature change can be caused under higher heating rates. On the other hand, with the lower heating rate, it implies that it is difficult to estimate the rate of decomposition only via the experimental observation of heat flow. Comparing heating rates of 5 K/min and 10 K/min, the peak of heat flow under 10 K/min heating rate (3.5 W/g) is approximately 2.3 times larger than that of 5 K/min (1.5 W/g). Similarly, the peak of the heat flow for 20 K/min (6.5 W/g) is approximately 1.8 times larger than that of 10 K/min (3.5 W/g). It can be seen that the peak of heat flow does not increase by the same fraction as the heating rate. Furthermore, the peaks of the heat flow of all heat rates lie on the point where the volume fraction of SEI reaches approximately at 0.35. It shows that approximately 65% of the SEI is decomposed when the heat flow hits the highest point.

Moreover, using the SEI formation and decomposition model and parameters discussed so far, we conducted simultaneous SEI decomposition and formation as described in our peer-reviewed journal paper [154]. Figure 4.13 shows a comparison between our DSC simulation and the experimental DSC result by Pasquier et al. [82]. At a temperature of approximately 400 K, both our simulation and Pasquier's experimental result show the peak of heat flow for SEI decomposition. The peak of heat flow is approximately 0.45 W/g which is 8 times smaller than that of Spotnitz et al. which is shown in Section 4.2.2. The SEI decomposition is clearly shown by the decreasing volume fraction of SEI, ϵ_{SEI}.
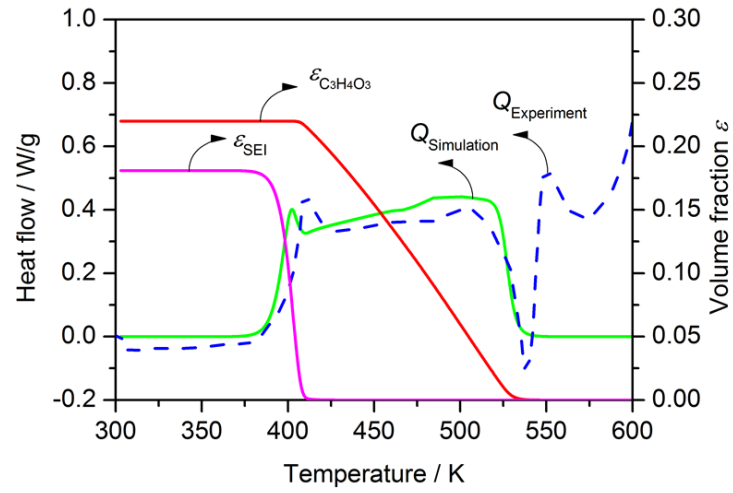
Figure 4.13: Heat flow and volume fraction while SEI formation and decomposition compared with DSC experimental results by Pasquier et al. [82; 153].
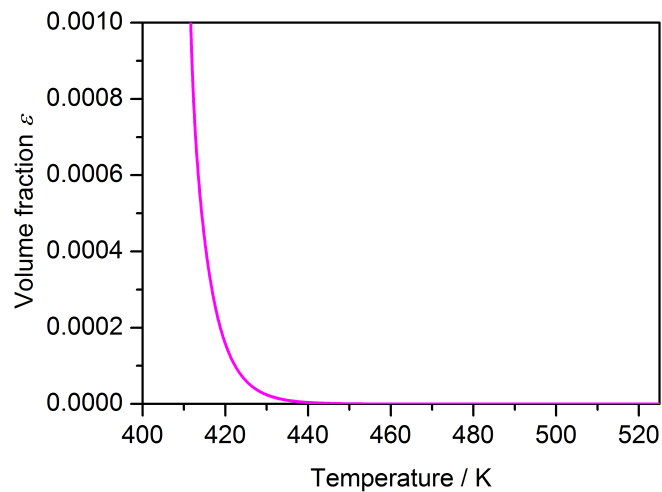
Figure 4.14: SEI volume fraction in a temperature range from 440 K to 470 K.

Between 400 K and 525 K, the heat flow plateau is considered to be the simultaneous SEI decomposition and formation as seen by decreasing ethylene carbonate due to SEI formation and a constant volume fraction of SEI (i.e., SEI decomposition and formation are in balance.). During the simultaneous SEI decomposition and formation, SEI volume fraction stays nearly zero as shown in Figure 4.14. The plateau region ends at 525 K where ethylene carbonate is completely consumed. When there is no ethylene carbonate left, SEI formation stops, and so is SEI decomposition. The endothermic heat flow that was experimentally observed at 540 K was attributed to the melting of $LiPF_6$ salt by Pasquier et al.. This phenomenon is not included in our simulation because it happens at a higher temperature than our target temperature range ($\sim$ approximately 523 K). Up to 525K, we successfully reproduce the heat flow of DSC experiment in same condition with only a model description of simultaneous SEI decomposition and formation.

4.3 Oxygen release from cathode material and solvent oxidation

4.3.1 Modeling and parametrization

In addition to models of SEI decomposition and formation on the anode side, we included a model of exothermic reactions on the cathode side for the blended cathode material. For the LFP cell, we did not include any exothermic reactions on the cathode side because it is already known that the olivine type of active material is stable even at elevated temperatures and oxygen evolution is rarely observed (see Section 2.4.2). The main exothermic reactions induced on the cathode side at elevated temperatures are oxygen evolution from a cathode active material and oxidation of solvent. At elevated temperatures, it is known that oxygen is released from a cathode active material because of structural instability and the released oxygen reacts with the solvent as already reviewed in Section 2.4.4. Also, it has been reported by Belharouak et al. that ethylene carbonate is the most reactive with oxygen through experiments [47]. The reaction of the ethylene carbonate with the released oxygen was assumed to produce carbon dioxide and water vapor (Figure 4.15) as reported by Belharouak et al..

Based on these arguments, we modeled a global reaction which is a combination of the oxygen release from the layered NCA cathode material and the oxidation of ethylene carbonate as following:

$$5 \, LiNCAO_2 + C_3H_4O_3 \rightarrow 5 \, LiNCAO + 3 \, CO_2 + 2 \, H_2O \tag{4.9}$$
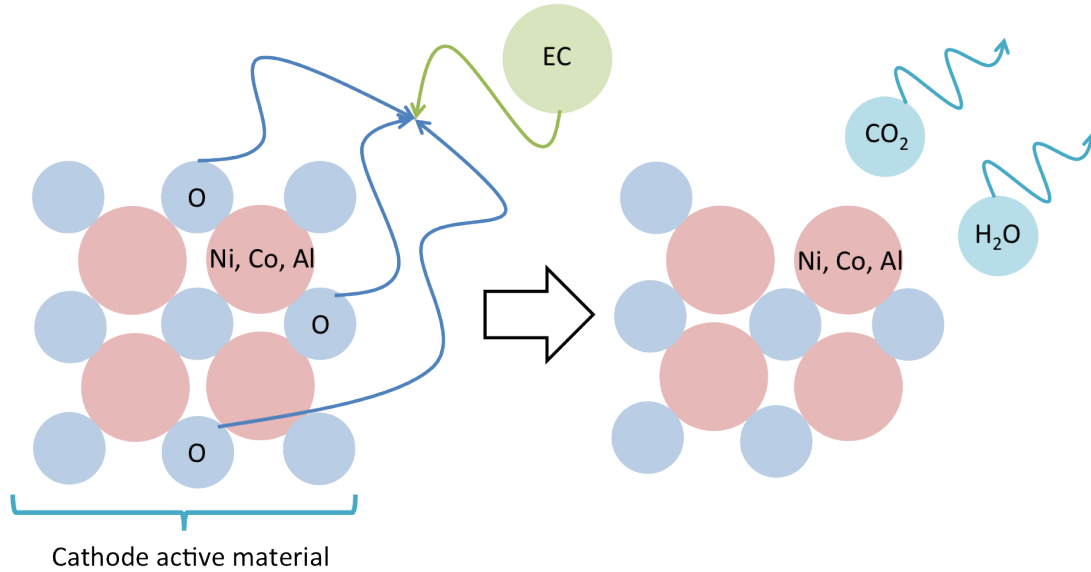
Figure 4.15: Schematic of oxygen release from cathode active material and oxidation of ethylene carbonate.

In this study, we considered only nickel cobalt aluminum oxide as a host of the oxygen release in the blended cathode material because it is known that the decomposition of LMO can be suppressed when it is blended with layered material as reviewed in Section 2.4.3.

The kinetic parameters for the reaction (Equation 4.9) are shown in Table 4.4. The parameters were obtained through fitting to the experimental DSC heat flow profile because there are no parameters available in literature.

Table 4.4: Kinetic parameters for the global reaction of oxygen release from cathode active material and oxidation of ethylene carbonate. These values were obtained through fitting with DSC experiment by Belharouak et al. [47].

Parameters	Unit	
Frequency factor	[m/s]	3.426×10^{12}
Activation energy	[J/mol]	2.80×10^5

The thermodynamic parameters of gaseous species were obtained from the NASA data [155]. As for the nickel cobalt aluminum oxide as a reactant (LiNCAO$_2$), we took the enthalpy of formation in SOC of 50% ($H_{\text{LiNCAO}_2} = -221$ kJ/mol). Note that the enthalpy is different from what is shown as enthalpies of lithium intercalation in Section 2.4.4. This is due to different references (i.e., the reference is standard state for H_{LiNCAO_2} in this section and, on the other hand, the reference in Section 2.4.4 is lithium metal for the enthalpies of lithium intercalation). As for the enthalpy of formation of the nickel cobalt aluminum oxide as a product (LiNCAO), we fitted the value to match the experimental

result by Belharouak et al. [47]. The value used in our work for $LiNi_{0.8}Co_{0.15}Al_{0.05}O$ is $H_{\mathrm{LiNCAO}} = -33.6$ kJ/mol. Details of the validation are shown in Section 4.3.2.

4.3.2 Results and discussion
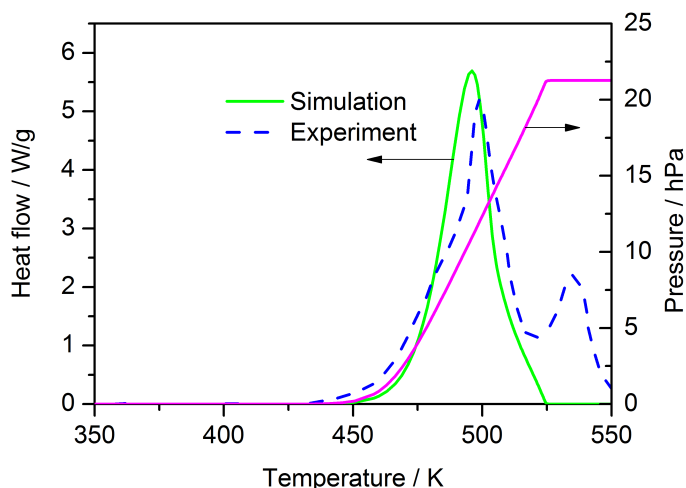
Figure 4.16: Profiles of heat flow and sum of partial pressures for released gases while oxygen release and solvent oxidation in NCA cathode material compared with DSC experimental results by Belharouak et al. [47; 137]. The heating rate is 10 K/min.

DSC simulations were conducted to obtain parameters which reproduce an exothermic behavior through oxygen evolution from NCA and oxidation of ethylene carbonate. In Figure 4.16, the simulation result is compared to the DSC experimental result by Belharouak et al.. The peak of the heat flow appearing approximately at 490 K is the target in this work as Belharouak et al. explains that this peak corresponds to the oxygen release from a cathode active material and solvent oxidation by investigations through XPS experiments. Parameters shown in Section 4.3.1 was used for the simulation. The heating rate is set as 10 K/min, which is the same condition as the DSC experiment conducted by Belharouak et al.. The initial temperatures were set at 303 K and was increased to 553 K in our simulation. In this simulation, volume specific active surface area was kept constant $(5.0 \times 10^7$ m^2/m$^3)$ because we assume that the reactions take place without correlating with a bulk thickness (i.e., volume fraction) such as the SEI. As shown in Figure 4.16, the simulation successfully reproduces the peak of heat flow in terms of width and height of the peak. The heat flow peak reach approximately 5.5 W/g that is nearly 14 times higher peak than that of SEI decomposition shown in Figure 4.13. This indicates that a combination of oxygen release from a cathode active material and solvent oxidation is highly exothermic, although an initiation temperature of this combination is 80 K higher than that of SEI decomposition. At the same time, sum of partial pressures for released gases

increases during the heat release. This represents that the gas production is successfully simulated in the model.

4.4 Ethylene oxidation and lithium hydration

4.4.1 Modeling and parametrization

In the previous sections, we constructed models of runaway reactions which are traceable by DSC experiments. In DSC experiments, a sample is placed in a relatively large space compared to the size of sample (i.e., open space), therefore produced gas can escape. In this section, to implement simulations of a whole battery, we studied chemical mechanisms which cannot be traced by DSC because battery components such as electrodes are in the closed environment of a battery can. As runaway chemistries in the closed systems, we included two reactions:(1) combustion of ethylene (Equation 4.10), and (2) hydration of lithium associated with H_2O produced from the ethylene combustion (Equation 4.11 (Figure 4.17). For combustion of ethylene, reactants are obtained through products of SEI decomposition. This reaction produces H_2O, which induces hydration of lithium on the cathode surface. The reaction between water and lithium is based on a hypothesis shown by Aurbach et al. [156]. Here, reactions in a closed system are also treated as global reactions similar to other reactions discussed in previous sections in this chapter.

$$C_2H_4 + 3\,O_2 \rightarrow 2\,CO_2 + 2\,H_2O \tag{4.10}$$

$$2\,H_2O + 2\,LiC_6 \rightarrow H_2 + 2\,LiOH + 2\,C_6 \tag{4.11}$$
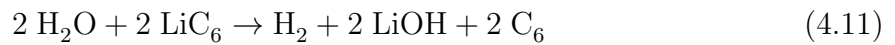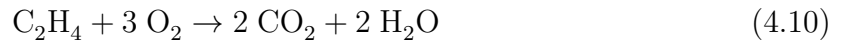
Reaction rates of these reactions are assumed to follow the Arrhenius equation and heat fluxes are derived by Equation 3.43 and 3.44. The thermodynamic properties of species except ethylene carbonate were obtained through the database of NASA polynomials for the both reactions. As for ethylene carbonate, we used the thermodynamic parameters shown in Section 3.5.5. The activation energy for the ethylene combustion is based on data by Guo et al. under the presence of a platinum catalyst whereas we used an estimated value for the frequency factor assuming that the reaction occurs with the almost same probability as SEI decomposition (Table 4.5) [157]. The kinetic parameters of hydration of lithium are based on parameters shown by Deal et al. (Table 4.6) [158]. The volume specific active surface area of SEI decomposition introduced in Section 4.2 is shared with both
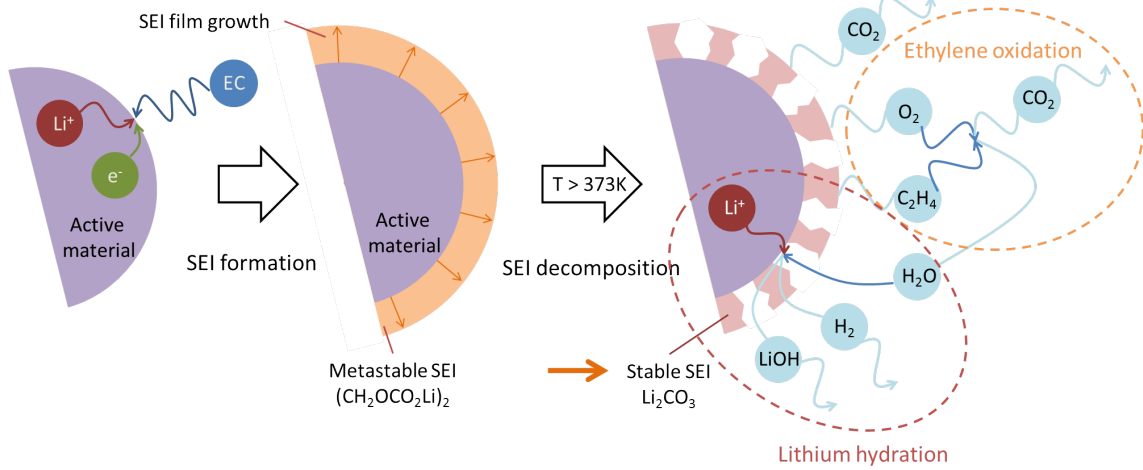
Figure 4.17: Schematic of reactions of gas products following after SEI formation and decomposition.

ethylene combustion and lithium hydration because these two reactions are associated with a SEI decomposition reaction.

Table 4.5: Kinetic parameters for a global reaction of ethylene oxidation. †: assumed, ‡: based on ref.[157].

Parameters	Unit	
Frequency factor	[m/s]	3.426×10^{26}†
Activation energy	[J/mol]	1.25×10^5‡

Table 4.6: Kinetic parameters for a global reaction reaction between lithium in active material and H_2O. The parameters are based on ref. [158].

Parameters	Unit	
Frequency factor	[m/s]	5.028×10^{-6}
Activation energy	[J/mol]	0.251×10^5

We conducted simulations in similar conditions to DSC of an anode assuming a small enough sample to have no temperature gradient inside and applying a constant heating rate (5 K/min) as reviewed in Section 3.6.3. The initial SEI volume fraction is 0.1 and the target was heated up from the initial temperature of 303 K. The results are discussed in Section 4.4.2.

4.4.2 Results and discussion

Figure 4.18 shows profiles of anode average/ambient temperatures and the SEI volume fraction of considering a constant heating rate of 5 K/min. We compared the cases between

with and without SEI formation reaction. In either case, sharp temperature peaks are observed when temperatures reach 380 K and above which is associated with decrease of the SEI volume fraction indicating decomposition of SEI. The temperature increases by the reactions are also identical in both cases and reach to 60 K.
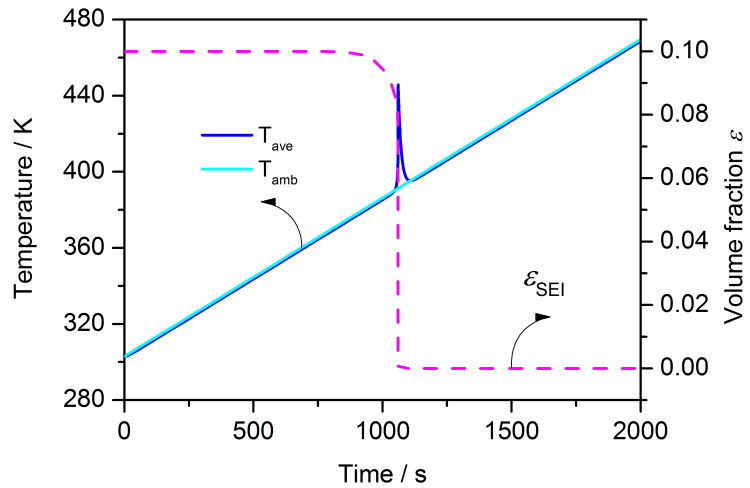
(a) Without SEI formation
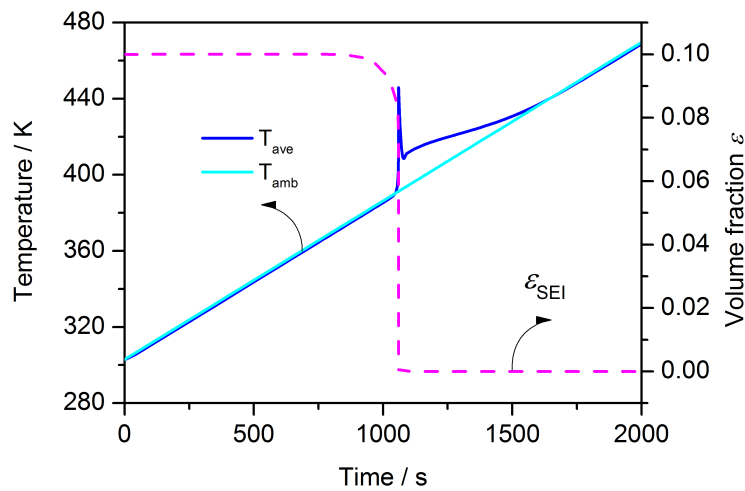
(b) With SEI formation

Figure 4.18: Profiles of cell average/ambient temperatures and heat flow from DSC simulation with/without SEI formation in addition to reactions associated with gas products from SEI decomposition.

The difference between with and without SEI formation appears after the temperature peak. With SEI formation, the anode temperature remains higher than the ambient temperature indicating simultaneous reactions of SEI decomposition and formation as well as the reactions by gas (Figure 4.18b). It lasts approximately 500 s and the anode temperature gradually merges with ambient temperature. On the other hand, without SEI formation, the anode temperature immediately reaches ambient temperature after the

peak. (4.18a). Therefore, it can be said that the peak is due to SEI decomposition and subsequent reactions involving the gaseous products. The sharp peak at 1100 s is dominated only by SEI decomposition and SEI formation contributes less to the temperature increase. This rapid temperature increase is associated with high heat flow by simultaneous reaction of ethylene oxidation and lithium hydration (Figure 4.19). The maximal heat flow reaches 2000 W/g, which is 400 times more than that of the cathode runaway chemistries. These results suggest that the peak temperature/heat flow also depend on the initial volume fraction of SEI because of the dependency on SEI decomposition as exhibited in Figure 4.8.
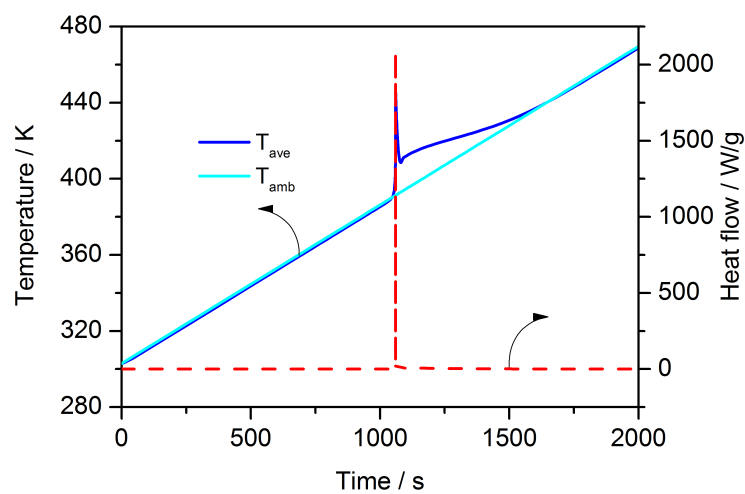
Figure 4.19: Profiles of heat flow and SEI volume fraction from DSC simulation with SEI formation in addition to reactions associated with gas products from SEI decomposition.

5 Results II: Battery simulations

This chapter presents the results from our full cell simulations. First, we calibrated the cell models with experiments implemented by our project partner, ZSW. The calibration has been conducted by comparing discharge/charge curves (Section 5.1). Thermal calculations of the battery model were verified in previous works [129; 135], therefore we only focused on the calibration of the discharge/charge curves. Utilizing the calibrated model, we investigated the behavior of runaway chemistries described in Chapter 4 and examined their influence on cell surface/average temperatures under thermal and electrical abuse (Section 5.2 and 5.3). In order to verify contributions on cell temperature increases from each reaction, we conducted simulations in various conditions (Table 5.1).

Under thermal abuse conditions, we examined how SEI and cathode runaway chemistries influence cell temperature behaviors in an LFP and a blended cell. Upon electrical abuse conditions, an external short circuit and heavy cycling were simulated in order to further investigate contributions to increased cell temperature that were not SEI and cathode runaway chemistries.

Table 5.1: Battery simulation conditions in this chapter. (a) SEI decomposition (b) SEI formation, (c) Oxygen release from cathode material and solvent oxidation, (d) Ethylene oxidation and lithium hydration.

Section	Battery	Condition	Runaway chemistries
5.2.1	LFP	Constant temperature	(a) and (b)
5.2.2	Blend	Constant temperature	(a), (b), and (c)
5.2.3	LFP	Temperature ramp	(a) and (b)
5.2.4	Blend	Temperature ramp	(a), (b), and (c)
5.3.1	LFP	External short circuit	(a) and (b)
5.3.2	Blend	Heavy cycling	(a), (b), (c), and (d)

5.1 Charge and discharge characteristics under nominal operating conditions

5.1.1 Batteries with LiFePO$_4$ cathode

The parameters for an LFP cell shown in Section 3.5 are verified by comparing charge and discharge curves against experiments conducted by the project partner, ZSW. Figures 5.1 and 5.2 present charge and discharge curves obtained through simulations and experiments, respectively. In both charge and discharge cases, we made comparisons of every combination in 0.1 C, 1 C, and 5 C at 298 K, 313 K and 333 K ambient temperatures. The cell used in the experiments is an ANR26650M1A type manufactured by A123 Systems, LLC. [159]. We did not conduct experiments over 333 K because of safety concerns to correctly investigate the characteristics under nominal operational conditions.

During our experiments, 2.6 V was used for the initial voltage. 3.6 V was used as the cut-off voltage for charge curves due to safety reasons given by the manufacturer. Once the cut-off voltage was reached, the voltage was kept constant. We applied the same cut-off condition in charging simulations. Under every temperature, 298 K, 313 K and 333 K, the charge curves in 0.1 C and 1 C exhibited almost perfect agreement between simulations and experiments, except at the end of charge when capacity was at approximately 2.3 Ah. At 0.1 C and 1 C, the simulations successfully reproduced the unique plateau of an LFP cell in a capacity range from approximately 0.2 Ah to 2 Ah. The charge curves with 5 C also reach the voltage plateau at the beginning of a charge by a capacity of approximately 1 Ah. However, the charge curves exhibit differences between the simulation and experiment at a capacity approximately 1 Ah and above. These differences at 5 C can be considered to be attributed to the kinetic effect because these are not observed at 0.1 C and 1 C where thermodynamic effect is dominant compared to kinetic effect [129].

The discharge curves show a similar tendency to charge curves for 0.1 C and 1 C: good agreement by capacity of approximately 2.2 Ah. This discrepancy in higher C-rates can be explained by the kinetic effect, similar to the discussion on charge curves. Under 5 C, the discharge curves show that the plateau region has better agreement at higher temperatures even though there are differences at the end of discharge associated with a rapid decrease in cell voltage.
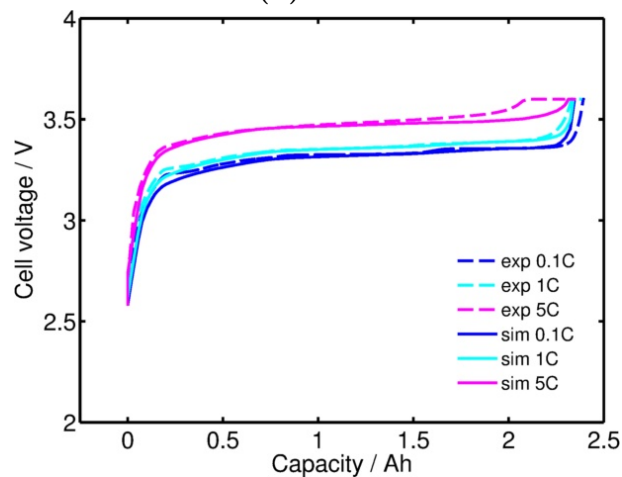
Although there are discrepancies between simulations and experiments at the end of charge/discharge, it can be said that the parameters shown in Section 3.5 are practical enough in a capacity range between 0 Ah to approximately 2.2 Ah for 0.1 C and 1
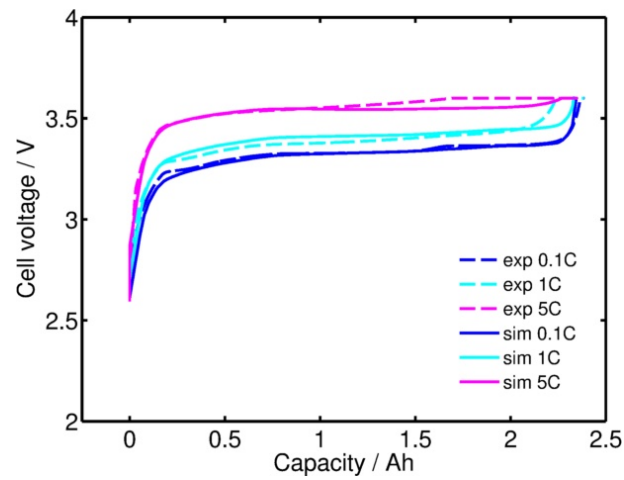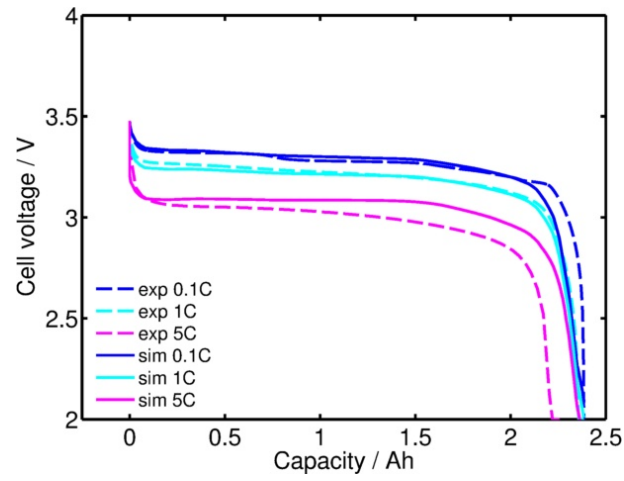
(a) 298K.
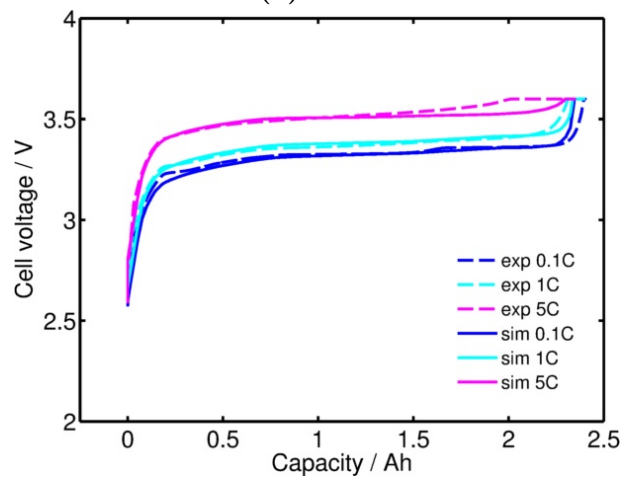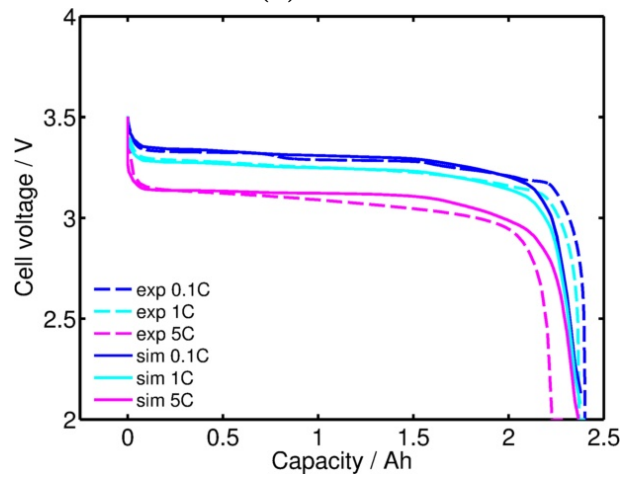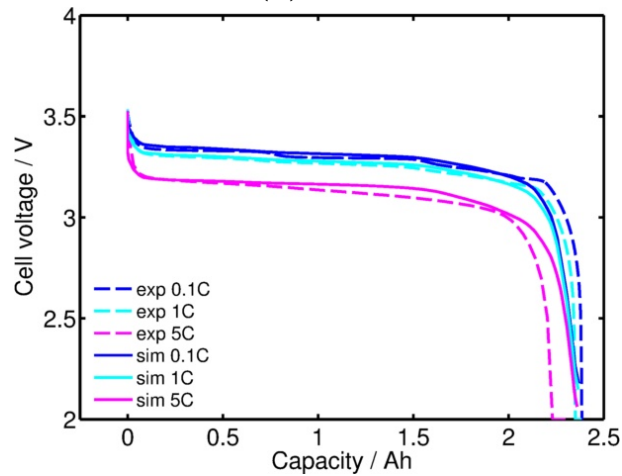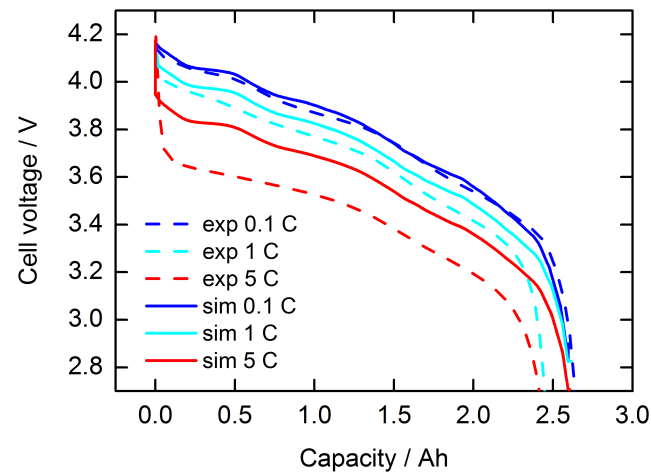

(b) 313K.

(c) 333 K

Figure 5.1: Comparison of charge curves under nominal operation condition of a cell with an LFP cathode between our simulation and experiments conducted by ZSW.

(a) 298 K

(b) 313K.

(c) 333 K

Figure 5.2: Comparison of discharge curves under nominal operation condition of a cell with an LFP cathode between our simulation and experiments conducted by ZSW.

C. Also, even with a higher C-rate such as 5 C, the comparison between simulations and experiments show these parameters are practical at higher temperatures.

5.1.2 Batteries with blended cathode

In addition to investing a cell with an LFP cathode, we also investigated the characteristics of nominal operating conditions for a cell with an NCA/LMO blended cathode. Similar to the LFP cell mentioned in Section 5.1.1, we compared simulation results with experimental data obtained by ZSW. The cells used in the experiments are a SE US26650VT type cell manufactured by the Sony Corporation. Figure 5.3 shows a comparison of discharge curves between simulations and experiments for a cell with the blended cathode. Both simulations and experiments are conducted in every combination under 0.1 C, 1 C, 5 C and 10 C at 298 K, 313 K and 333 K ambient temperatures. Only discharge curves are examined in this section because discharge curves provide all basic information such as a cell voltage dependency on capacity. Furthermore, the charging cut-off voltage allows investigations in a full capacity range only at low C-rates, as seen in the charge curves of an LFP cell in previous section. The kinetic parameters shown in Section 3.5.2 were also used in these discharging simulations.

Different from an LFP cell, which has a plateau in its voltage profile, a blended cell exhibits voltage steps while discharging. As discussed in Chapter 2, these steps are due to the crystal structure changes upon discharge in a spinel cathode lithium intercalation/extraction according to lithium concentration and a cycling number. In 0.1 C, the simulations successfully reproduced the first step which appears at a capacity of 0.5 Ah. The second and the third steps are also reproduced by simulations, however, these are slightly shifted to lower capacity compared to the experiments. Similar to the simulation characteristics of the LFP cell shown in Section 5.1.1, simulations have better agreements with experiments at higher ambient temperatures. Discrepancies between experiments and simulations occur under 5 C for every ambient temperature in a full capacity range. Voltage difference between experiments and simulations is 0.2 V in the 298 K case and it reduces to 0.1 V in the 333 K case. These discrepancies are considered to be due to kinetic effects, because thermodynamics are dominant at lower C-rates. However, these voltage differences between simulations and experiments are less than 10%, therefore we assume that the simulations hold qualitative validity. In Section 5.3, we discuss abuse based on cell cycling with the same model used in this section.

(a) 298 K
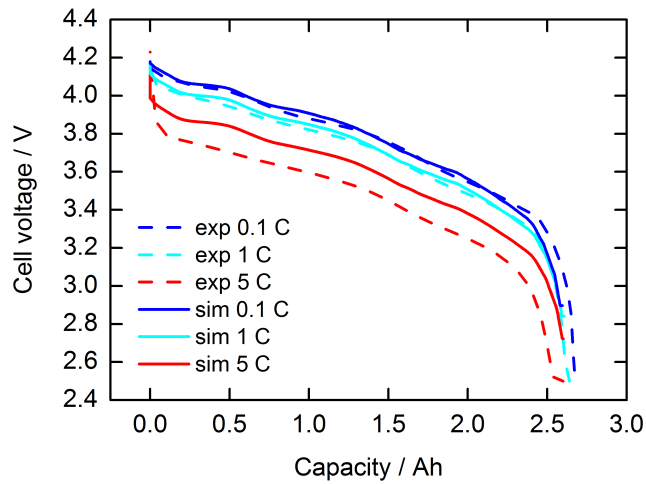
(b) 313 K
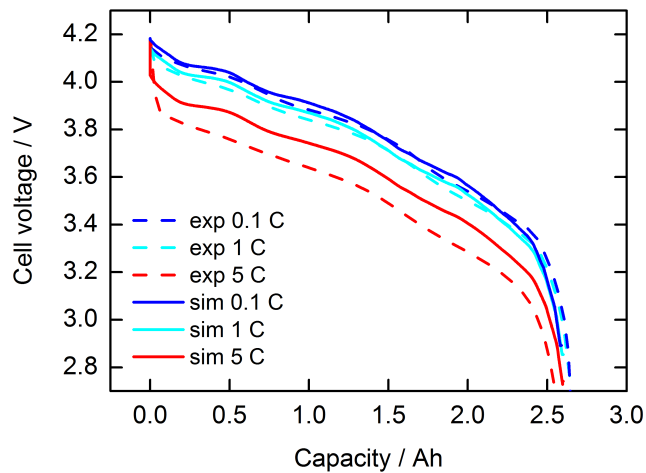
(c) 333 K

Figure 5.3: Comparison of discharge curves under nominal operation condition of a cell with blend cathode between our simulation and experiments conducted by ZSW.

5.2 Thermal abuse

### 5.2.1 Constant elevated ambient temperature with an LiFePO$_4$ cathode battery

In this section, we explain numerical experiments conducted for an LFP cell under constant elevated ambient temperatures. Note that Chapter 4 explains runaway chemistries associated with each electrode inside of a cell, but in Chapter 5, we discuss the thermal behavior of an entire cell in which the runaway chemistries of the electrodes are coupled with an electrochemical cell model.

Based on the olivine material characteristics explained in Section 2.4.2, we made the assumption that an LFP cathode does not decompose, hence oxygen evolution does not occur. Therefore, we only included SEI decomposition and formation as runaway chemistries (Section 4.1) for an LFP cell and investigated how those two reactions influence average cell temperatures at constant elevated ambient temperatures. We examined these reactions in the LFP cell in an ambient temperature range between 353 K and 433 K with SOC at 100% under an open circuit condition (i.e., zero current density). The initial temperatures of a cell were defined in the same value as ambient temperatures. The initial SEI volume fraction was set to 0.18, based on the realistic range of the SEI volume fraction discussed in Section 4.1.1. Here, we assumed a used cell to realize high heat flow from SEI. As for other parameters, we utilized the parameters shown in Section 3.5. Figure 5.4 shows profiles of average cell temperatures and volume fractions of ethylene carbonate and SEI at 373 K and 400 K ambient temperatures.

Under a 373 K ambient temperature (Figure 5.4a), SEI decomposition starts from the beginning (0 h) because the initial cell temperature, 373 K, is over the onset temperature of SEI decomposition reaction. The average cell temperature has a unique kink at 0.2 h which corresponds to the initiation of an SEI formation reaction in addition to SEI decomposition indicated by decreasing volume fraction of ethylene carbonate. In a range of 10 h to 22 h, the plot of volume fraction shows a plateau until the volume fraction of ethylene carbonate reaches zero. This plateau can be explained as a simultaneous reaction of SEI decomposition and formation. The highest average cell temperature is $T = 373.8$ K at 11 h which results from the simultaneous reaction of SEI decomposition and formation. Maximum cell temperature exceeds average cell temperature only around the plateau region, between approximately 8 h and 23 h, indicating that these exothermic reactions happen actively. After all of the ethylene carbonate is consumed at 25 h, the rest of the SEI starts decomposing. The decomposition takes approximately 25 h to complete. Under a 373 K ambient temperature, these results show that overall phenomena proceeds
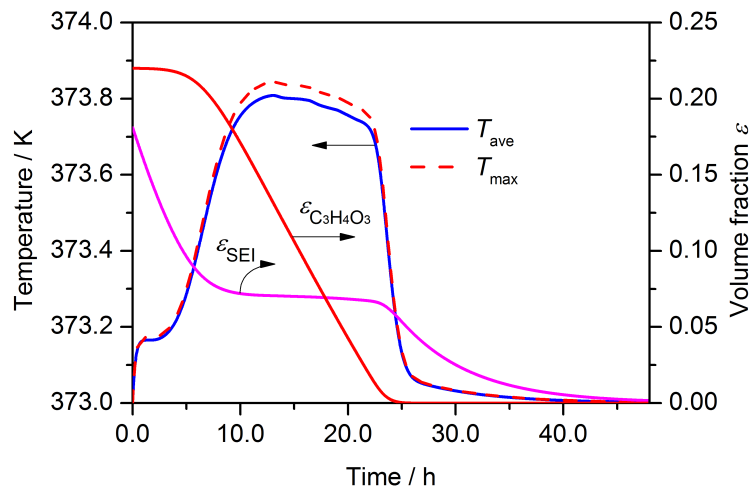
(a) LFP, constant ambient temperature 373 K
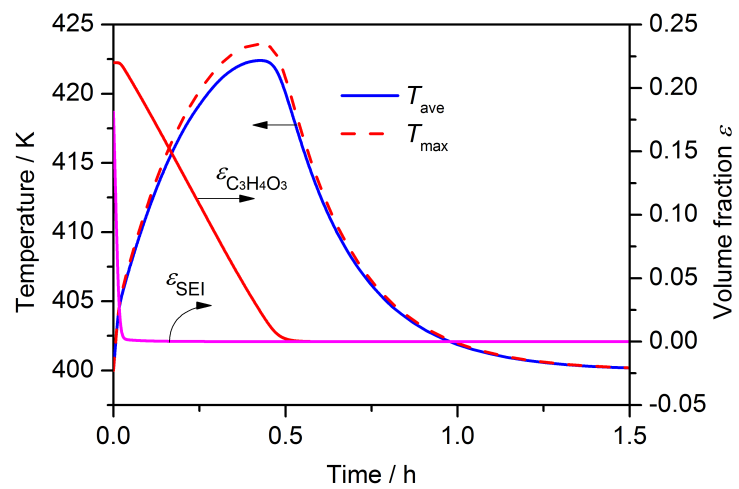
(b) LFP, constant ambient temperature 400 K

Figure 5.4: Profiles of average cell temperature and volume fraction of SEI and ethylene car-
bonate for an LFP cathode cell at 373 K and 400 K constant ambient temperatures
[153].

very slowly, taking 100 h with the maximum temperature increase not being prominent (i.e., maximum 1 K increase).

On the other hand, under a 400 K ambient temperature (Figure 5.4b), the consumption time of ethylene carbonate is five times faster than that of a 373 K ambient temperature. At the same time, SEI is also consumed more rapidly than that under a 373 K ambient temperature. Moreover, similar to the case discussed in Figure 4.14, SEI volume fraction over zero is not observed in the 400 K case even though the plot in the 373 K case shows the plateau at 0.07 from 10 h to 22 h. Although SEI volume fraction stays nearly zero in a range from 0.0 h to 0.49 h, we can see that the simultaneous reaction of SEI decomposition and formation still occurs because it takes more time to consume ethylene carbonate (0.5 h) than SEI (0.1 h), indicating SEI continues forming up to 0.5 h. Furthermore, the large increase of average cell temperature in a time range from 0.0 h to 0.49 h also suggests the occurrence of a simultaneous reaction. Similar to the 373 K case, maximum cell temperature exceeds average cell temperature in a time range between 0.25 h and 0.5 h while simultaneous SEI decomposition and formation occurs. Here, SEI is decomposed right after it is formed. The consumption of ethylene carbonate is 48 times faster than that in the 373 K case due to higher reaction rates associated with a higher cell temperature. The maximum cell temperature reaches 423 K by 0.49 h, 23 K higher than the initial cell temperature. This temperature increase is more than 20 times higher than that in the 373 K case because of higher reaction rates for both SEI decomposition and formation. Although the temperature rise (23 K) is prominent, the temperature plot does not show an exponential increase. Thus, it can be said that self accelerating heating (i.e., thermal runaway) is not observed even at an elevated temperature of 400 K.

These results indicate that it is unlikely for the LFP cell to suffer thermal runaway only from simultaneous SEI reactions, even at an elevated temperature, unless there are additional triggers like short circuits. However, a cell can be damaged by consumption of electrolyte associated with the simultaneous reactions (i.e., fast aging of a cell).

5.2.2 Constant elevated ambient temperature with a blended cathode battery

In this section, the thermal behavior of a cell with a blended cathode (NCA/LMO) is examined at constant elevated ambient temperatures. In contrast to the LFP cell explained in Section 5.2.1, for a cell with the blended cathode, we introduced the model of oxygen release from cathode material and solvent oxidation (Section 4.3), in addition to SEI decomposition and formation based on arguments about oxygen evolution (Section 2.4.5).

In this model, SEI volume fraction was defined as 0.18, which is the same value mentioned in previous section. We examined an ambient temperature range from 483 K to 443 K in 100% SOC under open-circuit conditions (i.e., zero current density). This ambient temperature range is higher than that in an LFP cell because the onset temperature is higher for oxygen evolution from cathode material and solvent oxidation, and because we did not observe differences in heat flow and average cell temperature between 373 K and 443 K. Similar to the LFP cell conditions shown in Section 5.2.1, the initial temperature of the blended cell was defined in the same value as ambient temperatures. As for other blended cell parameters, we utilized the values shown in Section 3.5.
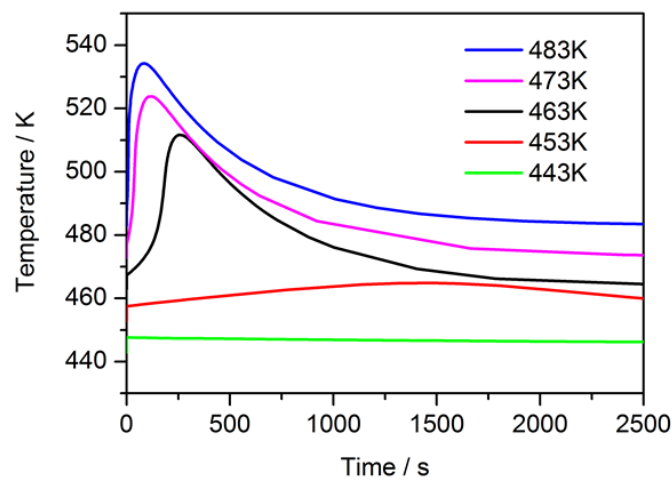
Figure 5.5: Average cell temperature profiles for a blended cell under various constant ambient temperatures.
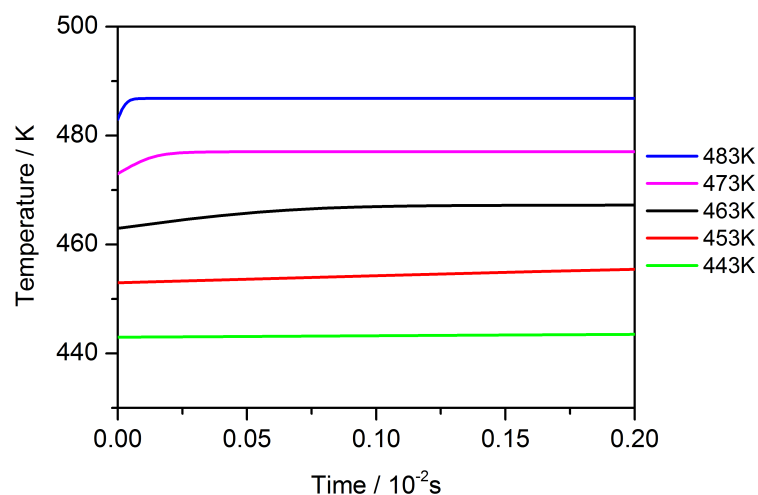
Figure 5.6: Average cell temperature profiles in a time range from 0 to 0.002 s for a blend cell under various constant ambient temperatures.

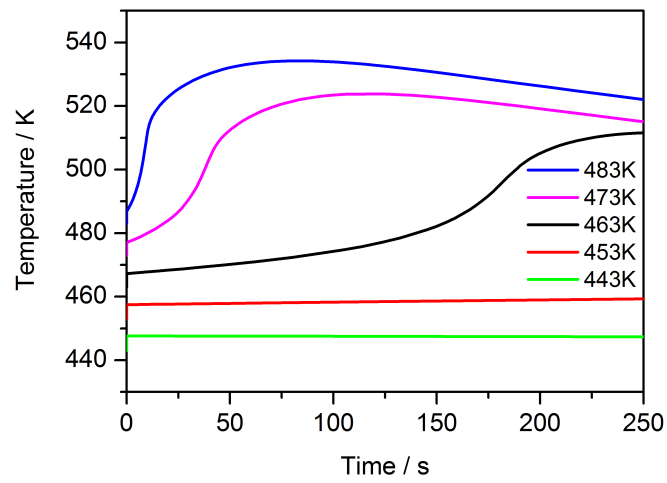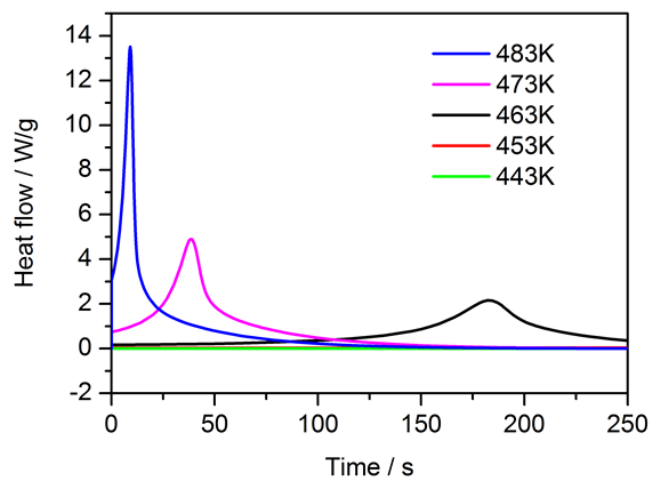Figure 5.5 shows profiles of average cell temperatures under various constant ambient tem-
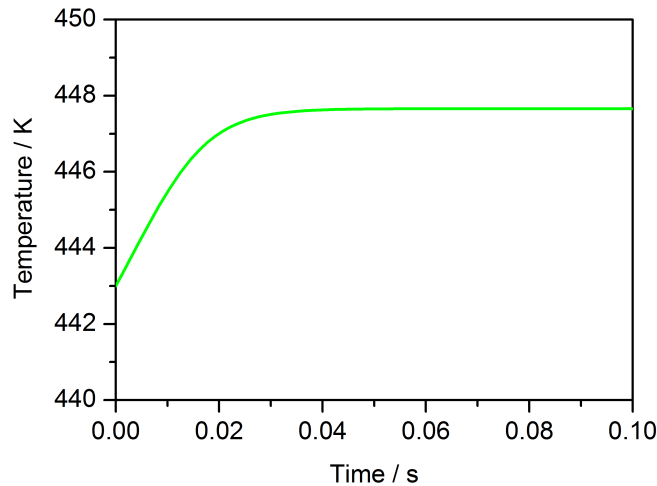
Figure 5.7: Average cell temperature profiles in a time range from 0 to 0.1 s for a blend cell under 443 K ambient temperature.

peratures. Due to its high initial temperatures, the SEI-related reactions are completed in one second. This can be seen in Figure 5.6, which shows average cell temperature profiles in a time range from 0 s to 0.002 s. In the 483 K case, temperature step shows that the SEI-related reactions are completed in 0.0001 s. At lower temperatures, the reaction rates are smaller, therefore the reaction completion time takes longer. In the 433 K case (Figure 5.7), it takes approximately 0.03 s to complete a temperature increase of 5 K. Moreover, any temperature rises are not observed after the SEI decomposition and formation reactions. On the other hand, at 453 K, moderate temperature increase of less than 5 K over 1500 s is observed. Rising temperature from cathode runaway chemistry becomes more prominent between 453 K and 463 K in an ambient temperature, and temperature peaks are observed between 0 s and 500 s. The average cell temperatures exponentially increases indicating that the heating rate from cathode runaway chemistries overcomes the cooling rate by natural convection at the cell surface. The maximum temperature rise is around 40 K under an ambient temperature between 463 K and 483 K. Compared to this temperature increase from cathode runaway chemistries, we can see that anode runaway chemistries (i.e., SEI decomposition and formation) have a low impact on overall temperature.

Heat flow profiles are shown in Figure 5.8b in an ambient temperature range from 443 K to 483 K in 0 s ∼ 250 s. Under 443 K and 453 K ambient temperatures, heat flows stay at nearly zero even though heat flow peaks are clearly seen (over 2 W/g) under other ambient temperatures. The average cell temperature peak in the 463 K ambient temperature case is wider but lower than those of higher ambient temperatures. The maximum heat flow under 463 K ambient temperature is approximately 6.5 times smaller

(a) Temperature profile


(b) Heat flow profile

Figure 5.8: Average cell temperature and heat flow profiles in a time range from 0 s to 250 s for a cell with blend cathode under various constant ambient temperatures.

than that of 483 K. This suggests that the heating rate is smaller but the heating time is longer at lower ambient temperatures and that a 10 K difference in ambient temperature has a large impact on the heating rate of cathode runaway chemistries. At 0 sec, higher ambient temperatures show a higher heat flow. It can be considered that this is also due to cathode runaway chemistries. This is because the heat flow of SEI decomposition and formation is less than 0.5 W/g from the DSC graph shown in Figure 4.13. Therefore, it can be considered that the contribution from anode runaway chemistries on total heat flow is small. Hence, it is unlikely that SEI decomposition and formation directly induce cathode runaway chemistry due to its low heat release rate when the volume fraction of SEI is less than 0.18.
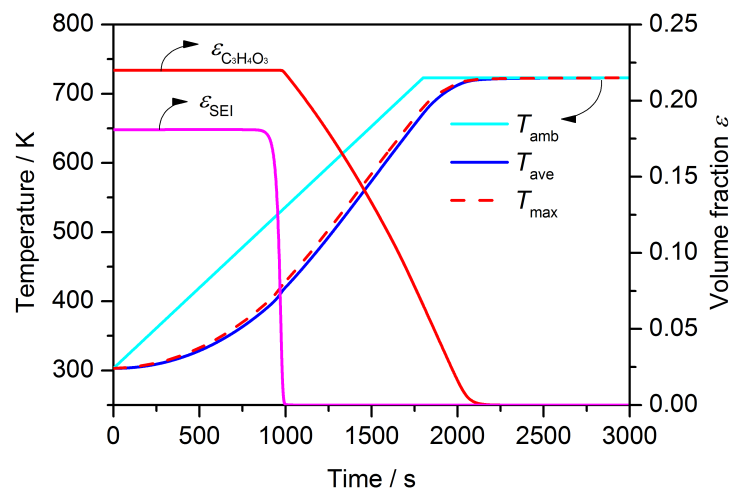
5.2.3 Ambient temperature ramp with an LiFePO$_4$ cathode battery

In order to investigate how ambient temperature ramps influence cell thermal behavior, we applied various constant heating rates to ambient temperature and examined the behavior of average cell temperature and volume fractions of ethylene carbonate and SEI. In this section, we examine a cell with an LFP cathode, therefore our model only includes SEI decomposition and formation as runaway chemistries based on characteristics of a cell as discussed in Chapter 2. The initial condition and parameters of a cell including SEI volume fraction are same as those under constant ambient temperature (Section 5.2.1). We tested heating rates in a range of 0.1 K/min to 15 K/min under an open-circuit condition (i.e., zero current density). Similar to the conditions in previous sections, heating rates were only applied to ambient temperature and a cell was heated by heat transfer at the surface and inside of a cell, accordingly. The initial cell and ambient temperatures were 303 K and ambient temperature was heated to 733 K.

Figure 5.9a shows profiles of average cell temperature, ambient temperature, and volume fractions of ethylene carbonate and SEI under a 0.1 K/min heating rate. The ambient temperature shows a linear increase from a constant heating rate and average cell temperature follows. At approximately 5.3 h, average cell temperature exceeds ambient temperature when average cell temperature reaches 380 K, and the temperature peak reaches approximately 420 K at 5.8 h. From the volume fraction of SEI, we can see that the decomposition of SEI already starts at approximately 3.5 h when average cell temperature reaches 360 K. However, average cell temperature does not overcome ambient temperature until SEI formation starts at 5.5 h. The SEI formation can be identified by decreasing the volume fraction of ethylene carbonate. This is similar to what was observed in the constant temperature case in Section 5.2.1. Although the volume fraction
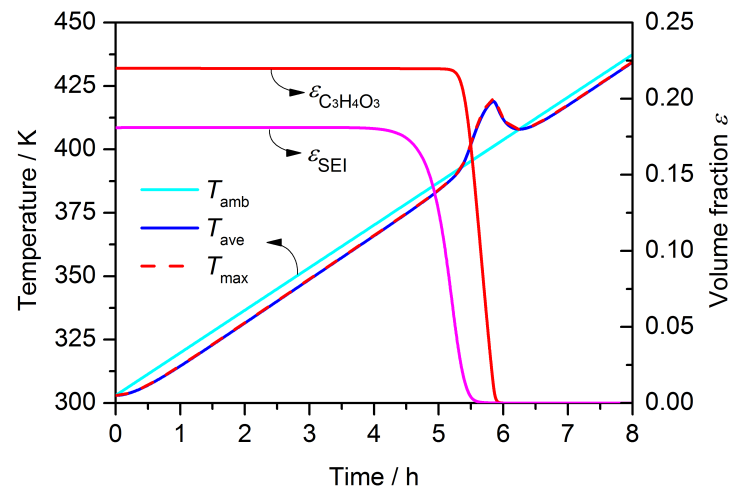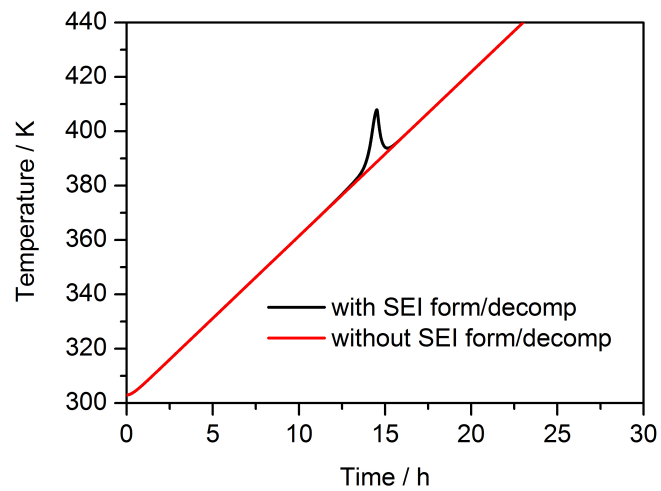
(a) Heating rate 0.1K/min

(b) Heating rate 15K/min

Figure 5.9: Average cell temperature profile of LFP cell under ambient temperature ramp with heating rate of 0.1 and 15 K/min [153].

of SEI stays at nearly zero during SEI formation between 5.5 h and 6.0 h, it can be considered that the simultaneous reaction of SEI decomposition and formation occurs in that time range due to the temperature peak. This is because a temperature peak cannot be achieved only by SEI formation, where heat flow is several magnitude smaller than that of SEI decomposition shown in Section 4.1. It takes almost 2 hours until all reactions complete from the point where SEI decomposition starts.

On the other hand, under a 15 K/min heating rate (Figure 5.9b), a average cell temperature peak does not appear (i.e., average cell temperature does not exceed ambient temperature). In this case, the heating rate of ambient temperature is rapid enough to hide the temperature rise of average cell temperature. The average cell temperature does not exceed ambient temperature even with approximately four times more rapid simultaneous reaction (i.e., higher heat flow) than that of the lower heating rate explained above. Meanwhile, the decrease in the reaction completion time is not proportional to the increase in heating rate. The heating rate is 150 times more with 15 K/min compared to 0.1 K/min, however, the completion time is only four times faster in the former case (i.e., 15 K/min). This can be also seen from slopes of the EC volume fraction relative to the SEI volume fraction in each heating rate. This is because the simultaneous reaction of SEI decomposition and formation is accelerated by its self-heating effect at a lower heating rate associated with the peak of temperature. Therefore, the heating rate of average cell temperature is forced to change at a faster pace than the original heating rate applied on ambient temperature. On the other hand, the relative temperature increase rate of average cell temperature against ambient temperature is moderate (i.e., without peak) under a faster heating rate. The onset temperature of SEI decomposition is observed at approximately 360 K and is the same in the 0.1 K/min case, however, the decomposition rate is more than 50 times faster (i.e., complete in 100 s) in the 15 K/min case.

In order to examine the influence of simultaneous SEI formation and decomposition on the average cell temperature, we compared average cell temperatures with and without the simultaneous reaction. Figure 5.10a shows temperature profiles with a heating rate of 0.01 K/min. Due to a low heating rate, the average cell temperature follows the ambient temperature without delay. The profile of average cell temperature with SEI decomposition and formation shows a peak similar to that of 0.1 K/min mentioned above. In contrast, without the reactions, we see a clear difference from the one with a reaction. The average cell temperature only follows ambient temperature and increases linearly. However, under a heating rate of 15 K/min, the difference with and without the reactions is more subtle compared to the lower heating rate shown in Figure 5.10b. These results indicate that heating rates on ambient temperature largely influence the behavior of average cell temperature. Under the higher heating rate, there is a possibility that we miss a signal

(a) Heating rate 0.01 K/min
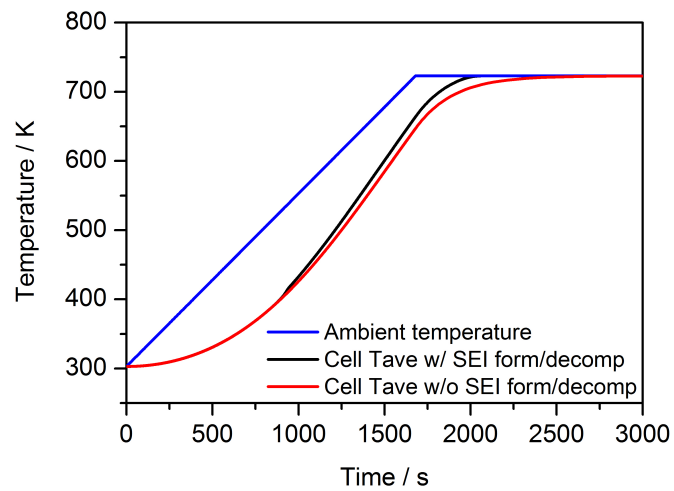
(b) Heating rate 15 K/min

Figure 5.10: Comparison of average cell temperature profile of LFP cell between with and without SEI formation/decomposition under temperature ramp in heating rate of 0.1 and 15 K/min.

of degradation inside of a cell if we only measure temperature of a cell.

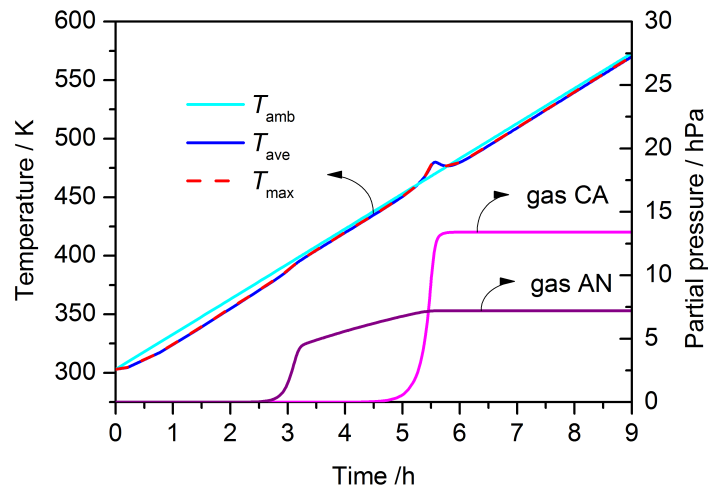### 5.2.4 Ambient temperature ramp with a blended cathode battery

In addition to an LFP cell, we examined the behavior of average cell temperature with a blended cell. The conditions and parameters of the cell are same as those discussed in Section 5.2.2. SEI volume fraction is set to 0.18. The runaway chemistries include oxygen evolution from cathode and solvent oxidation, in addition to SEI decomposition and formation. Similar to the conditions in Section 5.2.3, we applied heating rates in a range from 0.1 K/min to 5 K/min on an ambient temperature under an open-circuit condition (i.e., zero current density). In this section, we investigate the sum of released gas partial pressure by exothermic runaway chemistries in each electrode in order to examine how much these reactions happen. Here, we assumed the gaseous products escape to an open space inside of a battery can. The open space volume was estimated as 4.5×10^{-6} m^3.

Upon a 0.1 K/min heating rate (Figure 5.11a), average cell temperature keeps the same value as ambient temperature, although we can see that reactions develop in the both anode and cathode from increased gas pressure. Total partial pressure from anode runaway chemistries starts increasing at 12.5 h and cathode pressure increase follows at 22.5 h. Due to the low heating rate, ambient and average cell temperatures stay at the temperature where only SEI decomposition and formation happen for relatively long time. For this reason, large amounts of ethylene carbonate are consumed by SEI formation before reaching the onset temperature of cathode runaway chemistries where ethylene carbonate is also a reactant. Under 0.1 K/min, the amount of gas released by cathode runaway chemistries is smaller than those in higher heating rates. This indicates that cathode runaway reactions (i.e., oxidation of electrolyte) occur less frequently at lower heating rates. Under lower heating rates, ethylene carbonate is consumed more by anode runaway chemistries, resulting in less oxidation of ethylene carbonate on the cathode side. Maximal cell temperature stays at the same value as average cell temperature.
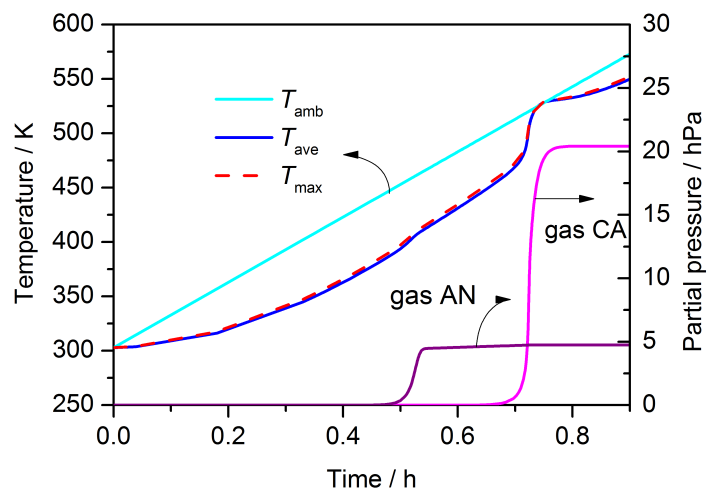
Figure 5.11b shows profiles of temperature and the total partial pressure under a 0.5 K/min heating rate. In contrast to the temperature profiles in the 0.1 K/min case (Figure 5.11a), average cell temperature shows a peak which exceeds ambient temperature, although maximal cell temperature stays at the same value as average cell temperature. The peak is associated with an increase of partial pressure from cathode runaway chemistries and indicates the occurrence of chemical reactions on the cathode side at a time range from
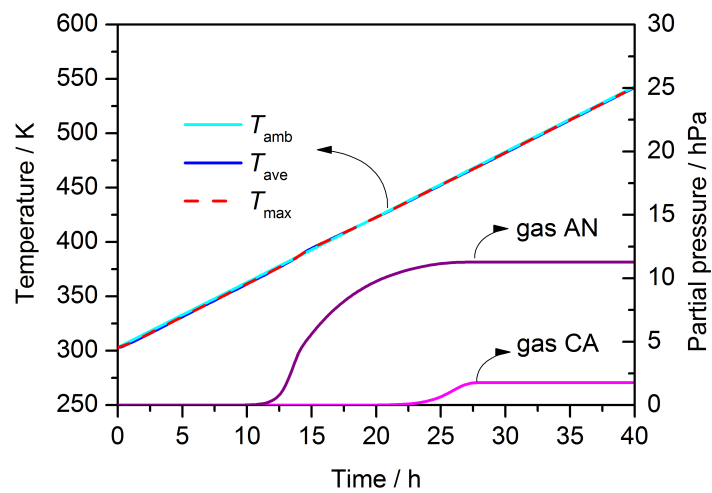
(a) Heating rate 0.1 K/min

(b) Heating rate 0.5 K/min
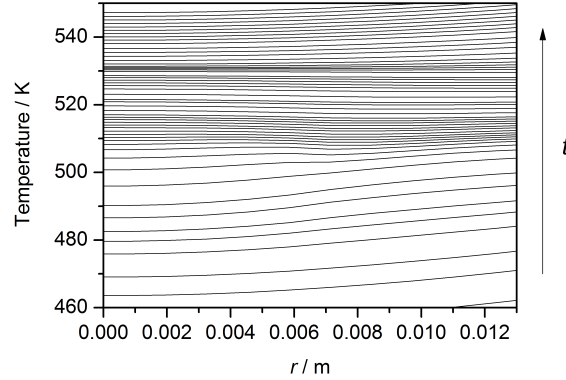

(c) Heating rate 5 K/min

Figure 5.11: Profiles of average cell temperature and total partial pressures for released gas by runaway chemistries in each electrode of the blended cell under ambient temperature ramp in 0.1, 0.5 and 5 K/min heating rate.

approximately 4.8 h to 5.5 h. Gas release from cathode runaway chemistries is approximately 6 hPa more than that in the anode side. In comparison to the lower heating rate shown in Figure 5.11a, we see that cathode runaway chemistries under 0.5 K/min release six times more gas than that under a heating rate of 0.1 K/min. On the other hand, a reaction in the anode ocurring under 0.5 K/min is 40% less than that under 0.1 K/min from the anode's gas release. This suggests that the amount of ethylene carbonate consumption by anode runaway chemistries is 40% less than that in the 0.5 K/min case. Therefore, it can be seen that more cathode reactions occur at higher heating rates because ethylene carbonate could remain longer at the onset temperature of cathode runaway chemistries. The consumption of ethylene carbonate from anode runaway chemistries is limited compared to the lower heating rates because the heating rate is fast enough to reach to the onset temperature of cathode runaway chemistries.

Figure 5.11c presents profiles under a 5 K/min heating rate. Due to the higher heating rate, average cell temperature shows longer delays in temperature rise from ambient temperature compared to lower heating rates. Similar to the case under a 0.5 K/min heating rate, we can observe a peak starting at 0.7 h when average cell temperature reaches approximately 460 K. When looking at the total partial pressure profiles, we can see that the peak is associated with cathode runaway chemistries. Compared to lower heating rates, the total partial pressure on the anode side is > 5 hPa less and, on the other hand, the total partial pressure on the cathode side is > 10 hPa more than those under 5 K/min. This suggests that the reaction in the anode occurs even less often due to same reason described above, i.e., average cell temperature reaches the onset temperature of cathode runaway chemistries even faster under a higher heating rate. The temperature rise caused by anode runaway chemistries (i.e., SEI decomposition and formation) seen at 0.5 h is very subtle in contrast to the temperature increase from cathode runaway chemistires which is nearly 50 K observed at 0.7 h. Even with the double temperature increase compared to the 0.5 K/min heating rate, average cell temperature does not exceed ambient temperature due to a sufficiently high heating rate. Compared to a lower heating rate, in a time range between 0.15 s and 0.7 s, maximal cell temperature is slightly higher than average cell temperature due to a greater temperature difference between the cell center and the cell surface.

In these results, the difference between the degradation process and the heating rate indicates that the degradation phenomena can be highly influenced by the history of heating a cell if a cell is exposed to several heating conditions. Furthermore, the maximum pressure rise observed is less than 21 hPa on the cathode side under a 5 K/min heating rate. This small increase in pressure shows that in order to reproduce a high-pressure rupture in the cell, it is necessary to extend a battery model by other battery failure
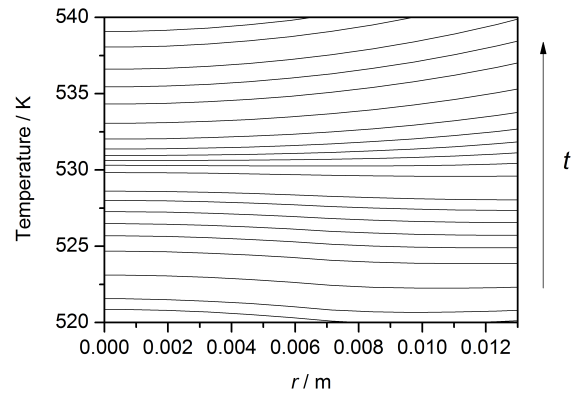
mechanisms such as electrolyte evaporation other than ethylene carbonate (e.g., DMC) or the expansion of gas which was originally inserted in the battery can.

(a) 460K - 550 K
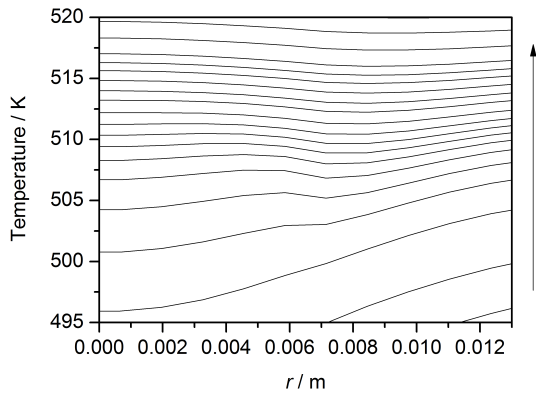
(b) 495 K - 520 K

(c) 520 K - 540 K

Figure 5.12: Temporal cell average/maximum temperature distributions along the cell radial direction (Cell center: $r = 0$) under 5 K/min heating rate. Time ranges in Figure 5.11c correspond to approximately: (a) 0.68 h - 0.9 h, (b) 0.72 h - 0.73 h, and (c) 0.73 h - 0.85 h.

Figure 5.12 shows temperature profiles along the cell radial direction under a 5 K/min heating rate. Each solid line in this figure represents a temperature profile at a certain time. We see that the temperature throughout the cell constantly increases as time advances. A temperature range from 460 K to 550 K corresponds to where the average cell temperature peak is observed in Figure 5.11c. In Figure 5.12a, below 500 K, we can see that the cell surface temperature is higher than that of the cell center due to a the high ambient temperature which is heated by constant a heating rate. However, temperature profiles become homogeneous throughout cell radial direction in a temperature range between approximately 500 K and 530 K.

Figure 5.12b shows a zoomed in view of temperatures between 495 K and 520 K. When

the cell center temperature is 495.5 K, the cell surface temperature is approximately 6 K higher than that at the center and the temperature distribution draw a continuous line without any kinks. However, between 500 K and 510 K, at approximately 0.0055 m and 0.007 from the cell center, we can see that the temperature distribution lines become more wavy due to cathode runaway chemistries. Then, at 515 K and above, the temperature distribution becomes smoother when the cell center temperature exceeds the cell surface temperature. These temperature distribution changes were caused by cathode runaway chemistries as reviewed in Figure 5.11c.

Figure 5.12c shows a zoomed in view of temperatures between 520 K and 540 K. The homogeneous temperature distribution shown in this figure is associated with the diminishing reaction of cathode runaway chemistries between 527 K and 530 K. Over 530 K, temperature distribution is restored to its former state (i.e., cell surface temperature exceeds the cell center temperature). There is no irregular distribution kinks observed during this time.

On the other hand, under a 0.5 K/min heating rate (Figure 5.13), temperature distribution changes are smaller than that in the 5 K/min case. Figures 5.13a and 5.13b show that there is only a slight temperature difference (less than 0.1 K) between the cell center and the cell surface and the temperature distribution along the cell radial direction is nearly homogeneous due to slow heating rate and SEI decomposition which is recognizable in a time range from approximately 2.0 h to 4.0 h in Figure 5.11b.

Figure 5.13c shows a temperature range where cathode runaway chemistry is observed (460 K $\sim$ 490 K). When the cell center temperature is approximately 460.5 K, the temperature distribution along the cell radial direction is almost homogeneous, indicating that there is a small amount of cathode runaway reaction. (Note that 463 K is the temperature where rapid cathode runaway reaction can be initiated, see Section 5.2.2.) However, as time develops, the cell center temperature increases and slightly exceeds the cell surface temperature between 475 K and 480 K where average cell temperature peak is observed in Figure 5.11b. Above 480 K, the cell surface temperature exceeds the cell center temperature indicating that runaway reactions will no longer occur.
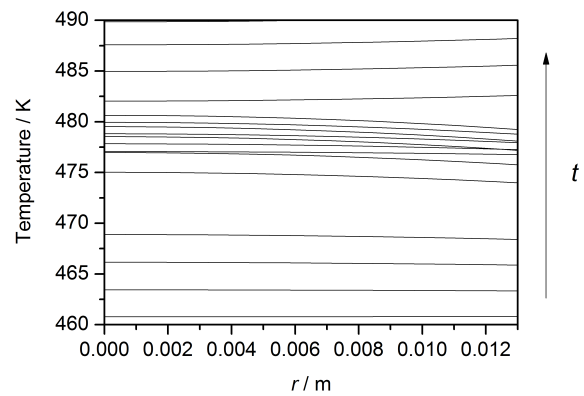
These temperature distribution results suggest that the cell center temperature change is always larger than the cell surface temperature change. These findings are also especially prominent at a high heating rate. Therefore, to assess runaway behavior, it is better to measure cell center temperature than cell surface temperature.
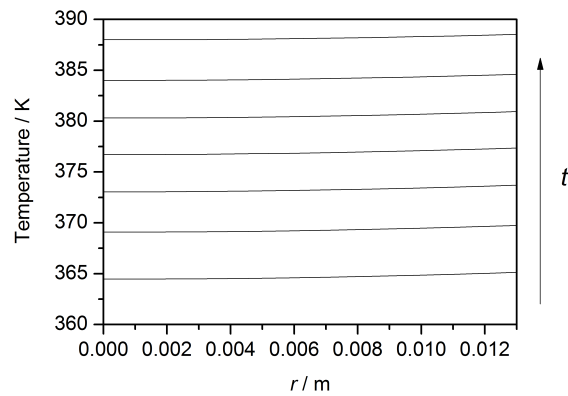
(a) 360 K - 390 K
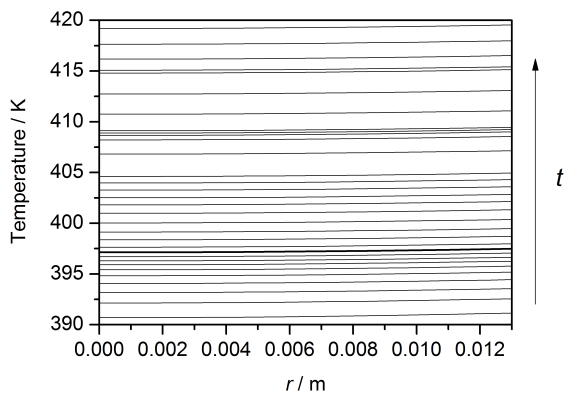
(b) 390 K - 420 K

(c) 460 K - 490 K

Figure 5.13: Temporal average cell temperature distributions along the cell radial direction (Cell center: $r = 0$) under 0.5 K/min heating rate. Time ranges in Figure 5.11b correspond to approximately: (a) 2.0 h - 3.0 h, (b) 3.0 h - 4.0 h, and (c) 5.0 h - 6.0 h.

5.3 Electrical abuse

5.3.1 External short circuit

In order to investigate electrical abuse, we conducted a simulation of an external short circuit and compared it with an an experiment performed by ZSW. ZSW found that the blend cell used in the experiment (Sony SE US26650VT) had a safety device which cut off the current (i.e., CID) during an external short circuit, therefore we only examined an LFP cell to fully investigate the influence of the short circuit on a cell. The LFP cell used in the short-circuit experiment is an ANR26650M1A type cell manufactured by A123 Systems, LLC., and is the same type of cell that was utilized in the experiments of charge and discharge curves shown in Section 5.1.1 [159]. The short-circuit experiment was conducted by connecting positive and negative poles with an electric wire. Here, resistance of a short circuit loop was designed to be less than 5 mΩ (Figure 5.14). In an external short circuit simulation, we conducted a transient simulation with a cell voltage of 0.4 V with an external resistance of 5 mΩ. The initial SOC of a cell is 100% which is a fully charged state both in the simulation and the experiment. As for other parameters of the LFP cell, we utilized the values shown in Section 3.5.1.
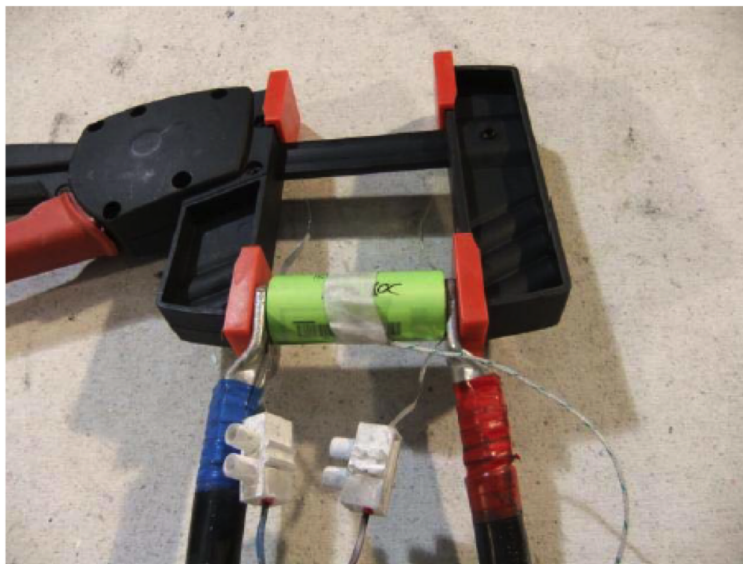

Figure 5.14: Experimental setup of external short circuit. Courtesy of ZSW.

Figures 5.15a and 5.15b show profiles of cell voltage, current, cell surface temperature, and SOC that were obtained from the experiment. The experimental cell voltage dropped from 3.5 V to approximately 0.4 V at 0 s and decreased to 0 V at 10 s, indicating that an internal short circuit eventually drives a current to zero. Experimental current first shoot up to 240 A at 0 s and went down by 20 A in a few seconds. Then, at 10 s, it went up
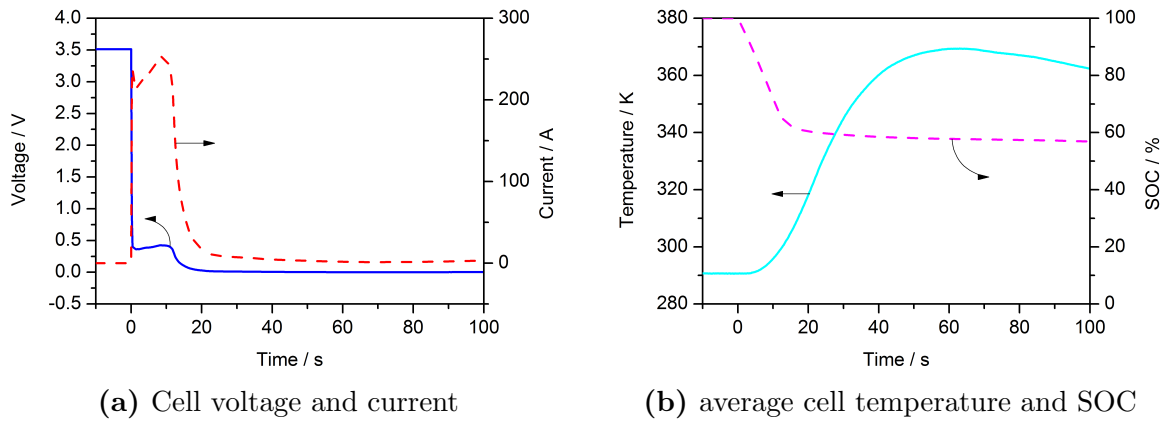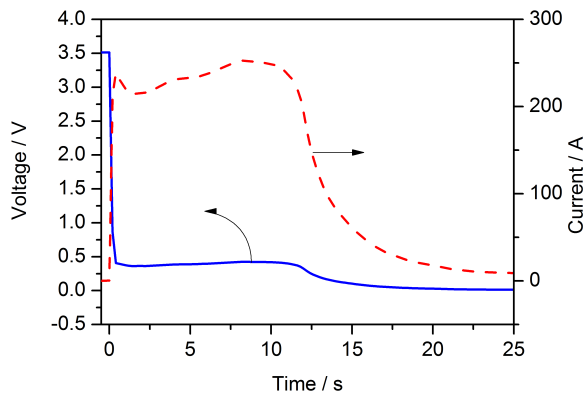
(a) Cell voltage and current   **(b)** average cell temperature and SOC

Figure 5.15: Experimental profiles of cell voltage, current, average cell temperature and SOC under external short circuit up to 100 s conducted by ZSW.

again, reaching approximately 250 A. After, the current reaches its highest peak at 250 A at 10 s, it rapidly drops to nearly zero in 10 s. During these processes, SOC profile decreases from 100% to 58% as shown in Figure 5.15b. The SOC drops linearly between 0 s and 12 s by 40% and then it starts decreasing slightly by few percent up to 100 s. Experimental cell temperature starts increasing at approximately 5 s with a slight delay from the point when the short circuit occurs. The cell temperature reaches approximately 370 K by 60 s and then gradually decreases by cooling through natural convection due to having a lower ambient temperature than the cell surface temperature. The surface temperature increase from the initial temperature is approximately 80 K.

In this simulation, we only conducted external short circuit even though phenomena which indicate an internal short circuit followed the external short circuit in the experiment. Figure 5.16c and 5.16d present the profiles from the simulation results. In order to compare the simulation results, we zoom in on the experimental results between 0 s and 25 s in Figure 5.16a and 5.16b. The simulated voltage drops from 3.5 V to 1.5 V at 0 s and it is nearly constant up to 20 s. Note that the voltage shown in the graph is the total voltage through the external resistance and cell voltage. The cell voltage is kept in 0.4 V throughout the simulation. The current density shoots up to approximately 1500 A/m^2 which corresponds to around 255 A considering that the surface area of electrodes in the LFP cell is 0.171 m^2 as shown in Section 3.5.1. This maximum current value shows good agreement with the experimental value. However, the current density in the simulation shows a different behavior compared to the experiment. The simulated current density draws smooth curves that gradually decrease to 1000 A/m^2. This is when SOC reaches zero as shown in Figure 5.16d. SOC decreases 40% by 10 s which is in good agreement with the experiment. Although the experimental external short circuit was terminated by the internal short circuit at approximately 10 s, the simulation of the external short circuit
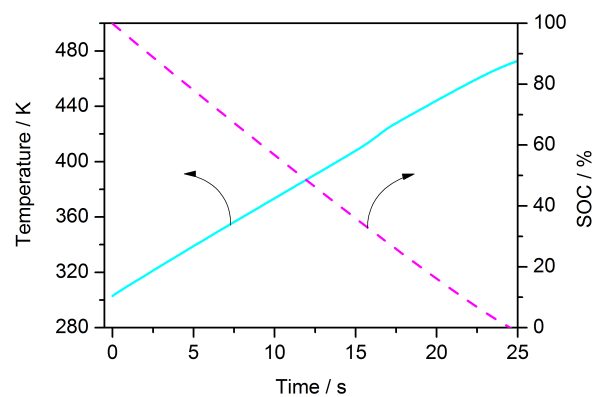
(a) Experimental cell voltage and current
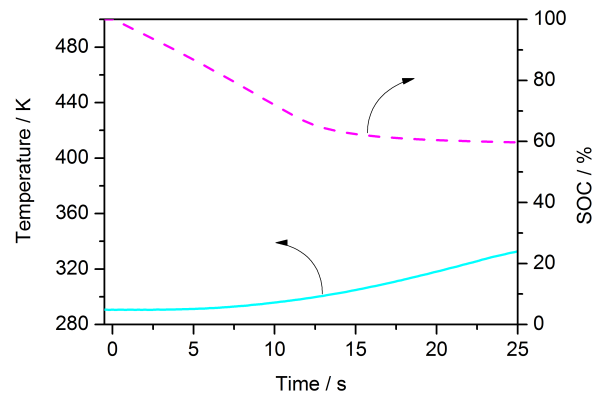
(b) Experimental cell surface temperature and SOC
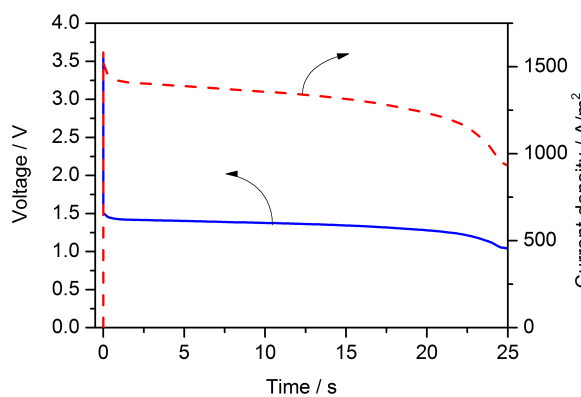
(c) Simulated total voltage through external registance and cell and current

(d) Simulated cell surface temperature and SOC

Figure 5.16: Cell behavior following external short circuit. The experimental data were obtained by ZSW.

continues until SOC reaches zero. The cell surface temperature at 10 s in the simulation is approximately 370 K, whereas the experimental cell surface temperature shows only a slight increase by 10 s. This may be explained by heat released due to thermal conduction through an external wire or resistance. The simulation predicts that the maximum cell surface temperature can reach 470 K if the external short circuit is completed before SOC reaches to zero without heat escape through thermal conduction.

These results show that the simulation could qualitatively reproduce the external short circuit although models need to be extended by descriptions of internal short circuits in future works.

5.3.2 Cycling at elevated temperature

In order to investigate the possibility of thermal runaway under discharge/charge cycling, we conducted full-cell simulations of heavy cycling from 0.1 C to 5 C in various initial/ambient temperatures. Since we found that cathode runaway chemistry is not induced only by SEI formation and decomposition in Section 5.2, we included additional runaway chemistries between gaseous products shown in Section 4.4. We conducted simulations for a cell with a blended cathode in order to examine a higher voltage range in which exothermic reactions are highly probable. Charge and discharge were continuously repeated within a voltage range between 3.0 V and 4.2 V, and ambient temperature was maintained at a constant value throughout the simulation. The initial cell temperature was set at the same value as the ambient temperature. In order to examine temperature dependency, we investigated cell behavior at 333 K, 343 K, 353 K, and 363 K ambient/initial cell temperatures. The initial volume fraction of SEI is 0.1 assuming a used cell. The other battery parameters were defined as reviewed in Section 3.5.1.

Figure 5.17 shows profiles of cell average and ambient temperatures, and volume fraction of SEI under cycling with 5 C. Figure 5.18 shows SEI volume fraction profiles. The voltage and current profiles of the cycling in each temperature are shown in Figure 5.19. At 333 K in ambient temperature (Figure 5.17a), thermal runaway is not observed even after 1.7 hours of cycling and average cell temperature stays at 360 K. However, a decrease in SEI volume fraction is observed by approximately 0.002 at 6000 s indicating SEI decomposition is more dominant than SEI formation (Figure 5.18a). At 343 K ambient temperature, a sudden exponential temperature rise (i.e., onset of thermal runaway) appears after three cycles (Figures 5.17b and 5.19b). This temperature increase is associated with SEI decomposition that induces the reactions of ethylene oxidation and hydration of lithium. SEI volume fraction starts decreasing at 1000 s, and thermal runaway is observed when SEI volume fraction reaches 0.09 at 3500 s where the average cell temperature is nearly

(a) Initial/ambient temperature 333 K

(b) Initial/ambient temperature 343 K

(c) Initial/ambient temperature 353 K

(d) Initial/ambient temperature 363 K
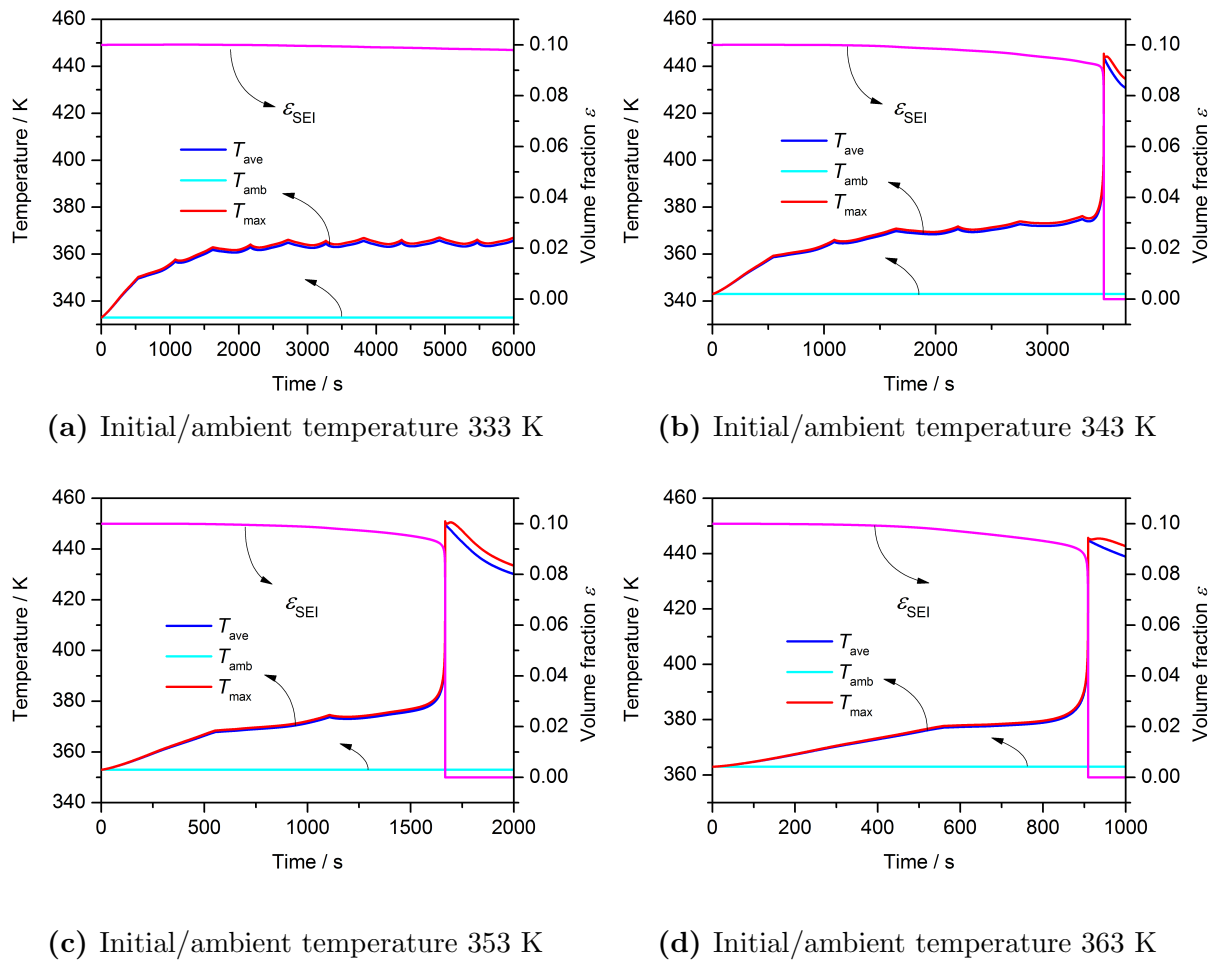
Figure 5.17: Profiles of cell average, maximum and ambient temperatures and SEI volume fraction under 5 C cycling at initial/ambient temperature of 333, 343, 353, and 363 K.
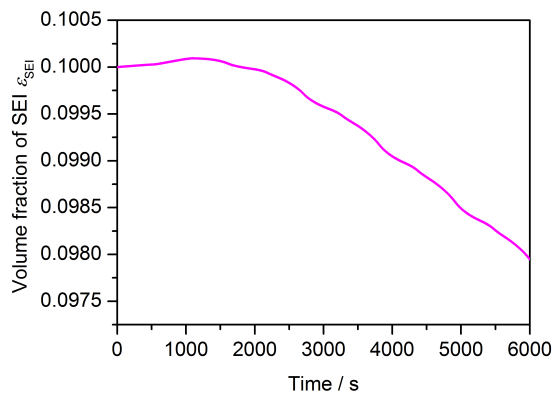
(a) Initial/ambient temperature 333 K
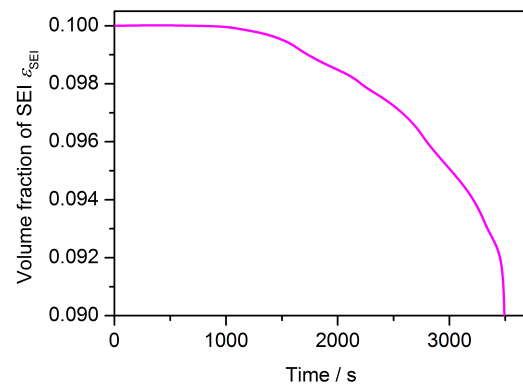
(b) Initial/ambient temperature 343 K
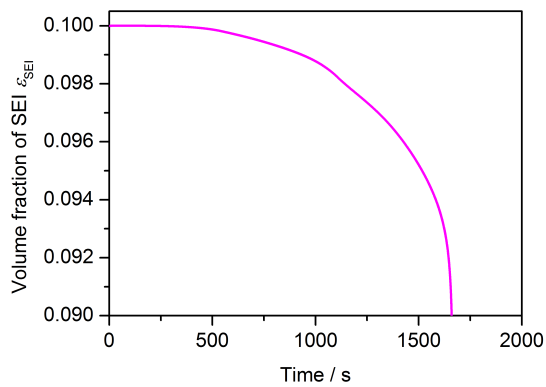
(c) Initial/ambient temperature 353 K

(d) Initial/ambient temperature 363 K

Figure 5.18: Profiles of SEI volume fraction under 5 C cycling at initial/ambient temperature of 333, 343, 353, and 363 K.

(a) Initial/ambient temperature 333 K

(b) Initial/ambient temperature 343 K

(c) Initial/ambient temperature 353 K
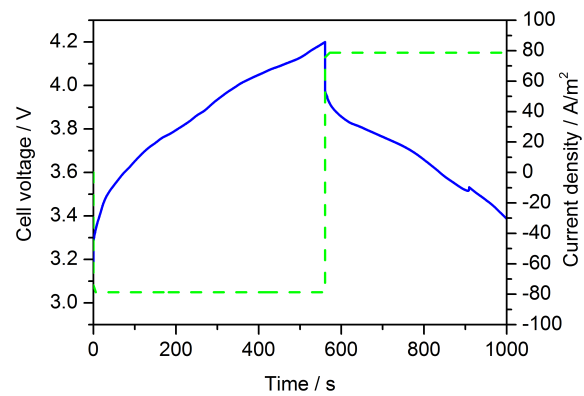
(d) Initial/ambient temperature 363 K

Figure 5.19: Profiles of cell voltage and current density under 5 C cycling in initial/ambient temperature of 333, 343, 353, and 363 K.
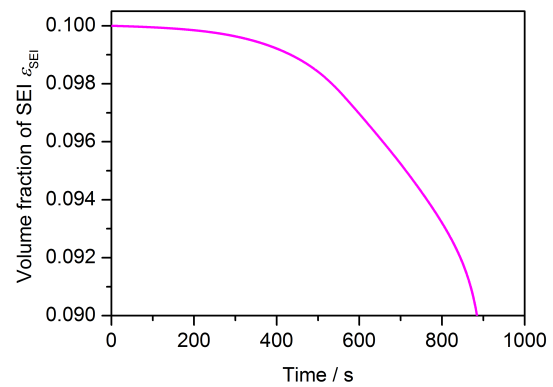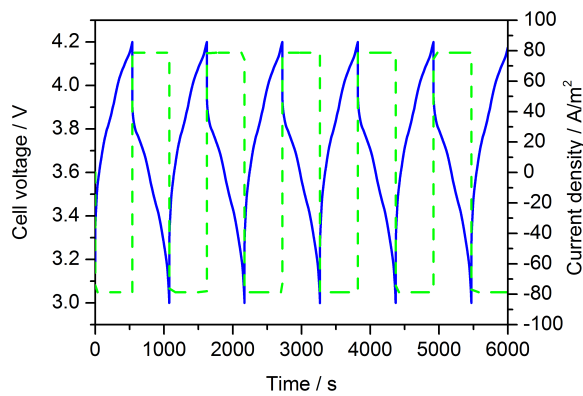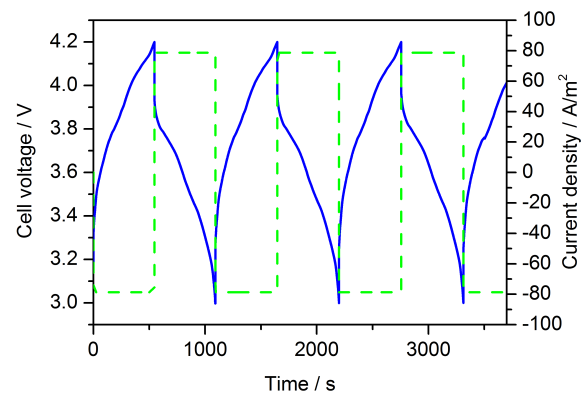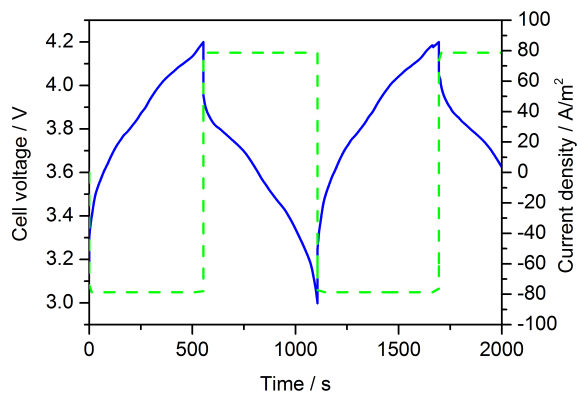
380 K (Figure 5.18b). On the other hand, without the ethylene oxidation and hydration of lithium reactions, an exponential temperature increase was not observed and only a slight temperature increase from cycling and SEI decomposition occurred. At 3500 s, the maximum average cell temperature reaches 450 K, it is approximately 10 K lower than the critical temperature needed to induce thermal runaway on the cathode side from the cathode runaway chemistries (i.e., the exponential temperature rise observed at 463 K ambient temperature in Figure 5.5). At 353 K and 363 K ambient temperatures, thermal runaway is observed after 1.5 cycle (Figures 5.17c and 5.19c) and after 1 cycle (Figures 5.17d and 5.19d), respectively. The maximum temperature reached from the runaway at 353 K and 363 K ambient temperature is 450 K, which is same temperature reached in the 343 K case. This is because the SEI decomposition initiation temperature is similar at every ambient temperature.

These results suggest that the anode runaway chemistries including ethylene oxidation and hydration of lithium do not release enough heat to induce an exponential temperature rise on the cathode side with an average SEI volume fraction, even under severe cycling with 5 C. However, the simulated maximum temperature is only 10 K below the critical temperature of cathode runaway chemistries (see Section 5.2.2). Therefore, it is likely that thermal insulation or lack of cooling (e.g., battery arrays in a battery pack) can cause even worse thermal runaway by chain reactions of highly exothermic runaway chemistries on both anode and cathode sides.

6 Summary and Outlook

6.1 Summary

Lithium-ion batteries are currently one of the most common commercialized batteries on the global market by virtue of their high energy density. However, lithium-ion batteries have suffered safety issues such as thermal runaway. Several exothermic degradation mechanisms play key roles in the thermal runaway of lithium-ion batteries. In this thesis, the goal is to provide a detailed analysis of degradation mechanisms (i.e., runaway chemistries) inside of a cell by the development of numerical models of runaway chemistries which are coupled to an electrochemical battery model, as well as predictions of conditions which possibly cause thermal runaway.

The background chapter (Chapter 2) provided general knowledge of rechargeable lithium-ion batteries related to thermal runaway, including explanations of components and an overview of numerical simulations of lithium-ion batteries. The battery component overview explained anode and cathode materials, electrolyte, SEI, separator and current collectors. The numerical simulation overview showed common methods of current battery simulation including thermal simulation.

Detailed methods used in this thesis were presented in Chapter 3. Lithium-ion batteries with two types of cathodes (LFP, and a blend of NCA and LMO) were investigated in this work. The numerical simulations were conducted utilizing the software packages DENIS and Cantera. As a basis for simulations of thermal runaway, we extended the DENIS/Cantera framework:

1. In order to realize thermal simulations in the framework, DENIS was extended to internally couple with Cantera in terms of heat sources.

2. Cantera was extended to return the reaction enthalpy which was utilized for thermal calculations.

3. To achieve DSC simulations, DENIS was extended to return heat flow from each component.

4. As input parameters, NASA polynomials were derived from heat coefficients and the standard enthalpies and entropies of formation for species whose thermodynamic data is not available in the NASA database.

Models of runaway chemistries in both the anode and the cathode were developed (Chapter 4). The runaway chemistries were established in models of global reactions and the parameters of the reactions were obtained either through literature or by fitting to DSC experimental results taken from literature. DSC simulations were conducted for each electrode to validate and to obtain the kinetic parameters of the global reactions. The models of runaway chemistries established in this work include SEI formation and decomposition, oxygen release from the cathode and solvent oxidation by the released oxygen, as well as reactions between gas products of SEI decomposition reaction (i.e., ethylene oxidation and lithium hydration). The following results were obtained:

1. It is known that the first exothermic reaction in thermal runaway situations is SEI decomposition. Therefore, the need arose to include SEI formation and decomposition reactions on the anode side. As for the SEI formation, the SEI was assumed to be a product of an irreversible reaction between ethylene carbonate and lithium ions on the anode side based on DFT calculations and experimental studies about SEI formation shown in literature. A kinetic model of SEI formation was constructed based on an aging model of a battery available in literature. In addition, a film growth model was applied to make the model consistent with actual SEI thicknesses, 10 - 100 nm.

2. SEI decomposition was modeled based on the assumption of a metastable SEI that decomposes to stable SEI and gaseous products as proposed and confirmed by experiments in literature. In the model, we assumed that SEI decomposition is a first order reaction. Parameters were taken from literature and the model was validated by comparison with DSC simulation results shown in literature. Furthermore, the SEI decomposition model was coupled with the model of SEI formation, and comprehensive DSC simulation for the anode was implemented. The models of simultaneous SEI formation and decomposition were validated by comparison to a DSC experimental result shown in literature.

3. As for runaway reactions on the cathode side, we modeled oxygen evolution from a cathode active material and solvent oxidation by the released oxygen for a cell with a blend type cathode. We did not model these reactions for a LFP cell because it is known that the oxygen evolution is suppressed in olivine type cells. The model was constructed as a global reaction which includes both oxygen evolution from a cathode active material and solvent oxidation by the released oxygen, a mechanism

that has been experimentally confirmed by DSC and XPS experiments. The kinetic parameters of the model were obtained and validated by comparison between DSC simulation and experiments.

4. Reactions between gaseous products of SEI decomposition with an associated exothermic reaction were modeled for a closed battery can environment which DSC cannot capture due to its requirement of an open environment for the sample. Here, we assumed two reactions: oxidation of ethylene and hydration of lithium by H_2O produced through the oxidation of ethylene. These reactions were modeled to be highly exothermic reactions which possibly induce reactions which have a high onset temperature (i.e., cathode runaway chemistries).

Utilizing the developed runaway chemistries of electrodes, we conducted full-cell simulations (Chapter 5). The full-cell model was first calibrated under nominal operating conditions for both LFP and blend cells. With the calibrated models, we investigated degradation processes and their influences on cell temperatures under thermal and electrical abuse. Thermal abuse included cell heating by constant elevated ambient temperatures and temperature ramps with various constant heating rates. As for electrical abuse, we studied an external short circuit and heavy cycling. We gained the following insights through the full-cell simulations under extreme conditions:

1. Under elevated constant ambient temperatures ranging from 373 K to 400 K, SEI decomposition and formation in a LFP cell were investigated. Simulation results suggest that it is unlikely for the LFP cell to suffer thermal runaway only with the simultaneous reactions even at an elevated temperature unless there are additional triggers like short circuits, although a cell can be damaged by consumption of electrolyte (i.e., fast aging of a cell).

2. Similarly, a blend cell was examined within a range of constant temperatures from 443 K to 483 K. For the blend cell model, oxygen evolution from cathode active material and oxidation of electrolyte were included in addition to SEI formation and decomposition. Results showed that the critical temperature of thermal runaway (i.e., the exponential increase of cell temperature) lies between 453 K and 463 K under natural convection. Moreover, it is unlikely that the SEI decomposition and formation directly induces the cathode runaway chemistry due to its low heat release rate when the volume fraction of SEI is less than 0.1.

3. Ambient temperature ramps with constant heating rates were applied to an LFP cell which has runaway chemistries only at the anode side. Simulation results indicate that behavior of cell average temperature largely depends on the heating rates.

Under higher heating rates, there is a possibility that we miss signals of degradations inside a cell if we only measure temperature.

4. Ambient temperature ramps were also applied to the blend type cell. Simulation results showed that each heating rate resulted in different reaction rates of cathode runaway chemistries depending on completion rate of anode runaway reactions due to common reactants among both reactions. The difference between heating rates indicates that degradation phenomena can be highly influenced by the heating history of a cell if a cell would have been exposed to several heating conditions.

5. Simulation of an external short circuit was conducted for a fully-charged LFP cell. The simulation results were compared with experimental data obtained by ZSW. The results showed that the simulation could qualitatively reproduce the external short circuit. However, models need to be extended by descriptions of internal short circuits in future works to fully reproduce phenomena associated with experimental external short circuit.

6. Simulations of heavy cycling were conducted for the blend type cell at 5 C under high ambient temperatures over 333 K. In this model, we extended anode runaway chemistries with oxidation of ethylene and hydration of lithium in addition to SEI formation and decomposition reactions as well as oxygen evolution from a cathode active material and solvent oxidation. Thermal runaway was observed due to the extended anode runaway reactions. Furthermore, the maximum temperature reached by the anode thermal runaway maybe sufficiently close to the critical temperature of cathode runaway chemistries. Therefore, it is likely that thermal insulation or lack of cooling (e.g., battery arrays in battery pack) can cause extended chain reactions of runaway chemistries in both electrodes.

This thesis has presented the first thermo-electrochemical numerical simulations of battery thermal runaway incorporating runaway chemistries at both electrodes. We gained a detailed insight how the runaway chemistries are influenced by cell conditions under thermal and electrical abuse conditions. The numerical prediction of cell runaway behaviors can be applied to construct mitigation strategise against severe thermal failures.

6.2 Outlook

The presented work is a strong base for further studies. The thermal runaway models are planned to be coupled with a stochastic simulation which enables to deal with uncertainties in operations or in the manufacturing processes. Furthermore, the thermal coupling in

the DENIS/Cantera framework will allow to provide thermal calculations for ongoing research of electrochemical energy devices such as fuel cells and various types of batteries. For future research, the following should be considered:

1. The battery model with the thermal runaway features can be applied to deductive failure analysis such as Fault Tree Analysis (FTA). The analysis enables us to understand the contributors of the failure event even from system levels. It can be utilized in a heat management system of an electric vehicle to avoid severe accidents due to thermal runaway of batteries. Moreover, the analysis would provide visions for further researches towards safe battery components.

2. The runaway chemistries can be applicable for battery aging analyses as several reactions consume lithium. It is also possible to explore the aging mechanism by including further reactions which occur at temperatures lower than room temperature. The simulation can predict the level of aging depending on operational history of cells.

3. While the work presented here was conducted in 1D, runaway reaction mechanisms can be included in 3D simulations. 3D models can either describe full cells with medium resolution or can represent parts of a battery with higher resolution of active material structures. Furthermore, 3D would allow for the location of thermally critical points ("hot spots") and thus, insights towards a safer battery structure can be obtained.

Bibliography

[1] National Research Council. Climate Change: Evidence, Impacts, and Choices, 2012.

[2] United Nations Framework Convention on Climate Change. http://www.unfccc.int. (Retrieved: 05/02/2014).

[3] United Nations Framework Convention on Climate Change, Kyoto Protocol. http://unfccc.int/kyoto_protocol/items/3145.php. (Retrieved: 05/02/2014).

[4] D. Talbot. The great german energy experiment. http://www.technologyreview.com/featuredstory/428145/the-great-german-energy-experiment/, 2012. (Retrieved: 05/02/2014).

[5] D. Boehme. Development of renewable energy sources in Germany 2012. Technical report, Federal Ministry for the Environment, Nature Conservation and Nuclear Safety, 2013.

[6] S. Angel. Smart grid: Implications and opportunities for clean energy and greenhouse gas emissions reductions. Technical report, U.S. Environmental Protection Agency, 2010.

[7] W. F. Christian Feisst, Dirk Schlesinger. Smart grid the role of electricity infrastructure in reducing greenhouse gas emissions. Technical report, Cisco Internet Business Solutions Group, 2008.

[8] SmartGrid.gov by the U.S. Department of Energy. http://www.smartgrid.gov/. (Retrieved: 05/02/2014).

[9] F. Porsche. *Hybrid Automobile Pioneer*. Porsche Museum, 2010.

[10] Porsche Archive. http://www.porsche.com/international/aboutporsche/porschemuseum/historyporschearchive/milestones/. (Retrieved: 13/02/2014).

[11] Toyota Prius Press release. http://www2.toyota.jp/jp/news/13/07/nt13_0701.pdf. (Retrieved: 13/02/2014).

[12] Toyota Prius 2013. http://www.toyota.com/prius/. (Retrieved: 13/02/2014).

[13] D. Doughty and E. P. Roth. A General Discussion of Li Ion Battery Safety. *Interface-Electrochemical Society*, pages 37–44, 2012.

[14] Global Lithium Ion battery Market - Industry Analysis, Size, Share, Growth, Trends, and Forecast, 2013 - 2019. http://www.researchandmarkets.com/research/5lcn66/global_lithium. (Retrieved: 17/02/2014).

[15] D. Linden and T. B. Reddy. *Handbook of Batteries*. McGraw-Hill Companies, Inc., New York, 3rd editio edition, 2002.

[16] US Federal Aviation Administration Battery Incident Chart. http://www.faa.gov/about/office_org/headquarters_offices/ash/ash_programs/hazmat/aircarrier_info/media/battery_incident_chart.pdf. (Retrieved: 17/02/2014).

[17] C. Mikolajczak, M. Kahn, K. White, and R. T. Long. Lithium-Ion Batteries Hazard and Use Assessment. Technical Report July, Exponent Failure Analysis Associates, Inc., 2011.

[18] H. Maleki and J. N. Howard. Internal short circuit in Li-ion cells. *Journal of Power Sources*, 191(2):568–574, 2009.

[19] K. Kitoh and H. Nemoto. 100 Wh Large size Li-ion batteries and safety tests. *Journal of Power Sources*, 81-82:887–890, 1999.

[20] G.-H. Kim, A. Pesaran, and R. Spotnitz. A three-dimensional thermal abuse model for lithium-ion cells. *Journal of Power Sources*, 170(2):476–489, 2007.

[21] R. Spotnitz and J. Franklin. Abuse behavior of high-power, lithium-ion cells. *Journal of Power Sources*, 113(1):81–100, 2003.

[22] G.-Y. Kim and J. R. Dahn. Effects of Electrode Density on the Safety of NCA Positive Electrode for Li-Ion Batteries. *Journal of the Electrochemical Society*, 160(8):A1108–A1111, 2013.

[23] M. Winter and J. Besenhard. Insertion electrode materials for rechargeable lithium batteries. *Advanced materials*, (10):725–763, 1998.

[24] D. MacNeil, Z. Lu, Z. Chen, and J. Dahn. A comparison of the electrode/electrolyte reaction at elevated temperatures for various Li-ion battery cathodes. *Journal of Power Sources*, 108(1-2):8–14, 2002.

[25] J. Yamaki, H. Takatsuji, T. Kawamura, and M. Egashira. Thermal stability of graphite anode with electrolyte in lithium-ion cells. *Solid State Ionics*, 148:241–245, 2002.

[26] S. Tobishima and J. Yamaki. A consideration of lithium cell safety. *Journal of Power Sources*, 81-82:882–886, 1999.

[27] G.-A. Nazri and G. Pistoia. *LITHIUM BATTERIES Science and Technology.* Soringer Science + Business Media, LLC, New York, USA, 2009.

[28] Y. Reynier, R. Yazami, and B. Fultz. Thermodynamics of lithium intercalation into graphites and disordered carbons. *Journal of The Electrochemical Society*, pages 422–426, 2004.

[29] R. J. Brodd. *Batteries for Sustainability.* Springer, New York, USA, 2013 edition, 2012.

[30] A. Padhi. Phospho olivines as Positive Electrode Materials for Rechargeable Lithium Batteries. *Journal of Electrochemical Society*, 144(4):1–7, 1997.

[31] J. L. Dodd. *Phase Composition and Dynamical Studies of Lithium Iron Phosphate.* PhD thesis, California Institute of Technology, 2007.

[32] A. Andersson, B. Kalska, L. Häggström, and J. Thomas. Lithium extraction/insertion in LiFePO 4: an X-ray diffraction and Mössbauer spectroscopy study. *Solid State Ionics*, 130:41–52, 2000.

[33] A. Andersson and J. Thomas. The source of first-cycle capacity loss in $LiFePO_4$. *Journal of Power Sources*, 98:498–502, 2001.

[34] V. Srinivasan and J. Newman. Discharge Model for the Lithium Iron-Phosphate Electrode. *Journal of The Electrochemical Society*, 151(10):A1517, 2004.

[35] G. Chen, X. Song, and T. J. Richardson. Electron Microscopy Study of the $LiFePO_4$ to $FePO_4$ Phase Transition. *Electrochemical and Solid-State Letters*, 9(6):A295, 2006.

[36] L. Laffont, C. Delacourt, and P. Gibot. Study of the $LiFePO_4/FePO_4$ two-phase system by high-resolution electron energy loss spectroscopy. *Chemistry of Materials*, 152(5):5520–5529, 2006.

[37] S. Yang, Y. Song, P. Y. Zavalij, and S. Whittingham, M. Reactivity, stability and electrochemical behavior of lithium iron phosphates. *Electrochemistry Communications*, 4:239–244, 2002.

[38] M. Thackeray. Lithium-ion batteries: An unexpected conductor. *Nature materials*, pages 81–82, 2002.

[39] K. E. Thomas, C. Bogatu, and J. Newman. Measurement of the Entropy of Reaction as a Function of State of Charge in Doped and Undoped Lithium Manganese Oxide. *Journal of The Electrochemical Society*, 148(6):A570, 2001.

[40] Y. Dai, L. Cai, and R. E. White. Capacity Fade Model for Spinel $LiMn_2O_4$ Electrode. *Journal of the Electrochemical Society*, 160(1):A182–A190, 2012.

[41] D. D. MacNeil and J. R. Dahn. The Reaction of Charged Cathodes with Non-aqueous Solvents and Electrolytes: II. $LiMn_2O_4$ charged to 4.2 V. *Journal of The Electrochemical Society*, 148(11):A1211, 2001.

[42] H. Tsunekawa, S. Tanimoto, R. Marubayashi, M. Fujita, K. Kifune, and M. Sano. Capacity Fading of Graphite Electrodes Due to the Deposition of Manganese Ions on Them in Li-Ion Batteries. *Journal of The Electrochemical Society*, 149(10):A1326, 2002.

[43] S. B. Chikkannanavar, D. M. Bernardi, and L. Liu. A review of blended cathode materials for use in Li-ion batteries. *Journal of Power Sources*, 248:91–100, 2014.

[44] H. Yang and J. Prakash. Determination of the Reversible and Irreversible Heats of a $LiNi_{0.8}Co_{0.15}Al_{0.05}O_2$/Natural Graphite Cell Using Electrochemical-Calorimetric Technique. *Journal of The Electrochemical Society*, 151(8):A1222, 2004.

[45] Y. Zhang and C.-Y. Wang. Cycle-Life Characterization of Automotive Lithium-Ion Batteries with $LiNiO_2$ Cathode. *Journal of The Electrochemical Society*, 156(7):A527, 2009.

[46] S. Hwang, W. Chang, S. M. Kim, D. Su, D. H. Kim, J. Y. Lee, K. Y. Chung, and E. A. Stach. Investigation of Changes in the Surface Structure of $Li_xNi_{0.8}Co_{0.15}Al_{0.05}O_2$ Cathode Materials Induced by the Initial Charge. *Chemistry of Materials*, 26:1084–1092, 2014.

[47] I. Belharouak, D. Vissers, and K. Amine. Thermal Stability of the $Li(Ni_{0.8}Co_{0.15}Al_{0.05})O_2$ Cathode in the Presence of Cell Components. *Journal of The Electrochemical Society*, 153(11):A2030, 2006.

[48] H. Y. Tran, C. Täubert, M. Fleischhammer, P. Axmann, L. Küppers, and M. Wohlfahrt-Mehrens. $LiMn_2O_4$ Spinel $LiNi_{0.8}Co_{0.15}Al_{0.05}O_2$ Blends as Cathode Materials for Lithium-Ion Batteries. *Journal of The Electrochemical Society*, 158(5):A556, 2011.

[49] B. Deng, H. Nakamura, and M. Yoshio. Superior Capacity Retention of Oxygen Stoichiometric Spinel $Li_{1+x}Mn_{2+x}O_{4+\delta}$ at Elevated Temperature. *Electrochemical and Solid-State Letters*, 8(3):A171, 2005.

[50] H. Maleki, G. Deng, A. Anani, and J. Howard. Thermal Stability Studies of Li ion Cells and Components. *Journal of The Electrochemical Society*, 146(9):3224–3229, 1999.

[51] P. Albertus, J. Christensen, and J. Newman. Experiments on and Modeling of Positive Electrodes with Multiple Active Materials for Lithium-Ion Batteries. *Journal of The Electrochemical Society*, 156(7):A606, 2009.

[52] K. Takada, T. Inada, A. Kajiyama, and H. Sasaki. Solid-state lithium battery with graphite anode. *Solid State Ionics*, 158:269–274, 2003.

[53] T. Kobayashi, Y. Imade, D. Shishihara, K. Homma, M. Nagao, R. Watanabe, T. Yokoi, A. Yamada, R. Kanno, and T. Tatsumi. All solid-state battery with sulfur electrode and thio-LISICON electrolyte. *Journal of Power Sources*, 182(2):621–625, 2008.

[54] N. Kamaya, K. Homma, Y. Yamakawa, M. Hirayama, R. Kanno, M. Yonemura, T. Kamiyama, Y. Kato, S. Hama, K. Kawamoto, and A. Mitsui. A lithium superionic conductor. *Nature materials*, 10(9):682–6, 2011.

[55] S. Boulineau, J.-M. Tarascon, J.-B. Leriche, and V. Viallet. Electrochemical properties of all-solid-state lithium secondary batteries using Li-argyrodite Li_6PS_5Cl as solid electrolyte. *Solid State Ionics*, 242:45–48, 2013.

[56] K. Xu. Nonaqueous liquid electrolytes for lithium-based rechargeable batteries. *Chemical reviews*, 2004.

[57] W. Elliott. Report No. 1, Contract NAS 3-6015 (N65-11518). Technical report, 1964.

[58] G. Pistoia, M. D. Rossi, and B. Scrosati. Study of the Behavior of Ethylene Carbonate as a Nonaqueous Battery Solvent. *Journal of The Electrochemical Society*, 501(4):500–502, 1970.

[59] S. Zhang, Q. Liu, and L. Yang. Polyacene as an anode in lithium ion batteries. *Journal of The Electrochemical Society*, 140(7):246–247, 1993.

[60] J. Dahn and U. V. Sacken. Rechargeable $LiNiO_2$/carbon cells. *Journal of The Electrochemical Society*, 138(8), 1991.

[61] T. Ohzuku, Y. Iwakoshi, and K. Sawai. Formation of Lithium-Graphite Intercalation Compounds in Nonaqueous Electrolytes and Their Application as a Negative Electrode for a Lithium Ion (Shuttlecock) Cell. *Journal of The Electrochemical Society*, 140(9), 1993.

[62] D. Guyomard and J. M. Tarascon. Rechargeable $Li_{1+x}Mn_2O_4$/Carbon Cells with a New Electrolyte Composition. *Journal of Electrochemical Society*, 140(11):3071–3081, 1993.

[63] J. Tarascon and D. Guyomard. New electrolyte compositions stable over the 0 to 5 V voltage range and compatible with the $Li_{1+x}Mn_2O_4$/carbon Li-ion. *Solid State Ionics*, 69:293–305, 1994.

[64] Y. Ein-Eli, S. Thomas, and V. Koch. Ethylmethylcarbonate, a Promising Solvent for Li-Ion Rechargeable Batteries. *Journal of The Electrochemical Society*, 143(12):1–5, 1996.

[65] D. Aurbach, Y. Ein-Eli, B. Markovsky, and A. Zaban. The Study of Electrolyte Solutions Based on Ethylene and Diethyl Carbonates for Rechargeable Li Batteries II. Graphite Electrodes. *Journal of The Electrochemical Society*, 142(9):2882–2889, 1995.

[66] P. Verma, P. Maire, and P. Novák. A review of the features and analyses of the solid electrolyte interphase in Li-ion batteries. *Electrochimica Acta*, 55(22):6332–6341, 2010.

[67] K. Edström, M. Herstedt, and D. P. Abraham. A new look at the solid electrolyte interphase on graphite anodes in Li-ion batteries. *Journal of Power Sources*, 153(2):380–384, 2006.

[68] T. Yoshida, M. Takahashi, S. Morikawa, C. Ihara, H. Katsukawa, T. Shiratsuchi, and J. Yamaki. Degradation Mechanism and Life Prediction of Lithium-Ion Batteries. *Journal of The Electrochemical Society*, 153(3):A576–A582, 2006.

[69] J.-i. Yamaki, Y. Baba, N. Katayama, H. Takatsuji, M. Egashira, and S. Okada. Thermal stability of electrolytes with Li_xCoO_2 cathode or lithiated carbon anode. *Journal of Power Sources*, 119-121:789–793, 2003.

[70] J. Christensen and J. Newman. A Mathematical Model for the Lithium-Ion Negative Electrode Solid Electrolyte Interphase. *Journal of The Electrochemical Society*, 151(11):A1977, 2004.

[71] H. Yoshida, T. Fukunaga, T. Hazama, M. Terasaki, M. Mizutani, and M. Yamachi. Degradation mechanism of alkyl carbonate solvents used in lithium-ion cells during initial charging. *Journal of Power Sources*, 68(2):311–315, 1997.

[72] K. Tasaki. Solvent decompositions and physical properties of decomposition compounds in Li-ion battery electrolytes studied by DFT calculations and molecular dynamics simulations. *The journal of physical chemistry. B*, 109(7):2920–33, 2005.

[73] Y. Wang, S. Nakamura, M. Ue, and P. B. Balbuena. Theoretical studies to understand surface chemistry on carbon anodes for lithium-ion batteries: reduction mechanisms of ethylene carbonate. *Journal of the American Chemical Society*, 123(47):11708–11718, 2001.

[74] D. Aurbach, Y. Ein-Eli, and O. Chusid. The Correlation Between the Surface Chemistry and the Performance of Li-Carbon Intercalation Anodes for Rechargeable 'Rocking-Chair'Type Batteries. *Journal of The Electrochemical Society*, 141(3):603–611, 1994.

[75] D. Aurbach. Review of selected electrode-solution interactions which determine the performance of Li and Li ion batteries. *Journal of Power Sources*, 89(2):206–218, 2000.

[76] D. Aurbach and Y. Ein-Eli. The Study of Li-Graphite Intercalation Processes in Several Electrolyte Systems Using In Situ X-Ray Diffraction. *Journal of The Electrochemical Society*, 142(6):1746–1752, 1995.

[77] E. Peled and D. Golodnitsky. An advanced tool for the selection of electrolyte components for rechargeable lithium batteries. *Journal of The Electrochemical Society*, 145(10):3482–3486, 1998.

[78] E. Endo, M. Ata, K. Tanaka, and K. Sekai. Electron spin resonance study of the electrochemical reduction of electrolyte solutions for lithium secondary batteries. *Journal of The Electrochemical Society*, 145(11):3757–3764, 1998.

[79] J. Besenhard, M. Winter, J. Yang, and W. Biberacher. Filming mechanism of lithium-carbon anodes in organic and inorganic electrolytes. *Journal of Power Sources*, 54(2):228–231, 1995.

[80] J. Dahn. Phase diagram of Li_xC_6. *Physical Review B*, 44(17):9170–9177, 1991.

[81] Y. Mizutani, T. Abe, K. Ikeda, E. Ihara, M. Asano, T. Harada, M. Inaba, and Z. Ogumi. Graphite intercalation compounds prepared in solutions of alkali metals in 2-methyltetrahydrofuran and 2, 5-dimethyltetrahydrofuran. *Carbon*, 35(1):61–65, 1997.

[82] A. D. Pasquier, F. Disma, T. Bowmer, A. S. Gozdz, G. Amatucci, and J.-M. Tarascon. Differential Scanning Calorimetry Study of the Reactivity of Carbon Anodes in Plastic Li - Ion Batteries. *Journal of the Electrochemical Society*, 145(2):472–477, 1998.

[83] M. Richard and J. Dahn. Accelerating rate calorimetry study on the thermal stability of lithium intercalated graphite in electrolyte. I. Experimental. *Journal of The Electrochemical Society*, 146(6):2068–2077, 1999.

[84] D. D. MacNeil, D. Larcher, and J. R. Dahn. Comparison of the reactivity of various carbon electrode materials with electrolyte at elevated temperature. *Journal of the Electrochemical Society*, 146(10):3596–3602, 1999.

[85] D. Aurbach, A. Zaban, A. Schechter, Y. Ein-Eli, E. Zinigrad, and B. Markovsky. The study of electrolyte solutions based on ethylene and diethyl carbonates for rechargeable Li batteries I. Li Metal Anodes. *Journal of Electrochemical Society*, 142(9):2873–2882, 1995.

[86] D. Bar-Tow, E. Peled, and L. Burstein. A Study of Highly Oriented Pyrolytic Graphite as a Model for the Graphite Anode in Li-Ion Batteries. *Journal of the Electrochemical Society*, 146(3):824–832, 1999.

[87] Y. Ein-Eli, S. Thomas, and R. Chadha. Li-Ion Battery Electrolyte Formulated for Low-Temperature Applications. *Journal of the Electrochemical Society*, 144(3):823–829, 1997.

[88] M. N. Richard and J. R. Dahn. Calorimetry study on the thermal stability of lithium intercalated graphite in electrolyte. II. Modeling the results and predicting differential scanning calorimeter curves. *Journal of The Electrochemical Society*, 146(6):2078–2084, 1999.

[89] J. Jiang and J. Dahn. Effects of solvents and salts on the thermal stability of LiC6. *Electrochimica Acta*, 49(26):4599–4604, 2004.

[90] A. M. Andersson, D. P. Abraham, R. Haasch, S. MacLaren, J. Liu, and K. Amine. Surface Characterization of Electrodes from High Power Lithium-Ion Batteries. *Journal of The Electrochemical Society*, 149(10):A1358, 2002.

[91] E. P. Roth, C. C. Crafts, D. H. Doughty, and J. McBreen. Advanced Technology Development Program for Lithium-Ion Batteries: Thermal Abuse Performance of 18650 Li-Ion Cells. Technical Report March, Sandia National Laboratories, Albuquerque, New Mexico, 2004.

[92] S.-T. Myung, Y. Sasaki, S. Sakurada, Y.-K. Sun, and H. Yashiro. Electrochemical behavior of current collectors for lithium batteries in non-aqueous alkyl carbonate solution and surface analysis by ToF-SIMS. *Electrochimica Acta*, 55(1):288–297, 2009.

[93] A. H. Whitehead and M. Schreiber. Current Collectors for Positive Electrodes of Lithium-Based Batteries. *Journal of The Electrochemical Society*, 152(11):A2105–A2113, 2005.

[94] K. E. Thomas, J. Newman, and R. M. Darling. *Advances in Lithium-Ion Batteries*. Kluwer Academic Plenum Publishers, New York, USA, 2002.

[95] J. Newman and W. Tiedemann. Porous-electrode theory with battery applications. *AIChE Journal*, 21(1):25–41, 1975.

[96] G. G. Botte, V. R. Subramanian, and R. E. White. Mathematical modeling of secondary lithium batteries. *Electrochimica Acta*, 45(15-16):2595–2609, 2000.

[97] J. Newman and K. E. Thomas. *Electrochemical Systems*. Wiley Interscience, Hoboken, New Jersey, third edition, 2004.

[98] C. Wang, W. Gu, and B. Liaw. Micro-Macroscopic Coupled Modeling of Batteries and Fuel Cells I. Model Development. *Journal of The Electrochemical Society*, 145(10):3407–3417, 1998.

[99] D. Bernardi, E. Pawlikowski, and J. Newman. A general energy balance for battery systems. *Journal of The Electrochemical Society*, 132(1):5–12, 1985.

[100] L. Rao and J. Newman. Heat-Generation Rate and General Energy Balance for Insertion Battery Systems. *Journal of the Electrochemical Society*, 144(8):2697–2704, 1997.

[101] G. Botte, B. Johnson, and R. White. Influence of Some Design Variables on the Thermal Behavior of a Lithium-Ion Cell. *Journal of The Electrochemical Society*, 146(3):914–923, 1999.

[102] S. Santhanagopalan, Q. Guo, P. Ramadass, and R. E. White. Review of models for predicting the cycling performance of lithium ion batteries. *Journal of Power Sources*, 156(2):620–628, 2006.

[103] V. Ramadesigan, P. W. C. Northrop, S. De, S. Santhanagopalan, R. D. Braatz, and V. R. Subramanian. Modeling and Simulation of Lithium-Ion Batteries from a Systems Engineering Perspective. *Journal of the Electrochemical Society*, 159(3):R31–R45, 2012.

[104] D. Zhang, B. N. Popov, and R. E. White. Modeling Lithium Intercalation of a Single Spinel Particle under Potentiodynamic Control. *Journal of The Electrochemical Society*, 147(3):831–838, 2000.

[105] M. Guo, G. Sikha, and R. E. White. Single-Particle Model for a Lithium-Ion Cell: Thermal Behavior. *Journal of The Electrochemical Society*, 158(2):A122–A132, 2011.

[106] V. R. Subramanian, V. D. Diwakar, and D. Tapriyal. Efficient Macro-Micro Scale Coupled Modeling of Batteries. *Journal of The Electrochemical Society*, 152(10):A2002–A2008, 2005.

[107] M. Doyle and J. Newman. Modeling the performance of rechargeable lithium-based cells: design correlations for limiting cases. *Journal of Power Sources*, 54:46–51, 1995.

[108] V. Ramadesigan, R. N. Methekar, F. Latinwo, R. D. Braatz, and V. R. Subramanian. Optimal Porosity Distribution for Minimized Ohmic Drop across a Porous Electrode. *Journal of The Electrochemical Society*, 157(12):A1328–A1334, 2010.

[109] M. Doyle and J. Newman. The use of mathematical modeling in the design of lithium/polymer battery systems. *Electrochimica Acta*, 40(13):2191–2196, 1995.

[110] J. Newman. Optimization of Porosity and Thickness of a Battery Electrode by Means of a Reaction-Zone Model. *Journal of The Electrochemical Society*, 142(1):97–101, 1995.

[111] M. Doyle, T. Fuller, and J. Newman. Modeling of galvanostatic charge and discharge of the lithium/polymer/insertion cell. *Journal of the Electrochemical Society*, 140(6):1526–1533, 1993.

[112] P. Arora, M. Doyle, A. S. Gozdz, R. E. White, and J. Newman. Comparison between computer simulations and experimental data for high-rate discharges of plastic lithium-ion batteries. *Journal of Power Sources*, 88(2):219–231, 2000.

[113] M. Doyle, J. Newman, and A. Gozdz. Comparison of modeling predictions with experimental data from plastic lithium ion cells. *Journal of The Electrochemical Society*, 143(6):1890–1903, 1996.

[114] T. Fuller, M. Doyle, and J. Newman. Simulation and optimization of the dual lithium ion insertion cell. *Journal of the Electrochemical Society*, 141(1):1–10, 1994.

[115] T. Fuller, M. Doyle, and J. Newman. Relaxation Phenomena in Lithium-Ion-Insertion Cells. *Journal of the Electrochemical Society*, 141(4):982–990, 1994.

[116] P. M. Gomadam, J. W. Weidner, R. a. Dougal, and R. E. White. Mathematical modeling of lithium-ion and nickel battery systems. *Journal of Power Sources*, 110(2):267–284, 2002.

[117] G. Ning, R. E. White, and B. N. Popov. A generalized cycle life model of rechargeable Li-ion batteries. *Electrochimica Acta*, 51(10):2012–2022, 2006.

[118] P. Ramadass, B. Haran, R. White, and B. N. Popov. Mathematical modeling of the capacity fade of Li-ion cells. *Journal of Power Sources*, 123(2):230–240, 2003.

[119] P. Ramadass, B. Haran, P. M. Gomadam, R. White, and B. N. Popov. Development of First Principles Capacity Fade Model for Li-Ion Cells. *Journal of The Electrochemical Society*, 151(2):A196–A203, 2004.

[120] K. E. Thomas and J. Newman. Thermal Modeling of Porous Insertion Electrodes. *Journal of The Electrochemical Society*, 150(2):A176, 2003.

[121] G. B. Less, J. H. Seo, S. Han, a. M. Sastry, J. Zausch, A. Latz, S. Schmidt, C. Wieser, D. Kehrwald, and S. Fell. Micro-Scale Modeling of Li-Ion Batteries: Parameterization and Validation. *Journal of The Electrochemical Society*, 159(6):A697–A704, 2012.

[122] S. Al Hallaj, H. Maleki, J. S. Hong, and J. R. Selman. Thermal modeling and design considerations of lithium-ion batteries. *Journal of Power Sources*, 83(1-2):1–8, 1999.

[123] L. Song and J. W. Evans. Electrochemical-Thermal Model of Lithium Polymer Batteries. *Journal of The Electrochemical Society*, 147(6):2086–2095, 2000.

[124] M. Guo and R. E. White. An approximate solution for solid-phase diffusion in a spherical particle in physics-based Li-ion cell models. *Journal of Power Sources*, 198(2010):322–328, 2012.

[125] V. Srinivasan and C. Y. Wang. Analysis of Electrochemical and Thermal Behavior of Li-Ion Cells. *Journal of The Electrochemical Society*, 150(1):A98–A106, 2003.

[126] K. Kumaresan, G. Sikha, and R. E. White. Thermal Model for a Li-Ion Cell. *Journal of The Electrochemical Society*, 155(2):A164–A171, 2008.

[127] J. Newman and W. Tiedemann. Temperature rise in a battery module with constant heat generation. *Journal of the Electrochemical Society*, 142(4):1054–1057, 1995.

[128] Y. Chen and J. Evans. Heat Transfer Phenomena in Lithium/Polymer-Electrolyte Batteries for Electric Vehicle Application. *Journal of the Electrochemical Society*, 140(7):1833–1838, 1993.

[129] C. Hellwig. *Modeling, simulation and experimental investigation of the thermal and electrochemical behavior of a LiFePO$_4$-based lithium-ion battery*. PhD thesis, University of Stuttgart, 2013.

[130] A. Wiebelt, T. Isermeyer, T. Siebrecht, and T. Heckenberger. Thermomanagement von Lithium-Ionen-Batterien. *Automobiltechnische Zeitschrift*, 111(7-8):200–504, 2009.

[131] D. Goodwin. Cantera: An object-oriented software toolkit for chemical kinetics, thermodynamics, and transport processes. https://code.google.com/p/cantera/, 2009. (Retrieved: 17/02/2014).

[132] A. J. Bard and L. R. Faulkner. *Electrochemical Methods Fundamentals and Applications*. John Wiley & Sons, New York, USA, second edition, 2001.

[133] P. Atkins and J. de Paula. *Physical Chemistry*. Oxford University Press, Oxford, 9th edition, 2010.

[134] C. Hellwig, S. Sörgel, and W. Bessler. A Multi-Scale Electrochemical and Thermal Model of a LiFePO4 Battery. *ECS Transactions*, 35(32):215–228, 2011.

[135] M. Hedwig. Skalen uebergreifende Modellierung und Simulation des thermischen Verhaltens einer Lithium-Ionen-Batterie. Master's thesis, University of Stuttgart, 2012.

[136] R. J. Kee, M. Coltrin, and P. Glaborg. *Chemically reaction flow: Theory and practice*. Wiley Interscience, New York, 2003.

[137] N. Tanaka, P. Bartsch, C. Hellwig, A. Latz, and W. G. Bessler. Multi-scale Simulation of Thermo/Electrochemical mechanism in Li-ion Cells at Elevated temperature. In *The 224th ECS Meeting*, San Francisco, 2013.

[138] P. Bartsch. *Parametrierung eines thermischen Modells für Lithium-Ionen-Batterien mit Mangan-basierten Kathoden*. Studienarbeit (co-supervised by Nanako Tanaka), University of Stuttgart, 2013.

[139] M. Guo and R. E. White. A distributed thermal model for a Li-ion electrode plate pair. *Journal of Power Sources*, 221:334–344, 2013.

[140] W. Mielke. Modellierung von Kennlinien, Impedanzen und thermischen Verhalten einer Lithium-Eisenphosphat Batterie. Master's thesis, University of Stuttgart, 2011.

[141] B. McBride, M. Zehe, and S. Gordon. NASA Glenn coefficients for calculating thermodynamic properties of individual species. Technical report, Glenn Research Center, NASA, Cleveland, Ohio, 2002.

[142] National Institute of Standards and Technology. NIST standard reference database, 2013.

[143] L. Vogdanis, B. Martens, H. Uchimann, F. Hensel, and W. Heitz. Synthetic and thermodynamic investigations in the polymerization of ethylene carbonate. *Die Makromolekulare Chemie*, 472(3):465–472, 1990.

[144] W. G. Bessler. *Electrochemistry and transport in solid oxide fuel cells*. Habilitation, Heidelberg University, 2007.

[145] J. P. Neidhardt, D. N. Fronczek, T. Jahnke, T. Danner, B. Horstmann, and W. G. Bessler. A Flexible Framework for Modeling Multiple Solid, Liquid and Gaseous Phases in Batteries and Fuel Cells. *Journal of the Electrochemical Society*, 159(9):A1528–A1542, 2012.

[146] B. Horstmann, T. Danner, and W. G. Bessler. Precipitation in aqueous lithium-oxygen batteries: a model-based analysis. *Energy and Environmental Science*, 6(4):1299, 2013.

[147] D. N. Fronczek and W. G. Bessler. Insight into lithium-sulfur batteries: Elementary kinetic modeling and impedance simulation. *Journal of Power Sources*, 244:183–188, 2013.

[148] P. Deuflhard, E. Hairer, and J. Zugck. One-step and extrapolation methods for differential-algebraic systems. *Numerische Mathematik*, 516:501–516, 1987.

[149] M. Safari, M. Morcrette, A. Teyssot, and C. Delacourt. Multimodal Physics-Based Aging Model for Life Prediction of Li-Ion Batteries. *Journal of The Electrochemical Society*, 156(3):A145–A153, 2009.

[150] C. Picart, J. Mutterer, L. Richert, Y. Luo, G. D. Prestwich, P. Schaaf, J.-C. Voegel, and P. Lavalle. Molecular basis for the explanation of the exponential growth of polyelectrolyte multilayers. *Proceedings of the National Academy of Sciences of the United States of America*, 99(20):12531–5, 2002.

[151] A. M. Colclasure, K. a. Smith, and R. J. Kee. Modeling detailed chemistry and transport for solid-electrolyte-interface (SEI) films in Li-ion batteries. *Electrochimica Acta*, 58:33–43, 2011.

[152] N. Tanaka, M. Hedwig, C. Hellwig, and W. G. Bessler. Toward Modeling Thermal Runaway of Li-ion Batteries. In *9th Symposium on Fuel Cel and Battery Modeling and Experimental Validation (ModVal9)*, Campus Sursee, Switzerland, 2012.

[153] N. Tanaka, C. Hellwig, and W. G. Bessler. Investigatoin of a kinetic mechanism for runway thermo-electrochemistry in lithium-ion cells. In *19th International Conference on Solid State Ionics (SSI-19)*, Kyoto, Japan, 2013.

[154] N. Tanaka and W. Bessler. Numerical investigation of kinetic mechanism for run-
away thermo-electrochemistry in lithium-ion cells. *Solid State Ionics*, 2014 (In
press).

[155] B. J. MacBride, S. Gordon, and M. A. Reno. Coefficients for Calculating Thermo-
dynamic and Transport Properties of Individual Species. Technical report, Lewis
Research Center, NASA, Ohio, Cleveland, 1993.

[156] D. Aurbach, I. Weissman, a. Zaban, and P. Dan. On the role of water contamination
in rechargeable Li batteries. *Electrochimica Acta*, 45(7):1135–1140, 1999.

[157] X. Guo and R. Madix. Oxygen-activated combustion of alkenes on the Pd (100)
surface. *Journal of the American Chemical Society*, (1):5523–5530, 1995.

[158] B. E. Deal and H. J. Svec. Kinetics of the reaction between lithium and water vapor.
Technical Report July, Ames Laboratory, 1953.

[159] A123 Systems, LLC. http://www.a123systems.com/. (Retrieved: 17/04/2014).

List of publications

Reviewed paper

- N. Tanaka, W.G. Bessler, "Numerical investigation of kinetic mechanism for runaway thermo-electrochemistry in lithium-ion cells", Solid State Ionics, 262, 70-73, 2014

Conference presentations

- N. Tanaka, M. Hedwig, C. Hellwig, and W. G. Bessler, "Toward modeling thermal runaway of Li-ion batteries", 9th Symposium on Fuel Cell and Battery Modeling and Experimental Validation, Sursee, Switzerland, April 2012 (Best poster award)

- C. Hellwig, N. Tanaka, B. Horstmann, and W. G. Bessler, "A Multi-scale Thermo-Electrochemical $LiFePO_4$ Battery Model Based on the Domino-Cascade Mechanism", The 16th International Meeting on Lithium Batteries, Jeju, Korea, June 2012

- J. Mehne, W. Nowak, M. Danzer, H. Döring, N. Tanaka, and W. G. Bessler, "Towards Predicting Thermal Runaway of Lithium-Ion Batteries", 13th Ulm Electrochemical Talks, Ulm, Germany, July 2012

- W.G. Bessler, N. Tanaka, C. Hellwig, M. A. Danzer, H. Döring , J. Mehne, and W. Nowak, "Towards Understanding Thermal Runaway of Lithium Batteries", Kraftwerkbatterie 2013, Aachen, Germany, February 2013

- N. Tanaka, J. Mehne, W. Nowak, M. A. Danzer, H. Döring, and W. G. Bessler, "Numerical Simulation and Experimental Validation for Thermal Runaway on Lithium-ion Cells", 10th Symposium on Fuel Cell and Battery Modeling and Experimental Validation, Bad Boll, Germany, March 2013

- N. Tanaka, C. Hellwig, and W. G. Bessler, "Investigation of a Kinetic Mechanism for Runaway Thermo-electrochemistry in Lithium-ion Cells", The 19th International Conference on Solid State Ionics, Kyoto, Japan, June 2013

- N. Tanaka, P. Bartsch, C. Hellwig, A. Latz, and W. G. Bessler, "Multi-scale Simulation of Thermo/Electrochemical Mechanism in Li-ion Cells at Elevated Temperature", 224th ECS Meeting, San Francisco, USA, October 2013

- N. Tanaka, P. Bartsch, M. A. Danzer, H. Döring, W. G. Bessler, "Thermo-Electrochemical Simulation of Li-Ion Cells Under Abuse Condition", The 17th International Meeting on Lithium Batteries, Como, Italy, June 2014

Acknowledgements

The completion of this thesis could not have been achieved without the support I received from numerous individuals.

With the deepest gratitude, I would like to thank my adviser, Prof. Wolfgang Bessler, for all the support throughout this project and for giving me an opportunity to engage in research in Germany. I would appreciate for all the time he spent with me to go through the challenging topic and for providing me a starting point on the battery model and theory of electrochemistry, which I had only a few insights.

I would like to acknowledge our department leaders, Prof. Andreas Friedrich and Prof. Arnulf Latz, for providing comfortable working environment which allow me to concentrate on research. Specifically, I would like to thank Prof. Friedrich for all the support as a second supervisor of this thesis.

I would like to express my gratitude to my project partners, Prof. Wolfgang Nowak (University of Stuttgart), Dr. Harry Döring (ZSW), Dr. Michael Danzer (ZSW), and Mr. Julian Mehne (University of Stuttgart), for their productive collaboration. Without their help, I would not have accomplished my project goal.

I would like to thank Dr. Christian Hellwig for his help and efforts he made to understand the battery model. I also need to thank Mr. Philipp Bartch for his efforts to construct the blended cell model.

I would like to thank group members and co-workers at DLR: Dr. Birger Horstmann for fruitful discussion about thermodynamics; Dr. Vitaliy Yurkiv for all his supports especially on starting up new life in Germany; Dr. Andreas Hofmann for reviewing my thesis and deep understanding about Japanese cultures; Mr. Klaus Göckelmann for helping me to deal with programming issues; Dr. Thomas Jahnke for fruitful discussion; Mr. David Fronczek for his help on DENIS programming; my former roommate, Dr. Jonathan Neidhardt, for his support especially on phase managements in DENIS; Mr. Timo Danner for implicitly encouraging me to complete my thesis on time; Dr. Caroline Willich for helping me to release my stress by violin and cello duet; Mr. Andreas Vogler for his help

on paperwork; Dr. Stefanie Braun, Mr. Georg Futter, and Mr. Simon Hein for enjoyable life at DLR.

I would also like to express my deepest thanks and appreciation to my longstanding friend, Ms. Emily Thompson, for her tremendous help on revising my poorly written English.

Furthermore, I would like to acknowledge my husband, Shinji, and my family for loving support to pursue my degree in a foreign country.

Finally, I would like to express gratitude to the Volkswagen Foundation for the full financial support throughout my research life at DLR.

Declaration of Authorship

I hereby certify that the dissertation entitled

MODELING AND SIMULATION OF THERMO-ELECTROCHEMISTRY OF THERMAL RUNAWAY IN LITHIUM-ION BATTERIES

is entirely my own work except where otherwise indicated. Passages and ideas from other sources have been clearly indicated.

Ich versichere, dass ich die vorliegende Arbeit mit dem Titel

MODELING AND SIMULATION OF THERMO-ELECTROCHEMISTRY OF THERMAL RUNAWAY IN LITHIUM-ION BATTERIES

selbständig verfasst und keine anderen als die angegebenen Quellen und Hilfsmittel benutzt habe; aus fremden Quellen entnommene Passagen und Gedanken sind als solche kenntlich gemacht.

Name/Name: _____

Unterschrift/Signature: _____

Datum/Date: _____